Utrecht University

Faculty of Geosciences

Department of Physical Geography

MASTER THESIS

Scale effects on waves and sediment mobility in the Metronome tidal facility

Author: E.P. van Onselen
Student ID: 4007069
1st supervisor: Prof. Dr. Maarten Kleinhans
2nd supervisor: Prof. Dr. Gerben Ruessink

UTRECHT, June 2017

Contents

Figures

Summary

I quantified scale effects on very small (~1 cm high, wavelength 20-30 cm) waves and on resulting wave-induced sediment mobility. The aim of this research is to gain and understanding of scale effects on wave dimensions, shape and ultimately wave-induced sediment mobility. Topics covered in this thesis are: (1) the effect of small-scale waves (~ 1 cm wave height) on wave non-linearity; (2) The effect of scaling on wave height loss (i.e. energy dissipation); (3) the effect of assumed distortion on the sediment size scaling requirement for mobility similitude; and (4) Implications of the aforementioned points on sediment transport. Wave experiments were conducted in the Metronome tidal facility by measuring wave time series at various cross-shore positions over simplified straight coast and ebb delta bathymetries. Relevant parameters such as mean wave height, skewness, asymmetry, near-bed orbital velocity and mobility were computed from these time series. A numerical wave model (SWASH) was employed to model waves after the Metronome experiments, which despite the small scale was able to accurately reproduce waves similar to those measured in the Metronome. The main use of SWASH was to scale up the Metronome experiments to a 500 times larger prototype using Froude scaling (i.e. Froude numbers in model and prototype are the same). This allowed investigating the scaling requirements for mobility similitude through varying the sediment size scale and model distortion (e.g. in small-scale models, slopes are often much steeper than in nature, hence these models are distorted).

Despite the very small-scale waves in the Metronome, surface tension and internal friction effects are minimal and only become significant for waves with wavelengths smaller than 0.1 m. Furthermore, the amount and rate of wave energy dissipation in the near-shore zone is similar across scales and is independent of model distortion. Wave non-linearity measured in the wave experiments was compared to known parameterizations of non-linearity. Non-linearity barely translated into the development of wave skewness, whereas wave asymmetry clearly developed towards greater Ursell numbers. This behavior is most likely related to a combination of steeper (than in nature) offshore waves and beach slopes, which limit the time for skewness to develop. The lack of skewness and lower wave non-linearity in general suggests a decreased on-shore transport component which should be accounted for in comparing equilibrium bed profiles or long-shore transport fluxes.

Through comparing mobility from measurement in the Metronome to its 500 times up-scaled counterpart, sediment size scaling requirements were derived for various assumed model distortions. It appears that increasing model distortion leads to a lower mobility in the 1:500 prototype. For example: undistorted, it requires a median sediment size of 10 cm to ensure mobility in the Metronome is the same as in the modelled prototype, whereas at a distortion of 5 only a median sediment size of 1 cm is required. I have thus been able to expand the scaling law for sediment size to include the effect of model distortion.

Compared to nature, mobility in the Metronome is significantly lower. Hence it is recommended to increase mobility through lowering sediment density or by generating higher and steeper waves. The latter will also improve similitude of the surf zone similarity parameter through lowering it. However, wave should not be made too steep to ensure that wave breaking remains depth-induced, rather than steepness induced.

1. Introduction

In the recently developed Metronome tidal facility in Utrecht, a twenty-by-three meter tilting flume, patterns associated with estuaries, including ebb-deltas, can be recreated. The tilting process creates a non-steady flow that mimics the alternation of ebb and flood currents. Observations include bars, shoals and mutually evasive ebb and flood channels that are hypothesized to be formed by similar factors as river bars (Kleinhans et al., 2015) In addition to the tilting mechanism, a wave generator that produces monochromatic waves was installed close to the seaward boundary of the flume. From preliminary results it appears that wave reworking leads to an overall downdrift migration of the ebb delta and the formation of swash-aligned barrier island on its terminal lobe (Roelofs, 2016). These developments of the ebb-tidal delta raise questions about scaling difficulties associated with the generated waves and their relation to ebb-tidal delta development as a function of wave-induced sediment mobility.

An ebb-tidal delta is a common depositional feature that is found in front of estuaries and tidal inlets along barrier coasts and is formed under micro- to meso-tidal conditions (Hayes, 1975). The overall morphology of an ebb-tidal delta is a function of both tidal currents and waves (Hayes, 1980; De Swart & Zimmerman, 2009). The ebb delta is to some extent reworked by waves, which may lead to the formation of inter- and/or supratidal swash bars (Oertel, 1972, Hayes, 1975). In case of a barrier-inlet system, sandy shoals may move from the ebb delta and attach to an adjacent barrier island (Ridderinkhof et al., 2016) However, for isolated estuarine inlets in a meso-tidal environment, there are no records of swash bars on the ebb delta developing into fully fledged spits or barrier islands.

Physical models with waves are a widely popular and often used as a tool for practical engineering problems and fundamental research (Hughes, 1993). They are typically carried out at a much larger scale than in the Metronome (e.g. Petersej et al., 2008; Van Rijn et al., 2011, and references therein). Waves in the Metronome are roughly 1 cm high close to the wave generator, which is comparatively small, especially considering modern facilities where even meter-high waves can be generated and tested (e.g. the Delta Flume by Deltares). Wave frequency of Metronome waves varies between 2 and 2.5 Hz depending on the experiment that is carried out. Lower frequencies can be set, but would result in very long and low waves. Wavelength is in the order of 20-30 cm, which translates to deep water depths of 10-15 cm. On the seaward side of the ebb-delta's terminal lobe, the slope is steep and close to the submerged angle of repose of the medium coarse sand that is used (~ 30°). In nature, the terminal lobe's seaward-facing slope can have a gradient as high as 1:20 (see examples in e.g. Pickrill (1985) and Bertin et al. (2009)), but this is still much gentler than in the Metronome. This suggests, based on geometry alone, that slopes formed in the Metronome are a distorted representation of reality. In other words: the depth scale in the Metronome appears to be exaggerated with respect to the length scale. The small scale of waves and the steep coastal profiles in the Metronome pose a challenge in converting and comparing the experiment to natural scale. The difficulties in doing so due to scale effects and scaling requirements are the central theme of this thesis.

Previous research on scaling and scale effects of waves has been extensively covered over the last decades (see e.g. the book of Hughes, 1993 and the review of Van Rijn et al., 2011). Scaling principles are reviewed in chapter 2 of this report. Whereas scaling of physical models is traditionally approached by requiring similitude of dominant flow parameters, Kleinhans et al. (2014) noted that for recreating river patterns results similar to nature can be obtained, despite the violation of traditional scaling laws. In this research we follow a more traditional approach as we focus on the fine details of flow through wave parameters and bed mobility computations, rather than large-scale patterns within the entire estuary. Although the Metronome qualifies as a 'river model' in the classification of Kleinhans et al. (2014), the experiments and modelling efforts in this research are scaled with similitude of dimensionless parameters in mind (e.g. Froude number, Shields number). Therefore the experiments carried out in this research qualify as (distorted) Froude models (Figure 1). This was achieved by conducting simplified experiments with manually laid out straight coast and

delta bathymetries and only waves as a boundary condition. The results of this research are, however, to be placed in the broader context of coastal patterns and morphological development of the system.

A previous case study on waves in the Metronome by Roelofs (2016) showed that with increasing distance from the wave generator, wave height decreases. At the time, waves were generated by a small wave paddle located in a corner of the flume to allow generation of oblique incident waves. This inevitably led to wave diffraction, causing the observed wave height decrease. The experimental setup has since been adjusted to generate shore-normal waves over the entire width of the flume to mitigate the effect of diffraction. This should also decrease the suggested reflection problems as waves travel parallel to the flume's sidewalls. The current setup allows for a detailed study of wave characteristics but is less suitable for studying the effect of wave-induced long-shore currents on a self-formed ebb-tidal delta.

The overarching aim of this research is to gain and understanding of scale effects on wave dimensions, shape and ultimately wave-induced sediment mobility. This is done by quantitatively describing scale effects and scaling requirements to gain overall mobility similitude on the ebb-delta. More specifically we study (1) the effect of waves at Metronome scale on wave non-linearity; (2) The effect of scaling on wave height loss (i.e. energy dissipation); (3) the effect of assumed distortion on the sediment size scaling requirement for mobility similitude; and (4) Implications of the aforementioned points on sediment transport.

This thesis is organized as follows: Chapter 2 discusses potential effects on very small scale waves, known wave scaling laws, and mobility similitude requirements. Chapter 3 presents the methods, computations and limitations of data retrieval from the physical models. Chapter 4 is the results section for 1:1 (Metronome scale) wave model results. The scale is blown up in chapter 5, where numerically modelled results are presented for the Metronome setup at 500 times its original size. Finally, discussion and conclusions follow in chapter 6 and 7.

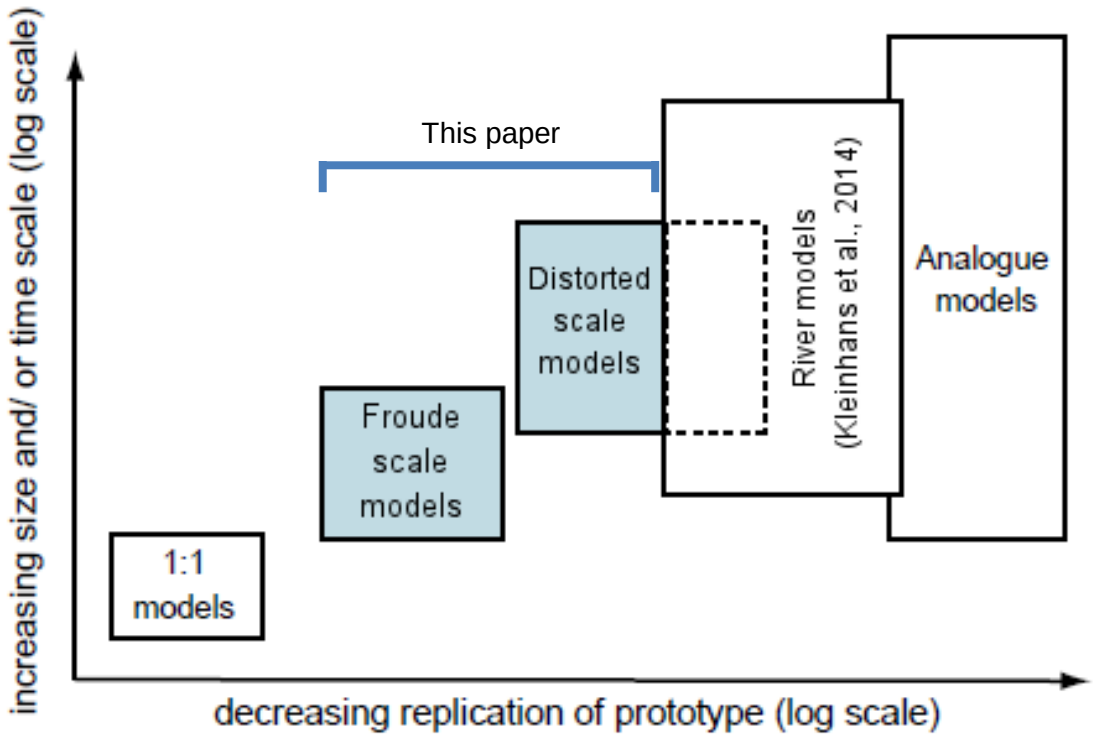

Figure 1. Schematic overview of physical model types (modified after Peakall et al. (1996) and Kleinhans et al. (2014). The type of models used (or assumed if we regard the Metronome as an already distorted representation of reality), fall between prototype scale (1:1) models that fulfill most similitude requirements and the large scale system-wide 'River model' by Kleinhans et al., (2014) that relaxes similitude requirements but nonetheless results in similar patterns observed in nature.

2. Wave scaling

Scale models are an important tool for coastal engineers and scientists to help understanding the effects of waves and flow on both natural and human-made coastal structures. Experimentation with hydraulic scale experiments began as early as 1752 (Hudson et al., 1979). The first formulation of similitude criteria from which eventually the Froude criterion of similitude was developed was proposed a hundred years later, in 1852 (Hughes, 1993). Over the years, hydraulic scale models evolved to become an indispensable part of coastal and fluvial engineering and science.

The effective use of waves in experiments comes with a number of challenges related to (1) disproportionate scaling of wave parameters (Kamphuis, 1972; Hughes, 1993; Van Rijn et al., 2011); (2) simplification of the prototype situation (e.g. using monochromatic waves versus wave spectrum); (3) distortion of length scale and (4) artificial effects due to wave generation and limited basin dimensions.

2.1. Scaling laws

Scaling in hydraulic experiments is based on retaining similitude of dimensionless flow parameters between the prototype and model in order to get a correct representation of physical processes (Van Rijn et al., 2011). Scaling of any parameter is given by the scale ratio *n*, which is the ratio between the prototype parameter value and the model parameter value. Hence,

$$n = \frac{X_p}{X_m} \tag{2.1}$$

Ideally, the scale ratios of both geometric (dimensions), kinematic (wave motion) and dynamic (forces) are identical. However, both in theory and in practice it is impossible to achieve similitude between all scale ratios except at prototype scale (Hughes, 1993). It is therefore necessary to identify the dominant forces in order to justify the neglecting of others (Hudson et al., 1979).

2.1.1. Hydraulic similitude

Scaling of waves is based on similitude of the ratio between inertial forces and gravitational forces, where gravity is the dominant restoring force (Hughes, 1993). This ratio is represented by the Froude number,

$$Fr = \frac{u}{\sqrt{gL}} \tag{2.2}$$

where u is the orbital velocity amplitude and L is wavelength. In order to get the same Froude number in the model and the prototype ($n_{Fr} = 1$), the following condition must be met, which follows from Eq. (2.2):

$$n_u = \left(n_g n_L\right)^{0.5} \tag{2.3}$$

where the scale ratio for gravity $n_g = 1$. Similarly, it follows from linear wave theory that $n_L = n_h = (n_T)^2$. In addition, the scale ratio of water depth (n_h) is directly proportional to the scale ratio of wave height (n_H), which follows from the formulations of fluid particle motion under a wave. Coupling these scale ratios to Eq. (2.3) yields the full expression for Froude scaling as given by Van Rijn et al. (2011)

$$n_u = n_T = (n_L)^{0.5} = (n_H)^{0.5} = (n_h)^{0.5} \tag{2.4}$$

In a laminar flow regime (Re < 1000) where viscous forces dominate the orbital flow under waves, the ratio between inertial forces and viscous forces should be considered for scaling instead (Hughes, 1993). This ratio in given by the Reynolds number

$$Re = \frac{uL}{\nu} \tag{2.5}$$

where ν is the fluid kinematic viscosity, which for water at a temperature of 293 K equals $1 \cdot 10^{-6}$ m^2/s. Assuming that $n_\nu = 1$ and following the same principles used in the above derivation of Froude scaling, but now using the Reynolds number as scaling criterion, the scale for velocity becomes:

$$n_u = (n_T)^{0.5} = n_L = n_h = n_H \tag{2.6}$$

From the difference between Froude and Reynolds scaling laws it becomes obvious that for a scaled model, Froude similitude cannot coexist with Reynolds similitude. For example: if $n_{Fr} = 1$, then $n_{Re} > 1$, indicating that the model Reynolds number becomes smaller than in the prototype. Conversely, if Reynolds scaling is applied such that $n_{Re} = 1$, then $n_{Fr} < 1$, indicating that the model Froude number becomes higher than in the prototype.

For the smallest waves where surface tension is the main restoring force, the ratio between inertial forces and surface tension may be used to derive the scaling criterion. The ratio between inertial forces and surface tension is represented by the Weber number:

$$We = \frac{\rho u^2 L}{\sigma} \tag{2.7}$$

where ρ is fluid density in kg/m^3 and σ is the surface tension coefficient ($7.275 \cdot 10^{-2}$ N/m for water at T = 293 K). Assuming that fluid density and surface tension remain the same between prototype and model, the relation between scale ratios becomes:

$$n_u = (n_T)^{-1} = (n_L)^{-0.5} \ = (n_h)^{-0.5} = (n_H)^{-0.5} \tag{2.8}$$

Weber numbers in the Metronome are generally large enough (We > 50, i.e. inertial forces are predominant) to justify Froude or Reynolds scaling over Weber scaling. Surface tension effects are further detailed in section 2.3.

In general, similarity in Froude and Reynolds number alongside an undistorted geometric scale is required to achieve overall hydrodynamic similitude (Hughes, 1993). Since it is impossible to maintain Froude and Reynolds similitude at the same time, Van Rijn et al. (2011) note that keeping the Reynolds number larger than about 1000 (non-laminar flow regime) while maintaining Froude similitude is sufficient for most laboratory experiments.

2.1.2. Length scales and distortion

Similarly to wave parameter scale ratios, a scale ratio exists for basin dimensions. The relation between the horizontal length scale n_l and vertical scale n_h determines whether a model is distorted or not. For an undistorted representation of the prototype $n_l = n_h$, which means that the horizontal and vertical scale ratios are equal as well their derivatives (e.g. beach gradient). A model is distorted if the horizontal length scale is not equal to the vertical length scale, for which the distortion factor is expressed as n_l/n_h (Van Rijn et al., 2011).

Maintaining similitude of the surf zone similarity parameter (ξ) is desirable to correctly model the type of breaking after the prototype (Van Rijn et al., 2011). If the scale ratios of wave height and wavelength are not equal to the horizontal length scale ratio (e.g. in case of Froude scaling), a distorted model must be applied to maintain similitude in the surfzone similarity parameter. The surfzone similarity parameter is given by Battjes (1974) as,

$$\xi = \frac{\tan(\beta)}{\sqrt{H/L}} \tag{2.9}$$

where β is the gradient of the beach $\Delta h/\Delta l$. In order to satisfy the condition $n_\xi = 1$, it follows from Eq. (2.9) that,

$$\frac{n_h}{n_l} = \sqrt{n_H/n_L} \tag{2.10}$$

Combined with the formulation for Froude scaling Eq. (2.4) it follows that

$$n_T = (n_h)^{0.5} * \left(\frac{n_l}{n_h}\right) \tag{2.11}$$

Eq. (2.11) is the formulation of distorted Froude scaling, where the ratio (n_l/n_h) is recognized as the distortion factor. If (n_l/n_h) > 1, it means that the coastal profile is relatively gentle compared to the model, which is often required to maintain surfzone similarity similitude.

2.1.3. Mobility scaling requirements

For the purpose of this study it is important to maintain similitude in mobility parameters such that sediment mobility and transport can be correctly modelled after the prototype situation. The similitude requirements proposed by Kamphuis (1985) require that for a given situation both dimensionless grain size (Bonnefille number) and dimensionless shear stress (Shields parameter) are equal between prototype and model. Dimensionless grain size is given in Van Rijn (1984) as,

$$D^* = D_{50}\sqrt[3]{\frac{Rg}{\nu^2}} \tag{2.12}$$

where R is the relative submerged density given by $(\rho_s - \rho_w)/\rho_w$ and D_{50} is the median grain size . The Shields parameter is given by,

$$\theta = \frac{\tau}{(\rho_s - \rho_w) g D_{50}} \tag{2.13}$$

where τ is the dimensional shear stress in N/m^2. In addition the relative density (ρ_s/ρ_w) and the relative length (λ/D_{50}, where λ is wave amplitude in case of short, monochromatic waves) must be the same between prototype and model. Hence, the full requirement for similitude of bedload mobility based on Kamphuis (1985), given in Hughes (1993) becomes

$$n_{D^*} = n_\theta = \frac{n_{\rho_S}}{n_{\rho_w}} = \frac{n_\lambda}{n_{D_{50}}} = 1 \tag{2.14}$$

Obviously, not all similitude requirements can be met at the same time and choices must be made in case a model is designed based on a prototype. Since Shields' stress is a function of D_{50}, grain size must be scaled in proportion to shear stress to maintain similitude between prototype and model. Maximum shear stress at the bed is a function of maximum orbital velocity (U_w) and the friction factor (f_w), Hence D_{50} can also be expressed in scale ratios by combination of measured shear stress with Eq. (2.11) and Eq. (2.4), which is given by Van Rijn et al. (2011) and adopted for $n_{\rho s}/n_{\rho w} = 1$ as

$$n_{D50} = \frac{n_h n_{f_w}}{(n_l/n_h)^2} \tag{2.15}$$

Only the length and depth scale ratios are known as the friction factor by itself depends on D_{50}, requiring Eq. (2.15) to be solved iteratively. Eq. (2.15) shows that for a larger geometric distortion, n_{D50} decreases.

In previous studies n_{D50} was derived empirically from flume experiments. Noda (1972) performed experiments using sand with D_{50} = 0.0005 m, similar to what is used in the Metronome. He expresses n_{D50} as a function of n_h for a given geometric distortion, adapted from Van Rijn et al. (2011):

$$n_{D50} = n_h^{0.55} \tag{2.16}$$

$$n_h = n_l^{0.76} \tag{2.17}$$

which translates to a distortion (n_l/n_h) ≈ 5 for a length scale n_l = 500. Another set of empirically-derived D_{50} scaling laws is presented in Van Rijn et al. (2011) based on the work of Ito and Tsuchiya (1984, 1986, 1988) and Ito et al. (1995):

$$n_{D50} = n_h^{0.55} \text{ for } n_h < 2.2 \tag{2.18}$$

$$n_{D50} = 1.7 n_h^{0.2} \text{ for } n_h \geq 2.2 \tag{2.19}$$

2.1.4. Other scaling considerations

Even if viscous friction, internal friction and the contribution of surface tension are insignificant in a model is that is Froude scaled, surface tension may become important when waves start to break. Miller (1972) noted that for periodic progressive waves in a fluid with reduced surface tension, the limit steepness (H/L) and limit crest angle become larger. Since the waves in Millers experiments were 5-10 times larger in terms of wave height than those typically generated in the Metronome, it is to be expected that the shape of breaking waves in the Metronome is significantly affected by surface tension. Although breaking wave shape may be significantly affected, Le Mehauté (1976) found that energy dissipation is in similitude and that the momentum balance was satisfied, regardless of flow characteristics. Wave height reduction due to energy dissipation in the near-shore should thus be correctly modelled, despite limit steepness and limit crest angle not being in similitude. Finally, reflection of waves tends to be different between prototype and model and can either be greater or smaller based on the circumstances (Hughes, 1993).

2.2. Short wave attenuation

Once generated, the waves in the Metronome and similar-sized wave experiments are comparatively small and hence may be subject to external and internal forces that are otherwise negligible for sea and swell gravity waves in nature. It is important to determine whether these forces significantly affect waves in our basin by quantifying contribution of these forces to wave attenuation (i.e. dampening of wave energy).

Surface tension may act as a restoring force, hence dampening the wave motion. Wave celerity is also a function of surface tension as it acts as a restoring force, especially for very short and low waves (Le Méhauté, 1976). Thus, the contribution of surface tension can be included in the expression of linear wave theory. Linear theory including surface tension is given by Hughes (1993) as,

$$C^2 = \frac{gL}{2\pi}\tanh\left(\frac{2\pi h}{L}\right) + \frac{2\pi\sigma}{\rho L}\tanh\left(\frac{2\pi h}{L}\right) \tag{2.20}$$

where C is wave celerity, L is wavelength, h is water depth, ρ is fluid density and g is acceleration due to gravity. The surface tension coefficient σ was taken from the tables provided by Varfaftik et al. (1984). For water at a temperature of 20 °C, $\sigma = 7.275 \cdot 10^{-2}$ N/m. Eq. (2.20) consists of a gravity term known as the wave dispersion relation (left of the addition) and a surface tension term. The ratio between the surface tension term and the gravity term, after rearrangement, becomes,

$$f_{st} = \frac{(2\pi)^2 \sigma}{\gamma L^2} \tag{2.21}$$

where f_{st} represents the fractional contribution between 0 and 1 of surface tension to the wave dispersion relation with $\gamma = \rho g$ being the specific weight of water. For water on earth at a temperature of 293 K, $f_{st} \approx 2.9 \cdot 10^{-4}/L^2$. Thus for waves with L = 0.25 m, $f_{st} \approx 0.0046$, which is not significant.

Friction effects dissipate wave energy and hence reduce wave height as a wave propagates in the flume. Hughes (1993) notes that friction may not be scaled properly in a Froude-scaled model since the Reynolds number of the prototype and model differ. The friction effects considered here are (1) internal friction (Keulegan, 1950; Hughes, 1993) and (2) viscous boundary layer friction (Keulegan, 1950; Johnson, 1966; Madsen et al., 1988; Hughes, 1993). An expression for wave attenuation due to internal shearing stresses was first developed by Keulegan (1950) and is given by Hughes (1993) in rearranged form as,

$$\frac{H(t)}{H_{t=0}} = e^{-\left(\frac{8\pi^2 \nu t}{L^2}\right)} \tag{2.22}$$

where $H(t)$ is the wave height after time t, $H_{t=0}$ is the initial wave height at the position of the wave generator and ν is the fluid kinematic viscosity, which is about $1 \cdot 10^{-6}$ m^2/s for water at a temperature of 293 K. The ratio between $H(t)$ and $H_{t=0}$ should ideally approach 1, which means that no significant amount of wave energy is lost due to internal friction. Using measured wavelength and linear theory to derive wave celerity, $H(x)/H_{x=0}$ can be calculated for a given travel distance x.

Under wave motion in intermediate to shallow depth water, near-bed orbital motion causes the development of a thin viscous boundary layer under the wave crest and trough that drains wave energy. Furthermore, a boundary layer develops along the flume's sidewalls causing another potential source of wave energy loss. The latter can be neglected if the width of the flume is much larger than the average water depth (e.g. the Metronome). Wave attenuation due to energy loss by the viscous boundary layer was expressed by Keulegan (1950) as

$$\frac{H(x)}{H_{x=0}} = e^{-\alpha x} \tag{2.23}$$

Where H_0 is the initial wave height at $x = 0$ and $H(x)$ is the wave height after travel distance x. α is the friction factor. The friction factor is based on the observation that wave energy flux through an infinitesimal narrow cross section equals 0 (i.e. eventually all wave energy is lost to viscous friction). Hence, the total mean rate of energy loss must be balanced by the work done on the fluid by pressure forces.

2.3. Wave generation

In the Metronome experiments, we strive to generate perfectly sinusoidal monochromatic waves. However, a wave generator system unavoidably generates higher (and lower) harmonics (e.g. second-order free waves) leading to wave nonlinearities on top of naturally-occuring nonlinearities (Hughes, 1993). For example: a free second-order wave is generated because the wave board motion does not exactly correspond to the motion of a progressive wave of constant form (Hansen and Svendsen, 1974). Since nonlinearities in the coastal zone are the main driving force behind sediment transport and current generation, it is important to understand and - if possible - suppress the nonlinear effects imposed by a wave generator such that only those nonlinearities, that are relevant for the studied topic, remain.

Second-order wavemaker theory is based on deriving generated wave motion up to second order using the known first-order motion of the wave board (Hansen and Svendsen, 1974; Spinneken and Swan, 2009). For piston-type wave generators this was first approximated by Madsen (1970, 1971)

and later by Daugaard (1972) and Multer (1973). Second-order theory for vertical flap-type wave generators was derived by Flick and Guza (1980) and was further improved by Kim et al. (1986) to include a time-independent solution for estimating return flow below nonlinear waves. More recently, a full second-order theory for wave generation by a rotating, translatory or combined wave board motion was developed by Schäffer (1996) and was later expanded to three dimensions by Schäffer and Steenberg (2003) for multi-directional wave experiments. However, it should be noted that none of these papers address the horizontal flap-type wave board that is installed in the Metronome, for it is an uncommon method to produce laboratory waves.

Using calculated first and second order wave components derived from second-order wavemaker theory, it is possible to introduce a correction term in order to suppress the generation of an unwanted higher harmonic free wave. First efforts were made by Hansen and Svendsen (1974), who were able to successfully bring down the second-order free wave amplitude to about 5-10% of the second-order Stokes component. Their solution was theory-based and included the addition of an extra wave component at the frequency of the second harmonic, which was added to the first order wave board motion, but in antiphase. Using their method, the movement of the wave board is not sinusoidal but remains constant through time. The most recent development includes real-time hydrodynamic feedback and was presented by Spinneken and Swan (2009). Their solution is based on the principle that force induced by the wave field acts upon the wave generator board. The nonlinear force component is derived from the real-time measurements by a force transducer and is subsequently used to feed back the required input force for the next time step. In contrast with the method proposed by Hansen and Svendsen (1974), the latter solution dynamically keeps up with wave non-linearity by adding an input wave component that cancels out the measured second order free wave motion.

An alternative approach to suppress unwanted higher harmonics in wave experiments was proposed by Hulsbergen (1974), who used a sill of rectangular cross-section and a height *0.1h* to produce a second harmonic free wave in antiphase with the second harmonic free wave that was forced by the wave generator. Thus, behind the sill only the first-order regular wave continues to exist. The position in the flume where the sill can best be placed is given by the overtake length, which is given by Hulsbergen (1974) as,

$$L_{ov} = L_{slow} * \frac{C_{fast}}{C_{fast} - C_{slow}} \tag{2.24}$$

where L is wavelength and C is wave celerity of the fast and slow waves as indicated by the subscripts. The second-order free wave generally travels slower than the first order component (Hughes, 1993). Hence, to calculate the overtake length of the second-order wave, L_{slow}, C_{fast}, and C_{slow} should be substituted by L_2, C_1, and C_2, respectively. In theory, it requires cross-spectral analysis to reliably determine wavelength and wave celerity of individual higher harmonic wave components. However, in practice and for the sake of simplicity, the sill may be placed by trial and error as Hulsbergen (1974) originally did.

3. Methods

Traditionally, the design of a scale model is based on a prototype situation which can be either nature or a large scale model. In this study, this approach was reversed. Waves were added to the Metronome experiment to ensure that their observed effects on morphology show at least some correspondence with nature. Thus, based on the experimental scale an up scaled prototype was reverse engineered to investigate similar behavior of waves and sediment mobility in the Froude scaled prototype. The effects of upscaling on wave and mobility parameters were then analyzed to gain an understanding of potential scale effects. The understanding of these scale effects was used to adjust scaling laws in order to find the requirements for similitude between prototype and scale model. A summary of the methods is given in Figure 2.

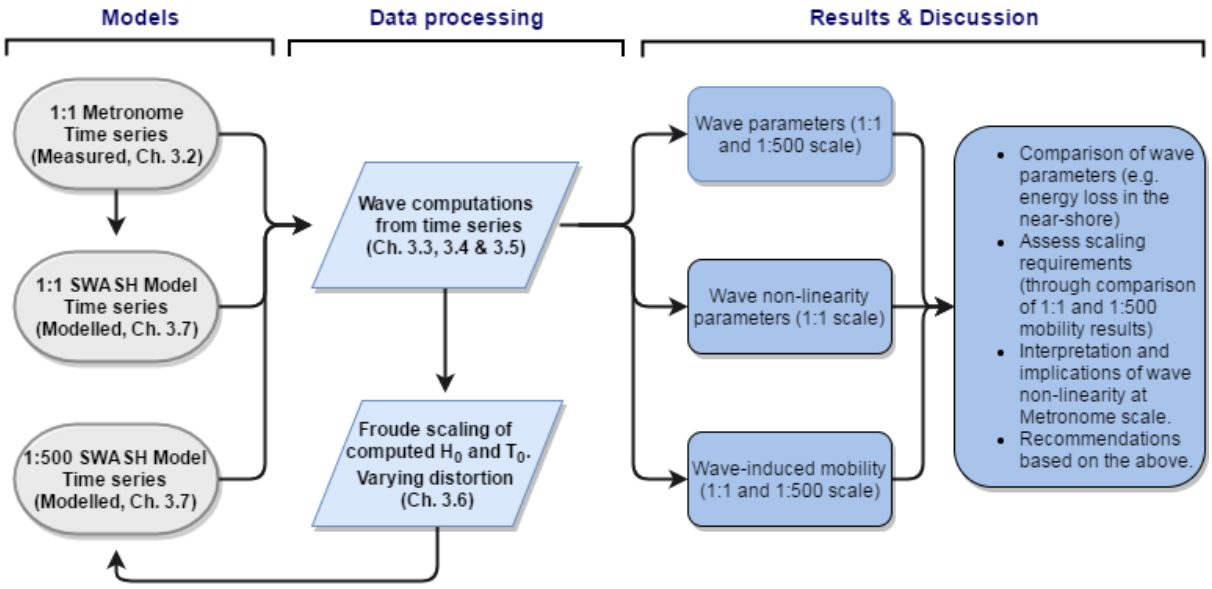

Figure 2. General outline of the method. Time series measured during the Metronome wave experiments (see Table 1 and Ch. 3.2) were used to set up SWASH models (see Ch. 3.7). Scaling to the prototype was done using computed mean offshore wave height (H_0) and period (T_0) from the measured time series. Output time series from 1:1 measured, 1:1 modelled and 1:500 modelled prototypes all underwent the same computations that are described in Ch. 3.3, 3.4 and 3.5.

3.1. Wave generation and characteristics

The wave generator in the Metronome tidal facility consists of a 3 m long (across the flume) and 10 cm wide wave board that is hinged on the far side of the basin. In neutral position, it rests flat on the water surface. Wave motion is induced by up-and-down motion of the wave board. The wave generator is best described as a 'horizontal flap-type' wave generator and is different from traditional flap-type, piston-type and plunger-type wavemakers described in Hughes (1993). Waves leaving the generator stretch over the entire width of the flume to eliminate wave energy loss by wave diffraction. It is capable of generating regular waves at a user-set frequency between 1 and 2.5 Hz. For these experiments, frequencies between 2 and 2.5 Hz were chosen based on previous observations and in order to attain an appropriate wavelength for deep water simulation in the offshore zone. A wave generator frequency of 2 Hz yields waves with a wavelength of roughly 30 cm.

Using short wave attenuation theory presented in the previous chapter, the contribution of surface tension to the wave dispersion relation and theoretical loss of wave energy due to internal and viscous boundary layer friction was predicted. The results of these predictions were used to confirm that the under given wave dimensions and wave travel distance, surface tension and friction effects are negligible. This was done by determining a set of arbitrary conditions that must not be exceeded. First, the main restoring force of the generated waves should be gravity. For this, the condition

F_{st} < 0.01, must be met. Secondly, between the wave board and the near-shore zone, wave height loss due to internal and viscous boundary layer friction may not exceed 2 % of the initial wave height.

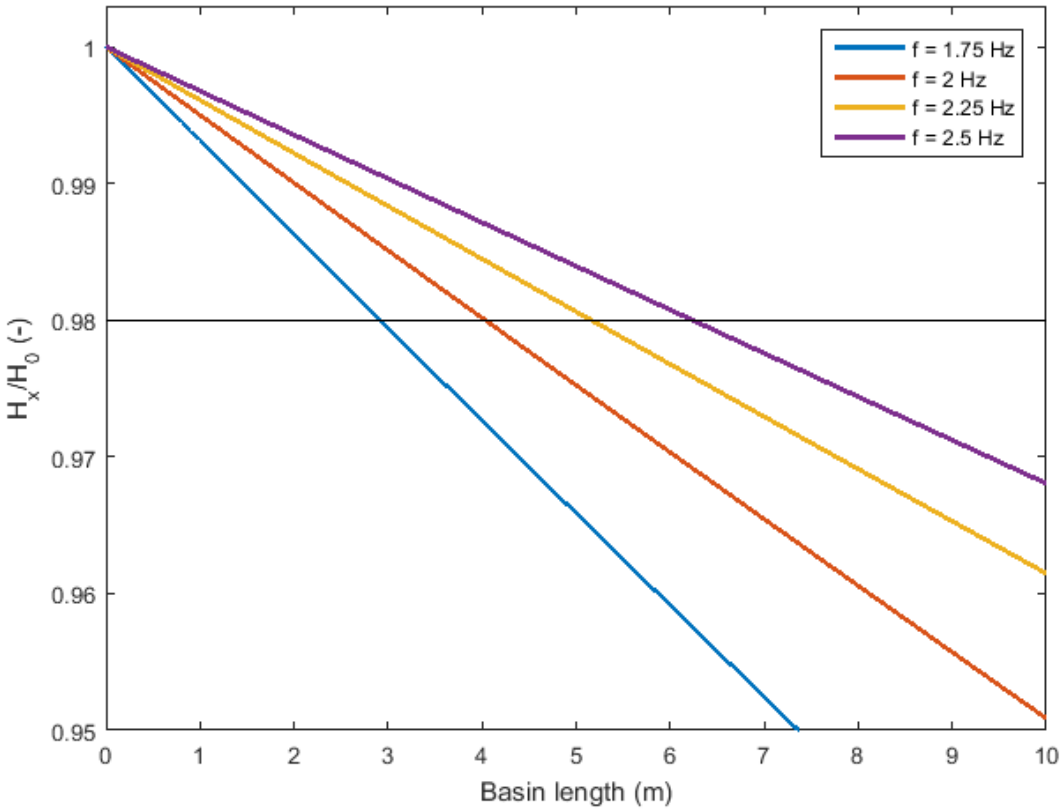

Figure 3. Wave attenuation (represented as a fraction of wave height of the initial wave height) for waves of a practical range of frequencies as a function of travel distance (basin length). Note typical length of the basin for wave experiments is 2 meters, thus less than 1% of the initial wave height is lost to friction effects.

From the predictions presented in section 2.3, it follows that for F_{st} = 0.01 the required minimum wavelength is 17 cm. Longer wavelengths imply an ever decreasing contribution of surface tension and are thus safe to use. For the wave experiments presented in this paper wavelengths are generally over 20 cm in the offshore zone, hence the surface tension term in Eq. (2.20) can safely be ignored in future computations. Wave height attenuation for different waves with a given frequency is presented in Figure 3. It appears that at metronome scale, these friction effects are minimal. However, the equation for viscous friction was derived for flumes with smooth sidewalls (Keulegan, 1950), whereas in the metronome a thicker turbulent boundary layer may develop due to the rough bottom.

3.2. Wave measurements

The data used for prototype comparison consists of four cross-shore profiles over different bathymetries. An overview of these experiments is presented in Table 1 below. Before running an experiment, the bathymetry was laid out and submerged to remove any crests or subaqueous slopes that are steeper than the angle of repose for wet sand. Next, water in the basin was removed in order to measure the distance between the bed and the echo sounder for each measurement location. Subsequently, for each measurement location, the distance between the echo sounder and still water level was measured. Measurements were conducted using a downward looking Massa M320/150 single beam echo sounder (SBES), which was set to its maximum sampling frequency of 20 Hz. Waves were recorded for two minutes at each location, during which results were directly sent to a computer and saved. Measurements were conducted starting at the coast in order to measure

waves before morphological changes could develop and affect waves. An exception is the ebb-delta experiment (4), where waves were allowed to rework the initial bathymetry for 24 hours before waves were measured. The experimental setup is illustrated in Figure 4.

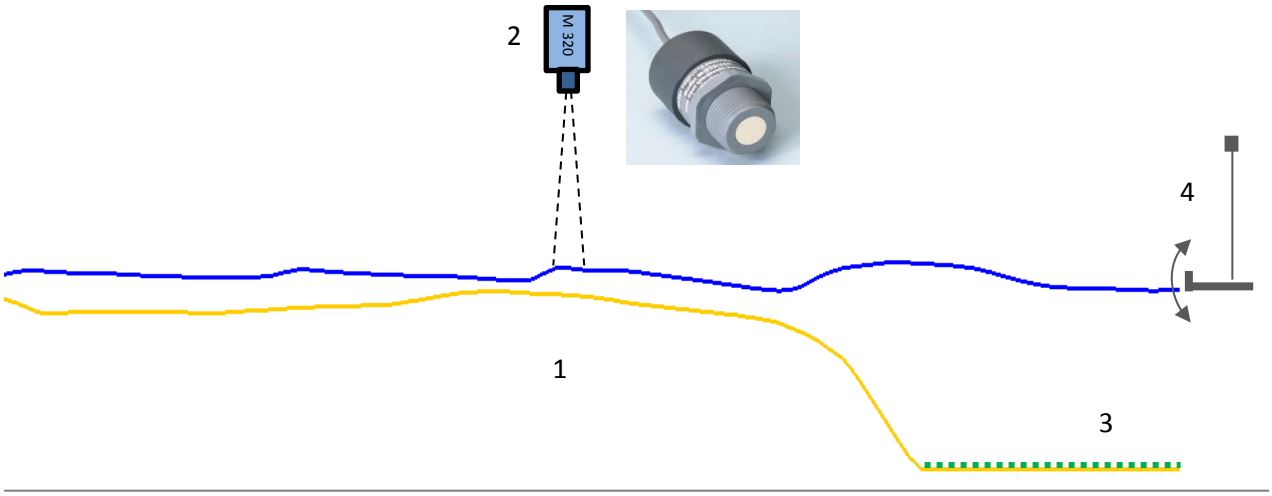

Figure 4. Side view of the experimental setup. The example bathymetry is from the ebb-delta experiment (Exp. 4, see Table 1). (1) Ebb-delta terminal lobe; (2) Massa M320/150 logger; (3) offshore zone with artificial grass bed; (4) wave generator. Time series were recorded for multiple positions along the profile to show the cross-shore development of wave parameters.

Table 1. Overview of conducted Metronome wave experiments

Parameter	Exp. 1	Exp. 2	Exp. 3	Exp. 4
Coastal profile type	Straight	Straight	Straight	Delta
Total length of the basin L_{basin} (m)	1.80	2.30	2.00	1.70
slope (m/m)	1:10	1:10	1:5	1:1
Measurements runtime (s)	100	100	100	100
Number of locations/time series	19	31	20	17
Offshore water depth $z_{offshore}$ (m)	0.060	0.096	0.069	0.062
Input wave frequency f (Hz)	2	2.5	2.5	2.25
Offshore wavelength L_0 (m)	0.33	0.23	0.22	0.28
Offshore wave celerity C_0 (m/s)	0.7	0.53	0.49	0.65
Sampling frequency f_s (Hz)	20	20	20	20
Offshore sampling density S (samples/wave)	9.4	8.7	9.1	8.5
Offshore mean vertical error, sample density related (% of H)	1.7	2.1	1.9	2.1
Offshore mean vertical error, footprint size related (% of H)	0.25	0.52	0.56	0.35
Near-shore mean vertical error, sample density related (% of H)	1.9	1.4	2.3	2.2
Near-shore mean vertical error, footprint size related (% of H)	2.7	5.8	3.5	1.9

3.2.1. Echo sounder limitations

Due to the design of the transducer, inaccuracy in the dataset may stem from (1) diffusive surface types (e.g. capillary ripples); (2) Decreased horizontal resolution due to footprint size of the beam; (3) Temperature fluctuations between measurements; and (4) decreased vertical accuracy due to propagation of waves and a limited sampling frequency. 1, 2 and 3 are system limitations, whereas 4 persists regardless of the precision and accuracy of the transducer.

Decreased precision due to e.g. diffusive surface types was automatically recorded on a scale of 0 to 100%, where the latter means maximum precision. During post-processing, all measurements with a recorded precision of 25% or lower were automatically discarded and re-interpolated based on surrounding points to maintain regularity along the time axis. Outliers were defined as points that lay more than two standard deviations from the mean of the most precise (100% precision) measurements. Points that met this criterion were removed using the above described procedure of re-interpolation.

3.2.2. Sample density-related inaccuracy

Decreased vertical accuracy due to propagating waves is attributed to the amount of samples per wave, hereafter referred to as the sampling density. Sampling density is a function of sampling frequency, wavelength and wave celerity. The sampling density is given by,

$$S = f_s \cdot \left(\frac{L}{C}\right) \tag{3.1}$$

Assuming a typical wave celerity for 1 cm high Metronome waves of 0.5 m/s and a wavelength of 0.25 m yields a sample density of 10 samples per wave at a sampling frequency of 20 Hz. The maximum distance that a measurement is offset from the wave crest or trough (horizontal offset, o_h) can be computed by,

$$o_{h,max} = \frac{L}{2S-2} \tag{3.2}$$

which essentially is half the horizontal resolution of the measurements (L/S-1). In our Metronome example the maximum distance that a distance measurement is offset from a wave crest or trough is 1.39 cm. Assuming a perfect sinusoidal wave of the form $\alpha sin(kx-\omega t)$, we can determine the maximum vertical error (assuming the distance measurement is accurate) as,

$$ve_{max} = \alpha - \{\alpha \sin(k(L/4 + ho_{max})\} \tag{3.3}$$

where α equals $H/2$. It should be noted that ve_{max} always represents and underestimation of the distance between target and transducer. For our Metronome example the maximum vertical error is 0.03 cm, which translates to 6% of the wave height provided that within a single wave ve_{max} at the crest equals ve_{max} in the trough. Eq. (3.3) can also be applied to asymmetric waves, but for skewed waves, loss of vertical accuracy is more significant for wave crests and less significant for wave troughs. Ideally, the sampling frequency must be increased to maximize the sampling density and thereby minimize the associated inaccuracy. Alternatively, the echosounder should be phase-matched with the wave generator such that for each wave a distance measurement exactly concurs with the passing of the wave crest and trough.

3.2.3. Footprint-related inaccuracy

Horizontal resolution of SBES is determined by the size of the beam's footprint, which is a function of slant range to the target and beam aperture. Footprint diameter on a horizontal surface is given by (International Hydrographic Organization, 2005)

$$a = 2z \cdot \tan\left(\frac{\phi}{2}\right) \tag{3.4}$$

where z is the height of the transducer above the target, which equals slant range for a downward-looking system. φ is the beam aperture. In case of measuring a sloping surface, the diameter of the beam's footprint along the direction of the slope increases. In the Metronome sensor height is 15 cm above still water level and the beam aperture of the Massa M320/150 is 8°. Under these conditions the footprint diameter is 2.1 cm on a flat surface. In a situation where waves are measured, a trough

is most difficult to detect as the lowest point is masked by the reflections coming from the edges of the beam (Simons and Snellen, 2016). Using Eq. (3.3) with $o_{h,max}$ = 0.5a the maximum error ve_{max} in the trough is about 0.017 cm, which is 1.7% of the wave height. Note that this maximum error occurs when a distance measurement is taken exactly above the wave trough, when the loss of vertical accuracy due to limited sampling density Eq. (3.2 & 3.3) is 0. In other words the maximum error due to sample density never adds to the maximum footprint-related error. An overview of sample density and footprint related inaccuracy is given in Figure 5.

3.2.4. Significance of sampling density and footprint related inaccuracy

For computing time-averaged wave parameters, both footprint and sampling density related inaccuracy are partially dealt with by averaging over a large number of waves, making use of naturally occurring variations in the wave period and the fact that it is unlikely that an integer number of samples exactly describes one wave (as opposed to our 'perfect' example where exactly 10 measurements fit within a wave cycle). In our case, e.g. wave height computations are based on roughly 200 waves in each time series, hence the error that varies between 0 and ve_{max} is also averaged such that the error in time-averaged wave height is less than 6% due to sampling density and less than 1.7% due to footprint size. If we assume a random distribution of errors between 0 and ve_{max} we can calculate the time-averaged error due to sampling density and footprint size by computing the mean vertical error (ve_m) from a random set of numbers between 0 and $o_{h,max}$ (illustrated in Figure 5). For sampling density, the mean error becomes 0.01 cm for both crest and trough, which translates to 2% of the wave height. For footprint size, the mean error becomes 0.0058 cm in the trough, which amounts to 0.58% of the wave height. The variation of footprint size between the crest and trough is minimal due to the low height of the waves with respect to the average slant range between the transducer and the water surface. Hence, it is safe to say that in time-averaged results these sources of inaccuracy are insignificant for typical Metronome waves.

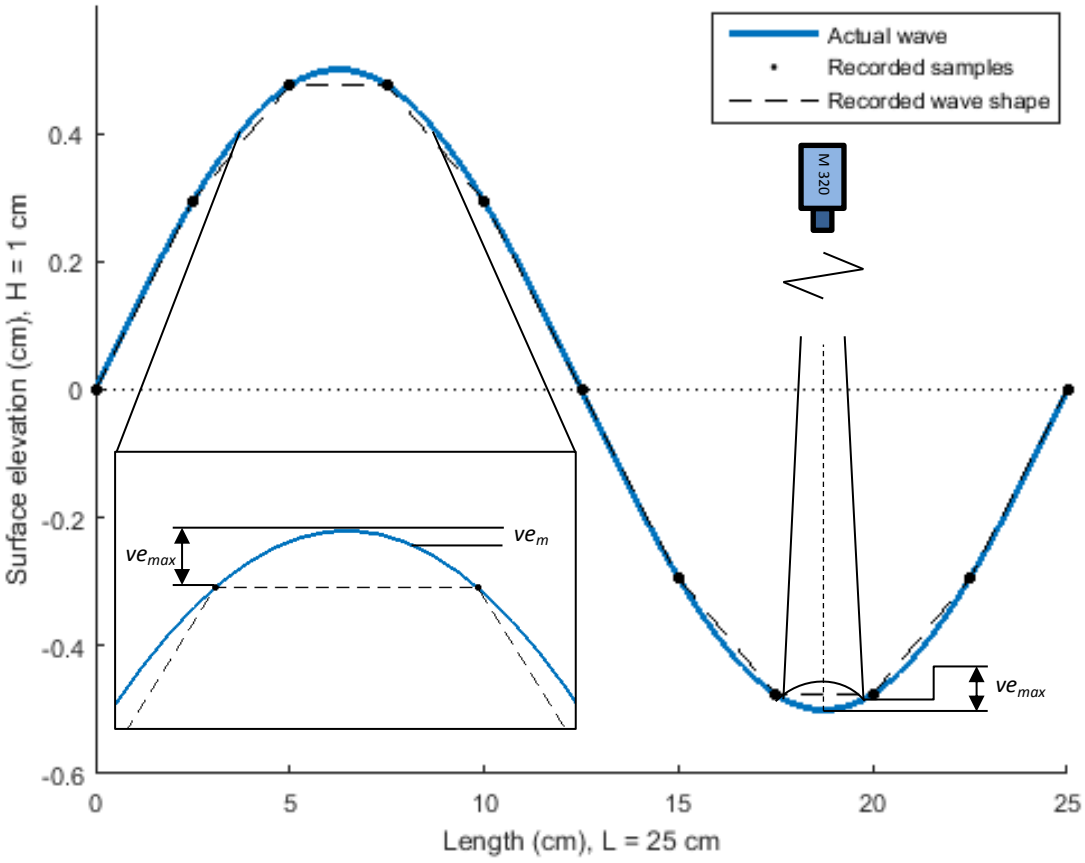

Figure 5. Sampling density and footprint related sources of inaccuracy. Maximum and mean sampling density related errors illustrated for the wave crest. Maximum footprint related error illustrated for the wave trough.

Sampling density related errors are a function of the offshore wavelength (and wave period or wave celerity for that matter, as they all relate to each other through the wave dispersion equation), which is presented in (Figure 6). It becomes clear that Metronome waves with wavelengths between 0.2 and 0.3 meters result in only small errors, but at offshore wavelengths below 0.1 both error sources increase exponentially.

Close to the shore where waves become lower, shorter and have steeper wave fronts, footprint-related problems may become larger with respect to sampling density issues and cause time-averaged parameters to be underestimated (fig). For example: suppose our waves with H = 1 cm, C = 0.5 m/s and L = 25 cm become 0.01 cm high and 15 cm long while travelling at a speed of 0.3 m/s: Using Eq. (3.1, 3.2 and 3.3) it follows that the 2% error in time-averaged wave height persists. The latter is because the sampling density remains the same as the ratio L/C in Eq. (3.1) does not change (hence the horizontal lines in Figure 6B). The error due to footprint size increases as the footprint itself does not become smaller. In this example the mean footprint-related error becomes 1.6% of the wave height. The footprint-related error only depends on wavelength, hence the red lines in Figure 6A and Figure 6B are the same.

Underestimation of time-averaged parameters due to a too low sampling density and a too large footprint diameter is mostly insignificant. Problems will arise if (1) the sampling frequency is lowered and/or (2) the waves become too short (< 0.1 m). However, none of this leads to significant errors in the Metronome experiments. An overview of offshore and near-shore underestimation of wave height for all Metronome experiments is also given in Table 1.

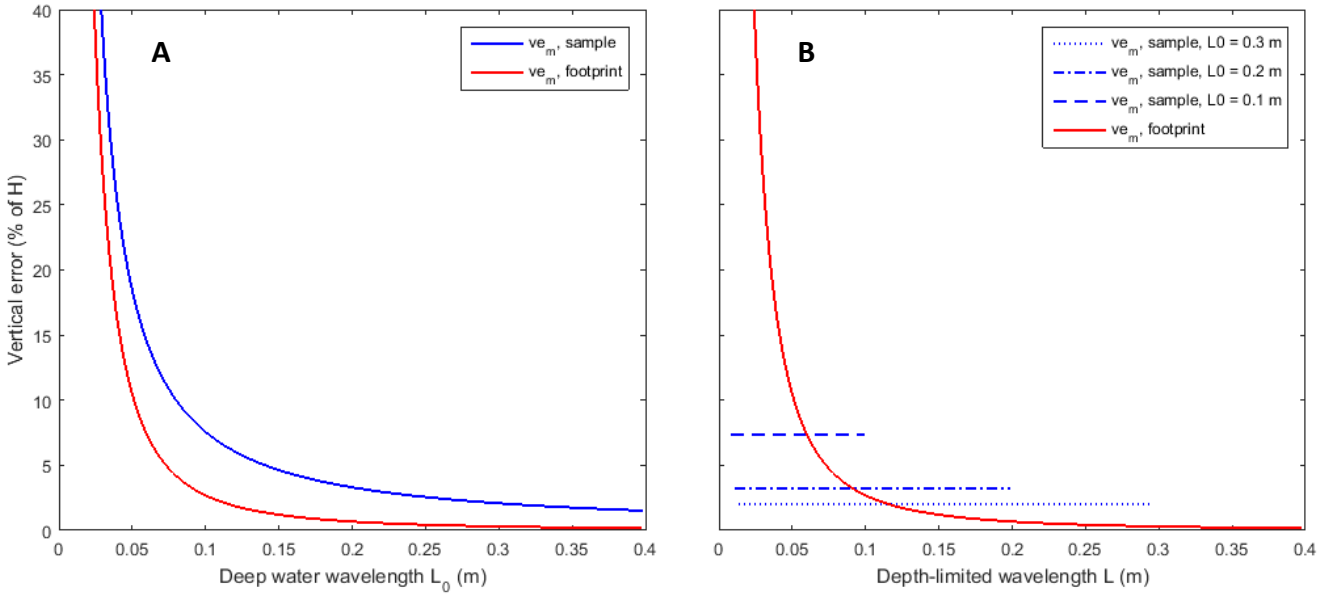

Figure 6. Sample density related (blue lines) and footprint size related (red lines) mean errors (ve_m) for a large amount of waves. (A) as a function of deep water wavelength, with wave period and celerity varying accordingly through the wave dispersion relation (L/C is not constant). (B) as a function of wavelength that reduces as a result of decreasing water depth where the ratio L/C is constant. Footprint-related errors only depend on wavelength and not on wave celerity, which is why the red lines in A and B are identical. Sampling density related errors depend on the ratio L/C (Eq. 3.1), hence they are constant in (B). The sampling density in this example is 20 Hz, transducer distance to target is 15 cm and beam aperture is 8°.

3.3. Wave parameters

The corrected time series were first converted to include free surface elevation (η) and still water depth (z) for the location of each time series. The zero-down crossing method was applied to calculate wave height and the period of individual waves in the time series. Since wave height and

period of the generated wave are most useful, a threshold was defined to filter out detected waveforms that are unrelated to the first-order wave (e.g. capillary ripples, erroneous sensor readouts). Too small waves were ignored by setting the minimum required wave height to 20% of the maximum wave height. For each time series, the mean period (T_z) and mean wave height (H_m) were calculated. If done right, the mean period should equal the input (first-order) wave period of the wave generator and ideally mean wave height equals minimum, maximum and significant wave height, since the waves are monochromatic.

Wavelength (L), wave number (k) and wave celerity (C) were solved using the approximation of the wave dispersion relationship by Fenton and McKee (1990), which is given by

$$L = L_0 \left(\tanh \left[\left(\frac{4\pi^2 h}{gT^2} \right)^{3/4} \right] \right)^{2/3} \tag{3.5}$$

where L_0 is the deep water wavelength. Wave number is related to wavelength by $k = 2\pi/L$ and wave celerity is given by $C = L/T$. Since the offshore zone in the metronome is considered to simulate deep water conditions, the observed wavelength must equal deep water wavelength. Hence, for simplicity L_0 was calculated by the approximation of wavelength in deep water in the absence of surface tension effects, given by

$$L_0 = \frac{gT^2}{2\pi} \tag{3.6}$$

As waves transition from deep water to intermediate depth and shallow water their orbital motion reaches the bottom and generation of higher harmonic wave components due to non-linear wave-wave interaction occurs that add up to the first-order wave motion. Following second-order Stokes wave theory, the recorded wave shape in this zone therefore changes from perfectly sinusoidal to asymmetric. Wave non-linearity was parameterized by considering wave skewness (i.e. asymmetry about the horizontal axis, where crest wave height H_{cr} > trough wave height H_{tr}) and asymmetry (asymmetry about the vertical axis, forward-pitching of waves). Wave skewness was computed using the time series of free-surface elevation by

$$Sk = \frac{\overline{\eta(t)^3}}{\sigma_\eta^3} \tag{3.7}$$

where $\overline{n(t)}$ is the time-averaged free-surface elevation of the time series, which equals 0 if all waves within the time series are perfectly sinusoidal; and σ_η is the standard deviation of free-surface elevation, which equals $a/\sqrt{2}$ for sinusoidal waves. If waves become skewed, $\overline{\eta(t)^3}$ becomes increasingly positive, while σ_η^3 becomes smaller. Thus, for skewed waves with $H_{cr} > H_{tr}$, $Sk > 0$. Asymmetry is given in a similar way by

$$As = \frac{\overline{\mathcal{H}(\eta(t))^3}}{\sigma_\eta^3} \tag{3.8}$$

where $\boldsymbol{\mathcal{H}}(\eta(t))$ is the Hilbert transform of the free-surface elevation. If waves become increasingly pitched forward, ($\eta(t)$) becomes increasingly negative. Thus, for asymmetric waves that are pitching forward $As < 0$. The resulting wave shapes due to skewness and asymmetry are given in Figure 7.

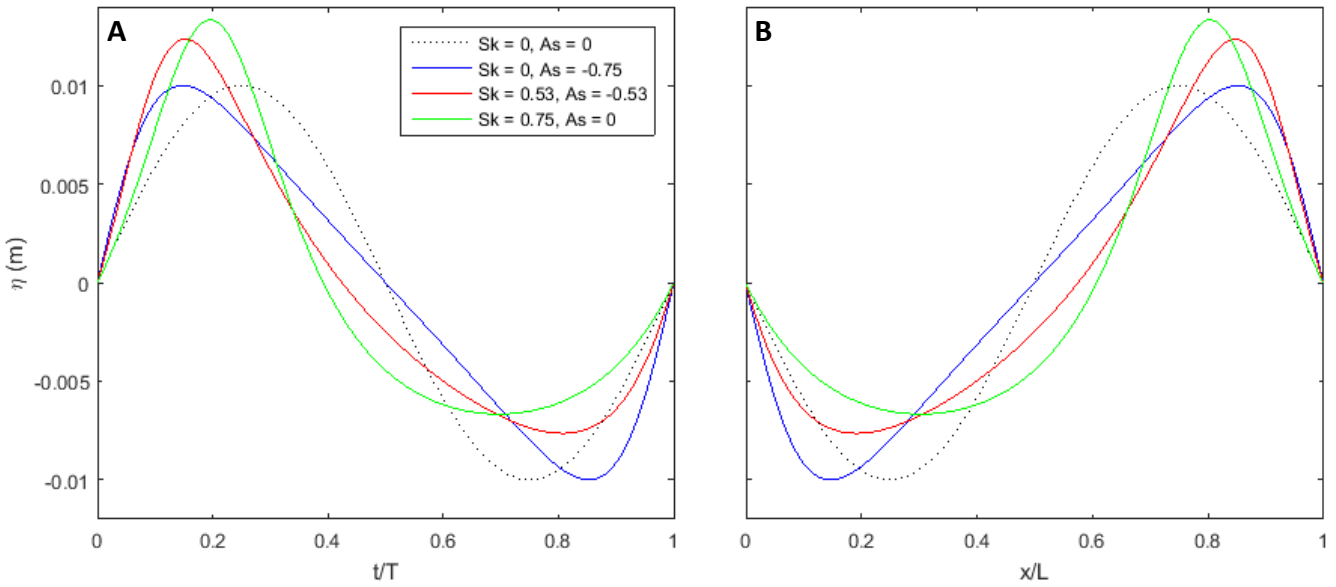

Figure 7. Wave shapes for different combinations of skewness and asymmetry. (A) as recorded in a time series and (B) along the length axis. The latter is a cross section of a single wave and clearly shows the forward pitching of asymmetric waves. Wave shapes were produced using the analytical approximate wave form by Abreu et al. (2010) with r = 0.6 and φ = 0 (asymmetric only); φ = -π/4 (skewed/asymmetric); and φ = -π/2 (skewed only).

The Ursell number (*Ur*) was used to parameterize skewness and asymmetry following the method of Doering and Bowen (1995). The Ursell number was computed by (Doering and Bowen, 1995)

$$Ur = \frac{3}{4}\frac{(ak)}{(kh)^3} \tag{3.9}$$

where a is the wave amplitude and h is water depth. A number of authors have derived empirical relations between the Ursell number and skewness and asymmetry (Figure 8). These fits are based on total non-linearity B given as (Ruessink et al., 2012)

$$B = \sqrt{Sk^2 + As^2} \tag{3.10}$$

And phase ψ given as (Ruessink et al., 2012)

$$\Psi = \tan^{-1}\left(\frac{As}{Sk}\right) \tag{3.11}$$

From empirical fits of B and ψ based on the Ursell number, skewness and asymmetry can be derived as $Sk = B \cdot cos\ \psi$ and $As = B \cdot sin\ \psi$. Based on this approach, the Ursell number relates to both the degree of non-linearity (through total non-linearity B) and to the partitioning into skewness and asymmetry (through the phase ψ). The empirical fits shown in Figure 8 were used to compare to the measured skewness, asymmetry and Ursell numbers in the Metronome (section 4.2). For further details on the parameters used in the fitted functions of B and ψ, see Eq. 4.7 and 4.9 in Doering and Bowen (1995); Eq. 9 and 10 in Ruessink et al. (2012); and Eq. 11 and 12 in Rocha et al. (2017), that expand on the parameterization of Ruessink et al. (2012) through additional dependence on offshore wave steepness, spectral bandwidth and beach slope.

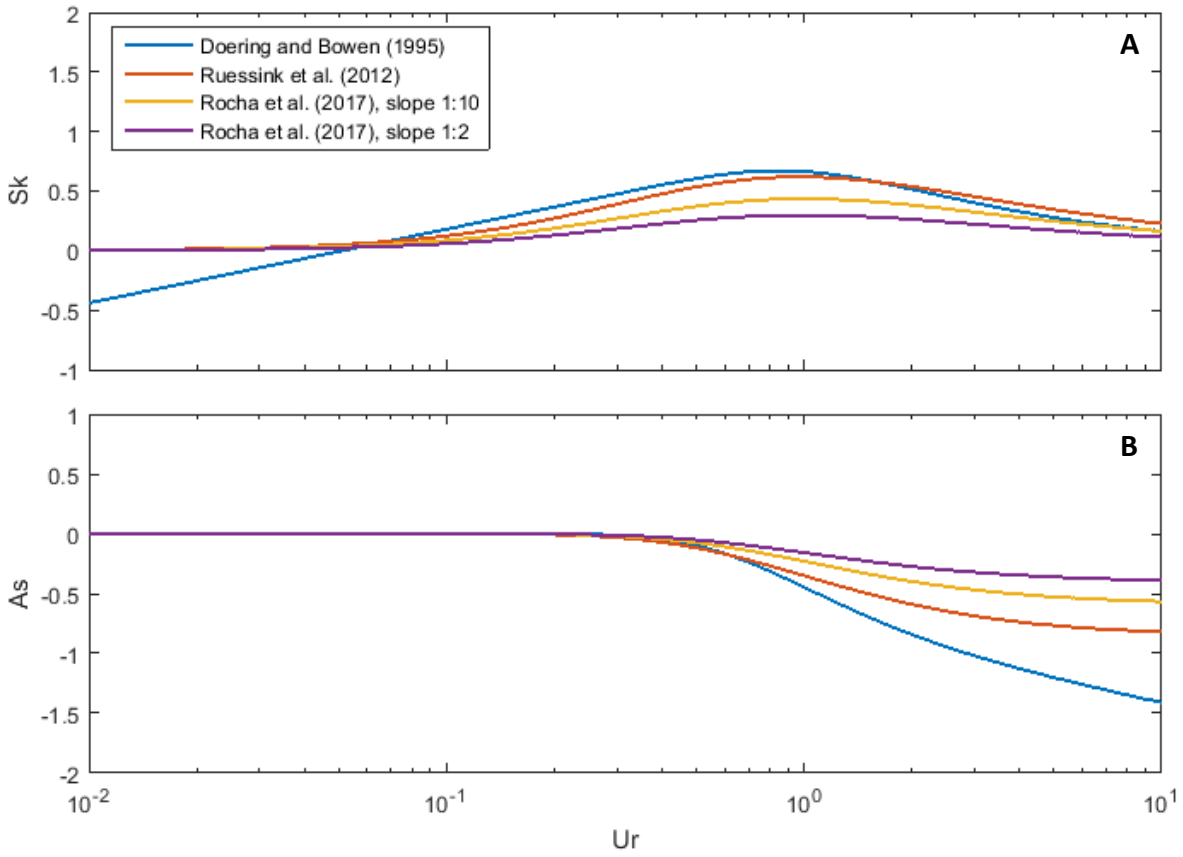

Figure 8. Empirical relations between the Ursell number, skewness (A) and asymmetry (B). The most recent parameterization by Rocha et al. (2017) includes additional dependence on offshore wave steepness, spectral bandwidth and beach slope. Two cases for beach slope are displayed here (1:10 and 1:2). Offshore wave steepness is based on a typical Metronome wave with H_0 = 0.01 m and L_0 = 0.25 m. Spectral bandwidth ≈ 0 as Metronome waves are monochromatic. Steeper beach slopes in combination with gentler offshore wave steepness appear to decrease the development of non-linear wave shapes.

3.4. Spectral analysis

The time-domain data was converted to the frequency domain by applying a fast Fourier transform, which was used to calculate the frequency-specific wave amplitude. No smoothing or filtering was required. Since the waves are monochromatic, smoothing of the frequency spectrum would only reduce accuracy of peak analysis. As opposed to random waves at sea, it is expected that peaks in the frequency spectrum are very narrow and that their non-zero width is only due to imperfections of the wave generator and/or sensor. Since wave non-linearity is characterized by the presence of (at least) a peak at twice the first-order wave frequency in the frequency spectrum, the magnitude of the first harmonic with respect to the first-order magnitude can be used as a measure of total wave non-linearity. This ratio is given by

$$A_r = a_{2f_p}/a_{f_p} \tag{3.12}$$

where f_p indicates the primary wave frequency and a is the corresponding amplitude. For fully linear waves, $A_r \approx 0$, whereas for non-linear waves $A_r >> 0$. The ratio was used to assess both wave-generator induced harmonics and harmonics due to wave-wave interaction. The former is represented by a value of $A_r > 0$ close to the wave generator, which decreases with distance from the wave generator in the absence of non-linear wave-wave interaction. As waves move into intermediate depth water, A_r increases due to generation of harmonics by non-linear wave-wave interaction. However, since A_r does not contain any phase information by itself, it does not

distinguish between non-linearity due to Skewness or Asymmetry. Hence, A_r is an equivalent of the total non-linearity parameter B (Eq. 3.10). Since A_r is based on the amplitudes of specific wave frequencies, as opposed to the entire spectrum, its use is limited to monochromatic waves.

3.5. Bed mobility

Sediment from the bed is mobilized if the maximum bottom shear stress ($\tau_{w,max}$) under a wave exceeds the critical shear stress (τ_{cr}) that is required to move the bed sediment. Hence, to apply a prediction of sediment mobility both $\tau_{w,max}$ and τ_{cr} need to be calculated from known wave parameters. It should be noted that the assessment of mobility only tells whether the sediment is mobilized and not what happens with entrained sediment (e.g. net transport). Since bottom shear stress can be expressed as a function of flow velocity, the maximum horizontal orbital velocity just above the thin boundary layer (U_w) must first be calculated. Following the method given by Soulsby and Smallman (1986), U_w was calculated using,

$$\frac{U_w}{a} = \frac{\omega}{\sinh(kh)} \tag{3.13}$$

where a is the wave amplitude, which for a monochromatic wave of near-constant height is given by $H_{mean}/2$, k is the wave number and h is the still water depth in m. In the absence of a steady current, the angular frequency ω is given by the dispersion relationship. Following the procedure outlined by Soulsby and Smallman (1986) and using a Newton-Raphson iteration, U_w was solved for a given time series (Soulsby, 2006).

Maximum bed shear stress under constant wave motion was estimated using the method described in (Nielsen, 1992), which combines maximum horizontal near-bed orbital velocity and a friction factor f_w,

$$\tau_{w,max} = 0.5\rho f_w U_w^2 \tag{3.14}$$

where f_w is given by,

$$f_w = exp\left[5.5\left(\frac{k_s}{d_0}\right)^{0.2} - 6.3\right] \tag{3.15}$$

where k_s is the Nikuradse roughness length, which equals $3D_{50}$ and d_0 is the wave orbital diameter, which is given in Masselink et al., (2011) as

$$d_0 = \frac{H}{\sinh(kh)} \tag{3.16}$$

Combining equation (3.16) and (3.15) with equation (3.14) yields the time-averaged maximum wave-induced shear stress for a given time series.

3.6. Application of scaling principles

Mean wave height and wave period at the seaward boundary of the Metronome were scaled up using Froude scaling for simulation in the SWASH model. As the contribution of surface tension and viscous boundary layer friction to wave dynamics is negligible, Weber and Reynolds scaling methods were not applied. Using a known model length scale ratio n_l and distortion factor (n_l/n_h) we can determine the associated wave period and wave height based on the scale ratio relationship given in Eq. (2.11) to maintain surfzone similarity. For scaling to prototype conditions, several length scales were considered (Figure 9). A length scale of 500 was chosen as a compromise between realistic wave parameters and ebb delta dimensions. E.g. at n_l = 500, mean offshore wave height is about 5 meters and the 'natural' ebb delta (i.e. not the small experimental delta for wave testing) in the

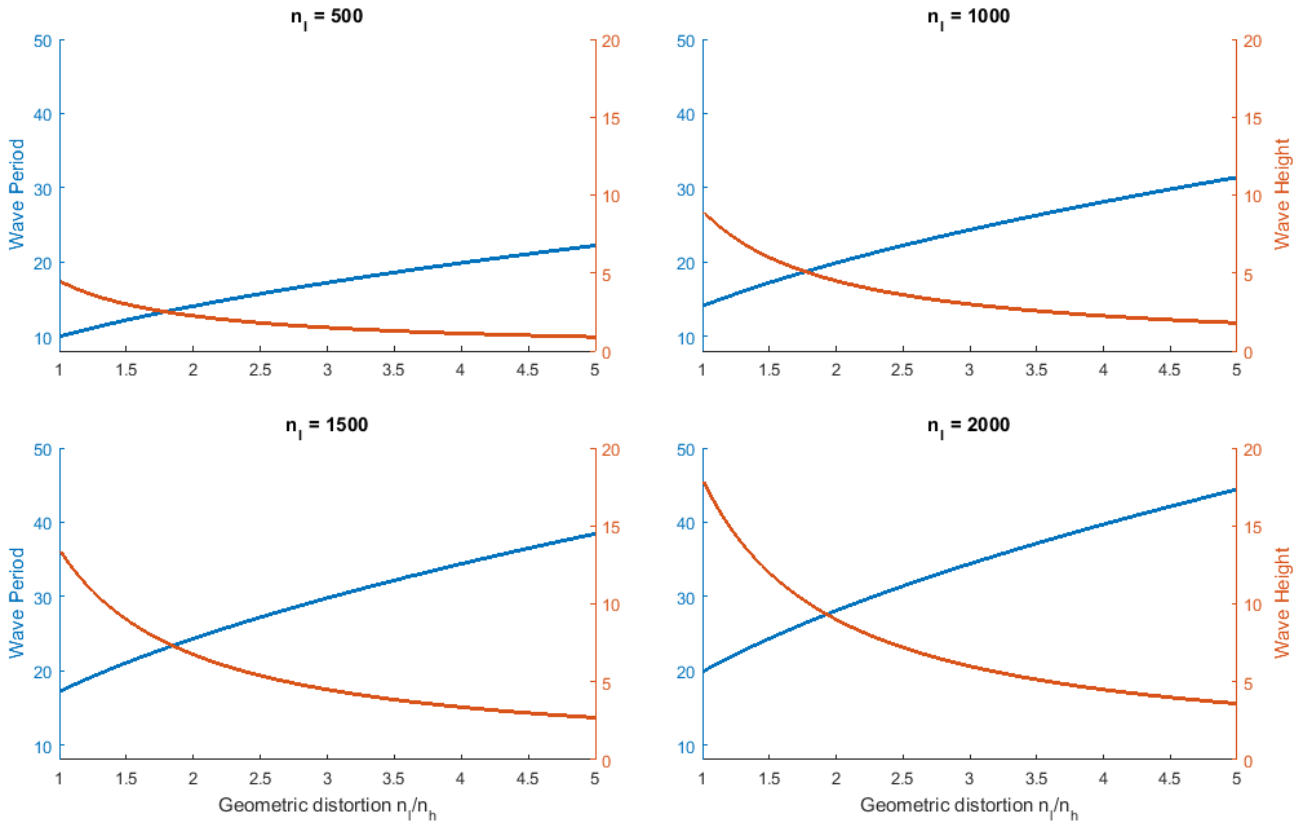

Figure 9. Effect of geometric distortion on the Froude scaling of a typical Metronome wave with H = 0.01 m and T = 0.5 s for several length scales. Note extremely high waves at scales larger than n_l = 500 for undistorted cases.

Metronome would expand about 1 kilometer into the sea, which is a realistic figure for a small estuary mouth in nature.

The Metronome model design choices are based on non-steady non-uniform flows that simulate tidal flow in an estuary, rather than short waves at the coast. Thus, a number of scale ratios are given and cannot be used for calibration of the prototype. Bed material and fluid properties in the metronome roughly correspond to the prototype. Hence for the metronome model the following conditions apply,

$$n_{\rho_w} = n_{\rho_s} = n_\nu = n_{D^*} = n_{k_s} = 1 \tag{3.17}$$

where we assume that Nikuradse roughness is only based on grain size in the absence of bedforms. This means that the requirement for similitude in dimensionless grain size and relative density are automatically met and can be used as a starting point. On the contrary, from Eq. (2.14) it follows that the relative length condition cannot be met since $n_\lambda \neq n_{D50}$ for any other scale except Metronome scale. Thus, from this perspective upscaling to a full-scale prototype must be based on non-fixed parameters such as wave properties and geometric distortion.

In order to maintain similitude of the Shields parameter the dimensional shear stress must be the same between prototype and model, which follows from combining Eq. (2.13) and (3.17). Thus, after combination with Eq. (3.14) it follows that

$$n_{\tau_{w,max}} = \frac{f_{w,pr} U_{w,pr}^2}{f_{w,m} U_{w,m}^2} = 1 \tag{3.18}$$

Both the friction factor (f_w) and the maximum near-bed orbital velocity (U_w) depend on wave properties through Eq. (3.16) and Eq. (3.13), respectively. Hence we can express shear stress as a

function of wave height, wave period, wave number and water depth, where the latter is related to the prototype to model length scale ratio by the distortion factor. Due the number of free variables an endless amount of combinations are possible to satisfy Eq. (3.18), making it impossible to solve mathematically or numerically. In addition, changing any of the above-mentioned parameters disregards Froude scaling, thus leading to flow characteristics not being in similitude. Since it is impossible to satisfy Eq. (3.18) while maintaining flow characteristics and surfzone similarity, sediment size has to be scaled in order to find a prototype situation that is in mobility similitude with the Metronome experiments.

In order to define mobility similitude, it is more useful to consider the difference between shear stress and critical shear stress at a given location and for a given sediment size rather than shear stress alone. This method makes comparing situations with different sediment sizes easier as the onset of mobility (i.e. when critical shear stress is exceeded) is represented by a single line regardless of sediment size. The difference between actual (measured or modelled) shear stress and critical shear stress using the dimensionless Shields number (Eq. 2.13) is given by

$$\theta_e = \theta - \theta_{cr} \tag{3.19}$$

where ϑ_{cr} is given by (Soulsby, 1997)

$$\theta_{cr} = \frac{0.3}{1+1.2D^*} + 0.055\left(1 - e^{-0.02D^*}\right) \tag{3.20}$$

Eq. (3.20) is plotted in Figure 10 below.

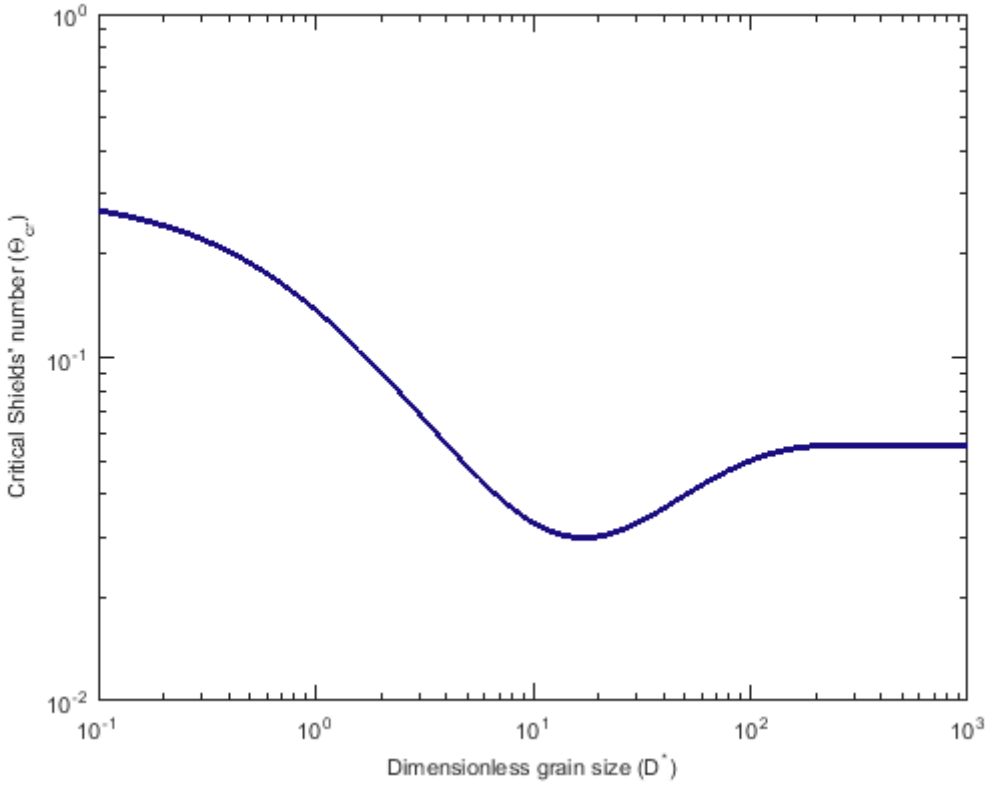

Figure 10. Dependence of critical Shields number on dimensionless grain size.

Critical Shields' number collapses to the line ϑ_e = 0, regardless of sediment size. Critical Shields' number is exceeded if $\vartheta_e > 0$. Mobility similitude requires that $n_{\vartheta e}$ = 1 between prototype and model.

In order to find how sediment size scales a least squares fit method was employed to find the best n_{D50} for which $n_{\vartheta e} \approx 1$.

3.7. Wave modelling

Waves were modelled after the wave experiments given in Table 1 both at Metronome and prototype scale using SWASH (Simulating Waves till Shore). The SWASH model is based on shallow water equations and non-hydrostatic pressure and is geared towards the simulation of surface waves and rapidly varying flows in coastal areas (Zijlema et al., 2011). Wave modelling was conducted at (1) 1:1 scale for all experiments and (2) at 1:500 prototype scale for experiment 4.

SWASH was employed in 1D mode. Hence only the seaward and landward boundaries are relevant for boundary conditions. Each cross-shore transect was replicated in SWASH by interpolating (measured) still water depth to a regular grid with dx = 0.02 m. Vertically, the water column was divided into three layers for computation. For the Metronome scale SWASH models, the most seaward located measured time series of each experiment was used to force movement of the water surface at the model's seaward boundary, ensuring maximum consistency between SWASH results and measured results. For the prototype model, wave height and wave period were computed by applying Froude scaling to the mean wave height and mean period of the most seaward located time series. The resulting prototype wave height and wave period were used as a regular (perfectly sinusoidal) input at the seaward boundary. The landward boundary was set to a radiative type, which effectively means that incoming waves decay to zero as they reach the coastline, rather than reflecting the remainder of each incoming wave. Each model run lasted for 400 seconds of simulated time with a time step of 0.005 seconds.

Turbulence was modelled using the Prandtl mixing length hypothesis, which was found to be the most useful method for breaking waves (Zijlema et al., 2011). As surface tension is likely to influence flow characteristics under breaking waves (Miller, 1972), a mixing length of 0.001 m was used, which is roughly equal to the capillary length of water. The mixing length was scaled proportionally to wave height (Zijlema et al., 2011) such that $n_{lm} = n_h$. Bottom friction was computed by the Colebrook-White formula using $k_s = 3D_{50}$ = 0.0018 m. The chosen roughness is only representative for the sandy bottom and not for the artificial grass bottom in the offshore zone since bottom friction is assumed to not affect waves in the deep water part of the basin.

Wave energy dissipation in the near shore is accounted for regardless of wave breaking parameters (Zijlema et al., 2011). However, the onset and total amount of energy dissipation may not be correctly modelled, especially when only a few (< 10) vertical layers are employed. SWASH uses the following criterium for the onset of wave breaking

$$\frac{d\xi}{dt} > \alpha\sqrt{gh} \tag{3.19}$$

where ($d\xi/dt$) is the vertical speed of the free surface and $\sqrt{gh}$ is the approximation of shallow water celerity. The parameter α is set to 0.6 by default, but was adjusted to fit energy dissipation in the 1:1 SWASH model to the measured time series. Wave breaking persists until

$$\frac{d\xi}{dt} < \beta\sqrt{gh} \tag{3.20}$$

where $\beta<\alpha$. ($d\xi/dt$) increases for waves approaching the shore as the wave front becomes steeper and hence vertical speed of the free surface increases at the wave front. Once ($d\xi/dt$) exceeds a fraction α of wave celerity, breaking is activated in the model until enough energy is dissipated such that ($d\xi/dt$) becomes smaller than fraction β of the wave celerity, thus creating a dynamic zone where breaking is accounted for. The default value of β is 0.2, but was adjusted in proportion to α to correctly represent energy dissipation due to wave breaking in the 1:1 SWASH model. In the 1:500 scale prototype SWASH model, default values for α and β were used.

The model output time series were treated in the same way as the measured time series from the Metronome. Thus. all calculations described in previous sections of this chapter were applied to the 1:1 and 1:500 scale SWASH output time series to calculate wave parameters, wave non-linearity and wave-induced mobility. This was done to ensure maximum consistency between measured and modelled parameters.

4. Metronome scale results and model

In this section, wave parameters based on measured results are presented as well as 1:1 modelled results for all conducted wave experiments (Table 1). Figure 11 gives a first glance overview of measured and 1:1 modelled results. Modelled wave trains follow measured results very well, especially in experiments 1 (Figure 11A) and 4 (Figure 11D). Both close to where the water level is forced to move in the model (to the right of position 1 in Figure 11) and further landward where waves have had time to develop freely (positions 2 and 3), there are no major discrepancies between measurements and model in both wave dimensions and shape.

4.1. Wave dimensions

In the first straight coast experiment (1) with a 1:10 bottom slope (Figure 12), wave height remains nearly constant at H_m = 0.6 cm from the wave generator until x = 10 cm, where $z \approx 2 \approx 0.06L_0$. Wave height appears to rise slightly just before x = 10 cm, an effect that is also captured by the model. After x = 10, wave height decreases rapidly towards capillary height as the waves lose energy. The surfzone similarity parameter is ξ = 0.7, implying that breakers are plunging. Model calibration for energy loss due to breaking required α = 0.08 and β = 0.04, i.e. the onset of breaking is initiated at a much gentler wave front than default. 1:1 Modelled mean wave height corresponds very well to the Metronome results.

In the second straight coast experiment (2) with a 1:10 bottom slope (Figure 13), offshore wave height shows slightly more variation compared to experiment 1. The variation appears to be random. The shorter-period waves have a smaller wavelength and a higher mean wave height of H_m = 1.2 cm compared to experiment 1. Wave height raises slightly up to H_m = 1.5 cm between x = 20 and 15. After x = 15, where $z \approx 2 \approx 0.08L_0$, waves lose energy due to breaking and wave height declines rapidly towards 0. The surfzone similarity parameter is ξ = 0.45, implying that breakers are spilling. The onset of breaking was calibrated with α = 0.4 and β = 0.2, which is much closer to the default values of 0.6 and 0.3, respectively. Modelled results do not show shoaling just before breaking commences as opposed to the model results of experiment 1. Furthermore, wave height declines from x = 20 onwards, well before the measured wave height declines.

In the third straight coast experiment (3) with a 1:5 bottom slope (Figure 14), only a smaller section closer to the shore was focused on. Wave height remains constant around H_m = 1.2 cm for the first 40 cm over the coastal profile, assuming variation in measured wave height is random. There is no clear indication of wave height increase just before breaking. Wave height decreases from x = 10 onwards, where $z \approx 2 \approx 0.08L_0$. The surfzone similarity parameter is ξ = 0.9, implying that breakers are plunging. Breaking was calibrated by using α = 0.4 and β = 0.2. Despite calibration efforts, the development of modelled wave height does not follow measured results, with wave height not declining before x = 8 cm.

In experiment 4 waves propagated over an experimental ebb-delta (Figure 15). Offshore wave height is near-constant with H_m = 0.9 cm. Starting at around x = 50, wave height increases slightly before declining rapidly at x = 42. Over the shallow area behind the delta front after x = 30, wave height no longer declines and is stable at H_m = 0.1 cm. The surfzone similarity parameter is ξ = 4.2, implying that breakers come in as bores. Breaking over the delta's terminal lobe was calibrated by using α = 0.2 and β = 0.1. However, although the onset of wave height decline seems to correspond between model and measurements, wave height declines faster according to measurements. Furthermore, modelled wave height on top of the delta remains about twice as high as measured. In this part of the delta, modelled wave height appears to vary at a regular interval of 7 cm in what appears to resemble a reflection pattern with nodes and antinodes.

Overall, wave height development along the profile matches 1:1 SWASH model results very well, especially in experiments 1 and 4. The onset of wave breaking and hence wave height decrease generally occurs when $z = 0.05 – 0.08L_0$. Wave breaking is in most cases preceded by a short wave shoaling stage where wave height locally increases. However, the latter could not be captured in

model results of 2.5 Hz wave experiments (2 and 3). Calibration of breaking parameters required much lower threshold values α and β for the 2 and 2.25 Hz wave experiments (1 and 4 respectively).

Table 2. Wave and wave breaking parameters of Metronome Waves

parameter	Exp. 1	Exp. 2	Exp. 3	Exp. 4
Offshore mean wave height, $H_{m,0}$ (m)	0.006	0.012	0.012	0.009
Onset of breaking at depth z (m)	0.02	0.02	0.02	0.015
Onset of breaking at fraction of L_0	$0.06L_0$	$0.08L_0$	$0.08L_0$	$0.05L_0$
Surfzone similarity parameter ξ (-)	0.7	0.45	0.9	4.2
Breaker type	Plunging	Spilling	Plunging	Surging
Breaking activation parameter α (-)	0.08	0.4	0.4	0.2
Breaking deactivation parameter β (-)	0.04	0.2	0.2	0.1

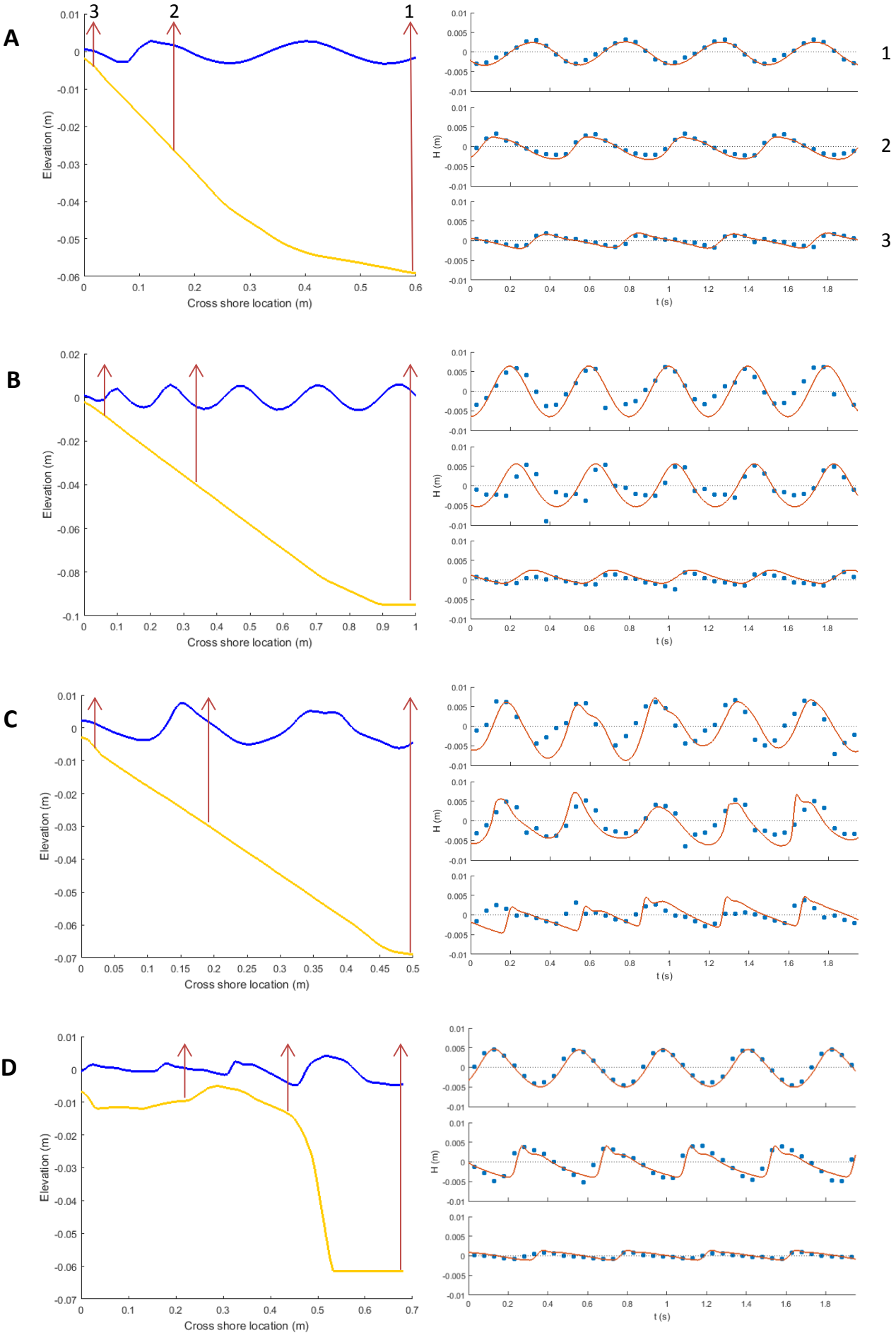

Figure 11. Overview of waves experiments 1 (top) through 4 (bottom). Left column: Snapshot of waves and bottom profile. Right column: Example of time series from the 1:1 SWASH wave model at indicated positions 1 (seaward), 2 and 3 (landward). Blue dots are measured results from the Metronome.

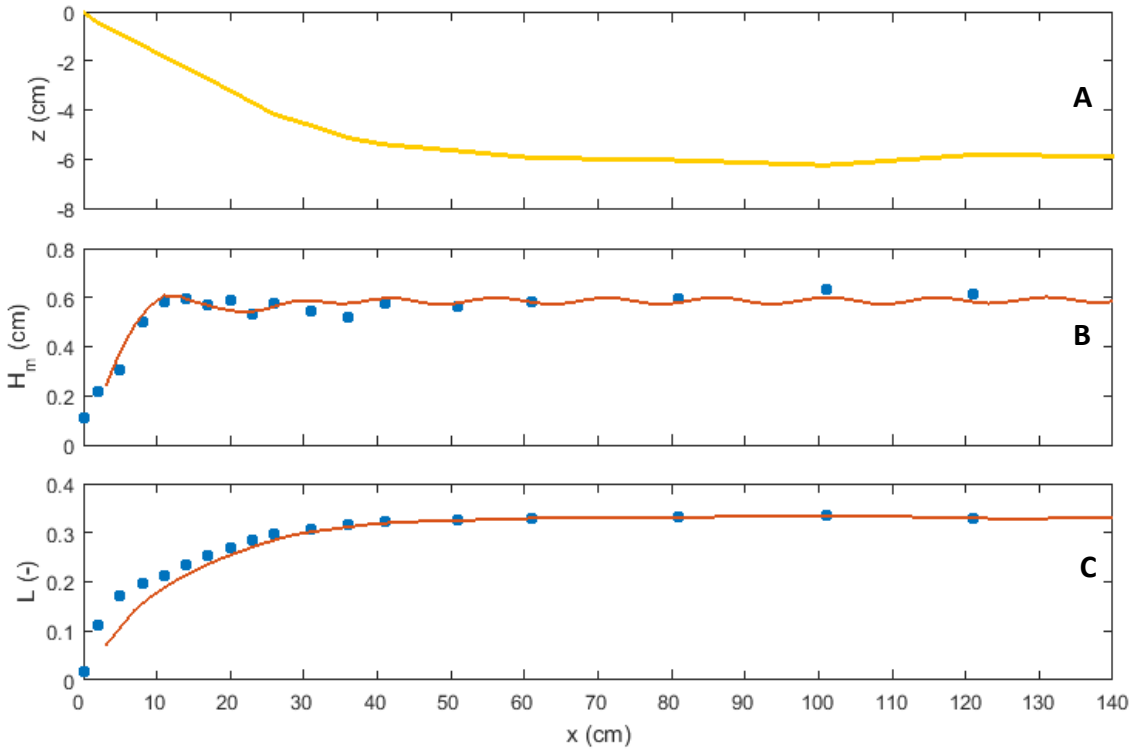

Figure 12. Experiment 1 (1:10 slope straight coast, 2 Hz waves) bottom profile (A); Wave height (B); and wavelength (C)

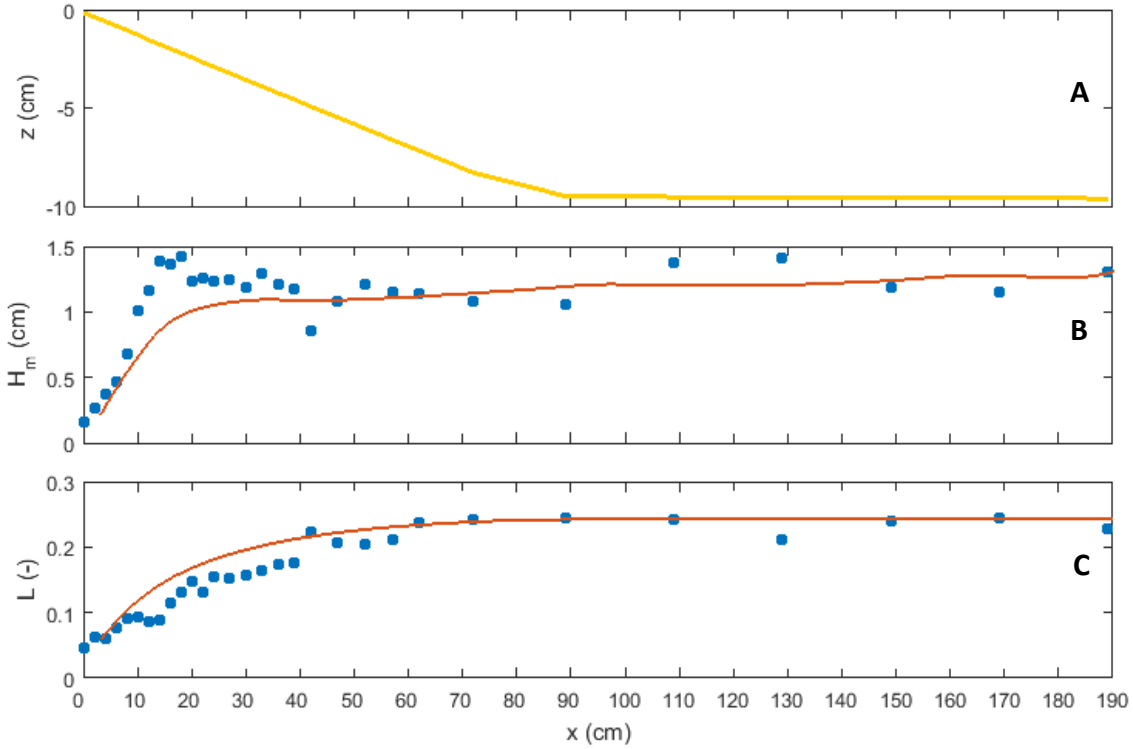

Figure 13. Experiment 2 (1:10 slope straight coast, 2.5 Hz waves) bottom profile (A); Wave height (B); and wavelength (C)

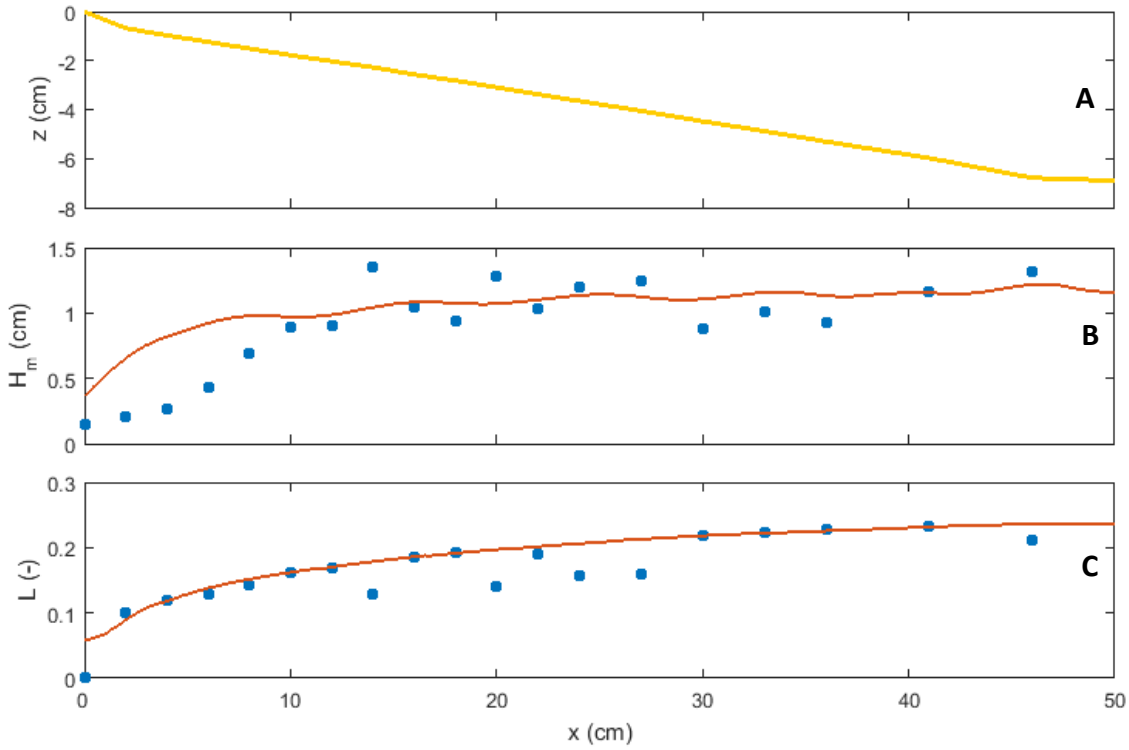

Figure 14. Experiment 3 (1:5 slope straight coast, 2.5 Hz waves) bottom profile (A); Wave height (B); and wavelength (C)

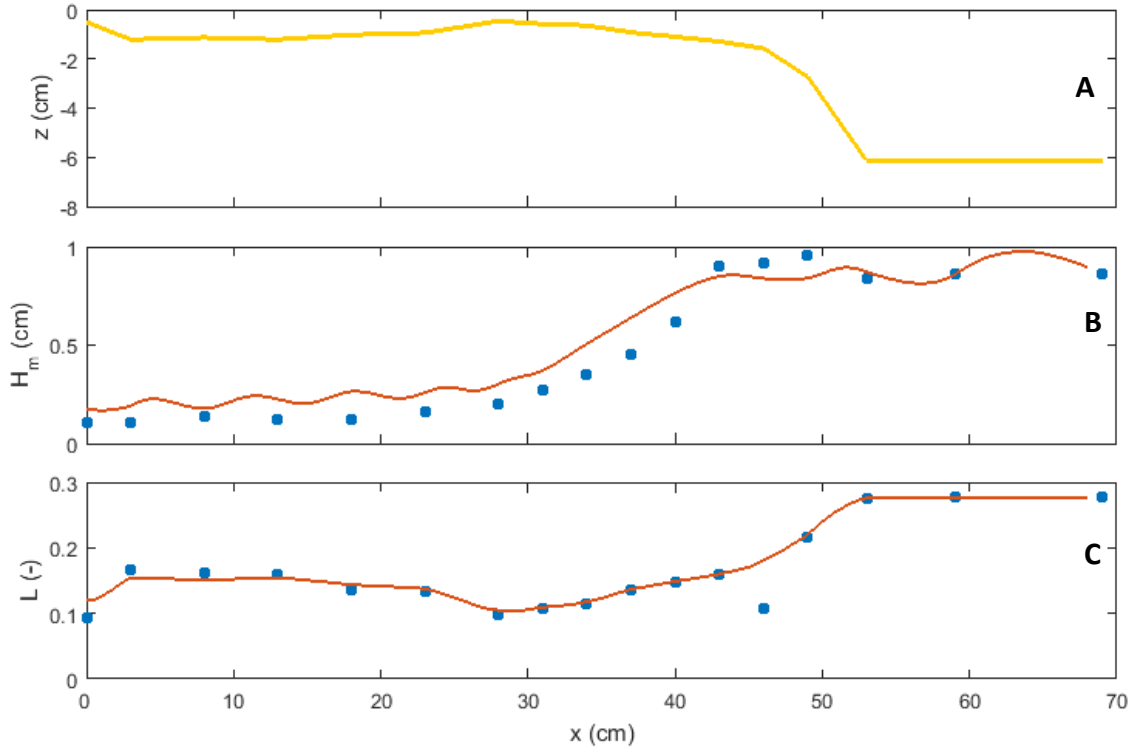

Figure 15. Experiment 4 (simplified delta, 2.25 Hz waves) bottom profile (A); Wave height (B); and wavelength (C)

4.2. Wave shape and non-linearity

In this section, measured and 1:1 modelled wave shape is described by wave skewness (*Sk*), asymmetry (*As*) and total non-linearity based on the ratio between the second order and first order wave amplitude (*Ar*). An overview of frequency spectra for each experiment for an offshore (undeveloped non-linearity) and an onshore (largely developed non-linearity just before wave breaking) location is presented in Figure 16.

In experiment 1 (Figure 17), skewness varies between 0.5 and -0.2 in the offshore zone. There appears to be a trend of increasing wave skewness starting at x = 30 with skewness reaching up to 0.5 at x = 10. Skewness subsequently decreases towards negative values after x = 5. Model results show less variation in skewness with values around 0 along the entire profile. Asymmetry shows a more consistent result with little variation in measured data and an almost perfect match with modelled results. Waves are not asymmetric in the offshore zone and only become asymmetric between x = 30 and x = 10 where *As* reaches -1, thus developing at the same time as wave skewness. Maximum asymmetry at x = 10 concurs with maximum wave height just before wave height decreases due to breaking. Total non-linearity close to the wave generator is about 0.2 and decreases steadily until second order wave amplitude is negligible at x = 30, such that $Ar \approx 0$. Total non-linearity increases towards the coast until reaching Ar = 0.6 at x = 8 and declines to 0.2 towards the shore. Maximum total non-linearity is reached just after the onset of breaking. Modelled results for the total non-linearity parameter suggest that there is no non-linearity in the offshore zone. Towards the coast where modelled asymmetry rises, total modelled non-linearity follows the rising trend, but underestimates the magnitude of *Ar* with respect to measured results.

In experiment 2 (Figure 18), skewness behaves erratically with $Sk < 0$ in the near-shore zone between x = 20 and the landward boundary (i.e. orbital velocity below the wave trough is higher than below the crest). Model results, however, suggest the expected development of positive wave skewness in the near shore. Measured wave asymmetry is very much scattered, with *As* varying between 0.5 and -0.5 in the offshore zone. There seems to be a trend of increasing asymmetry (*As* becomes smaller) between x = 30 and the landward boundary, but not nearly as distinctly recognizable as in experiment 1. Total non-linearity as a result also shows more variation in the offshore zone. A clear increase of total non-linearity already starts at x = 40, but the presence of such a high second-order wave is difficult to relate to skewness and asymmetry that have not yet been developed at this point. Maximum non-linearity is reached at x = 15, which is where waves begin to break. Model results show a similar development but with maximum Ar = 0.25 as opposed to Ar = 0.8 at x = 15.

In experiment 3 (Figure 19), both measured and modelled skewness show much variation with a weak trend of increasing skewness towards the landward boundary, reaching up to Sk = 0.5. Asymmetry varies around 0 and starts increasing (*As* decreases) from x = 20 onwards, reaching -0.5 close to the landward boundary. Model results for asymmetry follow the same development as measured results, but with *As* reaching -1 close to the landward boundary. Total non-linearity based on measurements varies between 0 and 1, show no clear trend. Modelled total non-linearity is lower than that of measured results, similar to experiments 1 and 2.

In the final delta experiment (4) (Figure 20), wave non-linearity parameters show more consistency for both measured and modelled results. Wave skewness is around 0 in the offshore zone and remains unaltered upon reaching the delta terminal lobe. Only behind the terminal lobe at x = 30, skewness slowly increases and reaches 0.5 at x = 10. Model results show a similar development of wave skewness, but show a strong variation causing skewness to vary between 0 and 1 between x = 30 and the landward boundary at a 7 cm interval. Asymmetry is around 0 in the offshore part of the profile, but waves quickly develop asymmetry upon reaching the terminal lobe between x = 50 and x = 40. Behind the terminal lobe at x = 30, waves become less asymmetric and eventually at the landward boundary $As \approx 0$. Model results for asymmetry show a similar pattern of development, but reach As = -1 on the terminal lobe, whereas asymmetry based on measured results reaches a

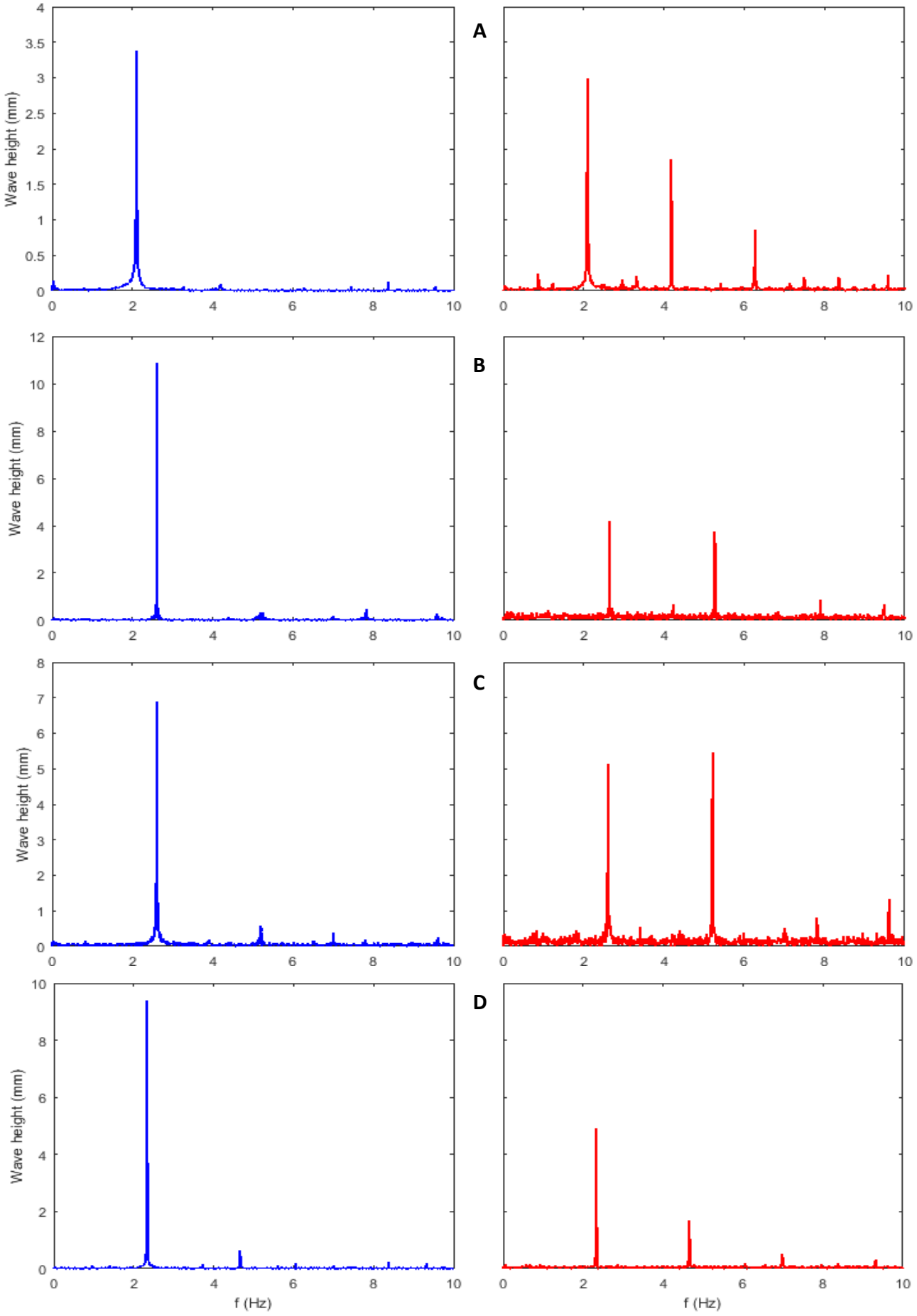

Figure 16. Frequency spectra with wave height along the y-axis. For each experiment (A, experiment 1; B, experiment 2; C, experiment 3; and D, experiment 4) an example of undeveloped wave non-linearity (low *Ar*, left column) and (fully) developed wave non-linearity (high *Ar*, right column). Note narrow spectral bandwidth as expected for monochromatic waves. Clear development of first (at $2f_p$) and sometimes second (at $3f_p$) higher harmonics visible.

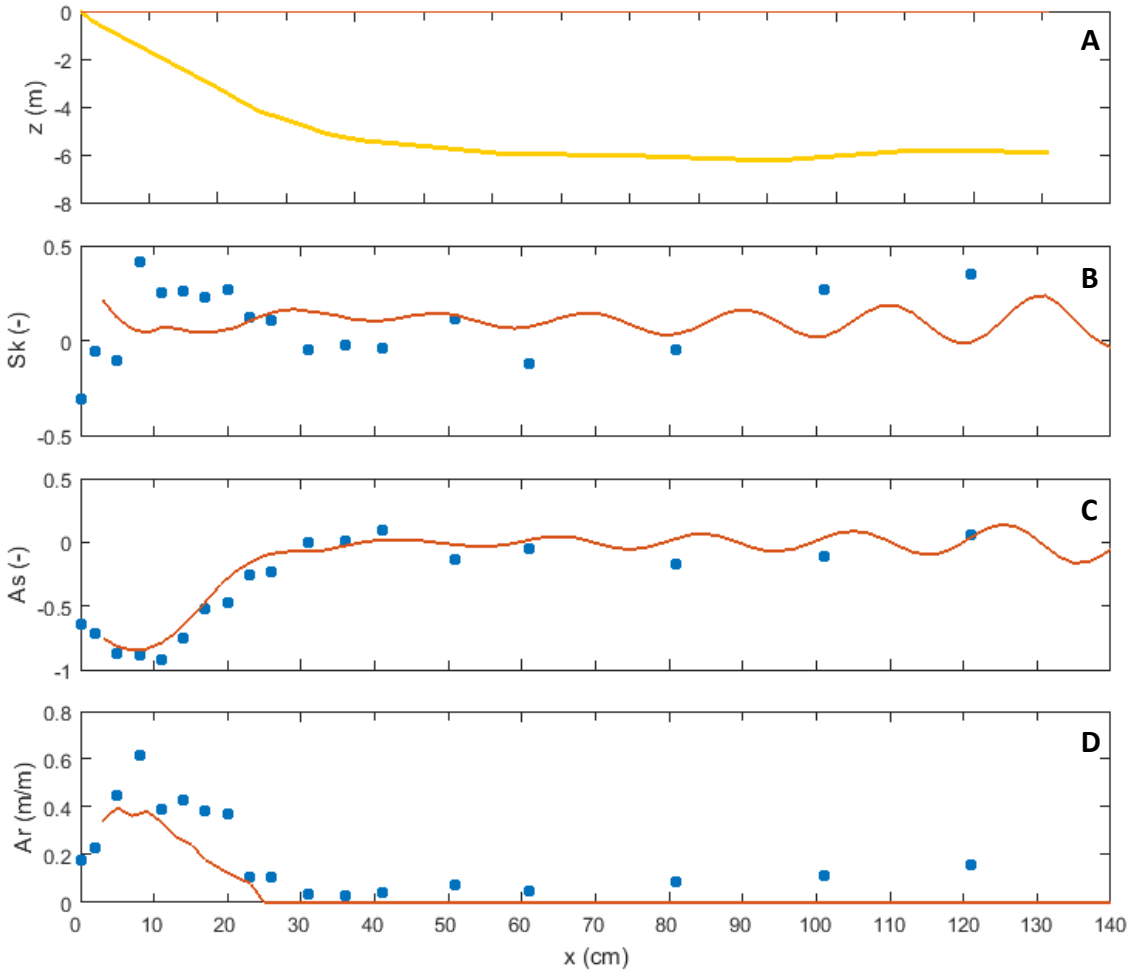

Figure 17. Experiment 1 (1:10 slope straight coast, 2 Hz waves) bottom profile (A); Skewness (B); Asymmetry (C); and total non-linearity (D)

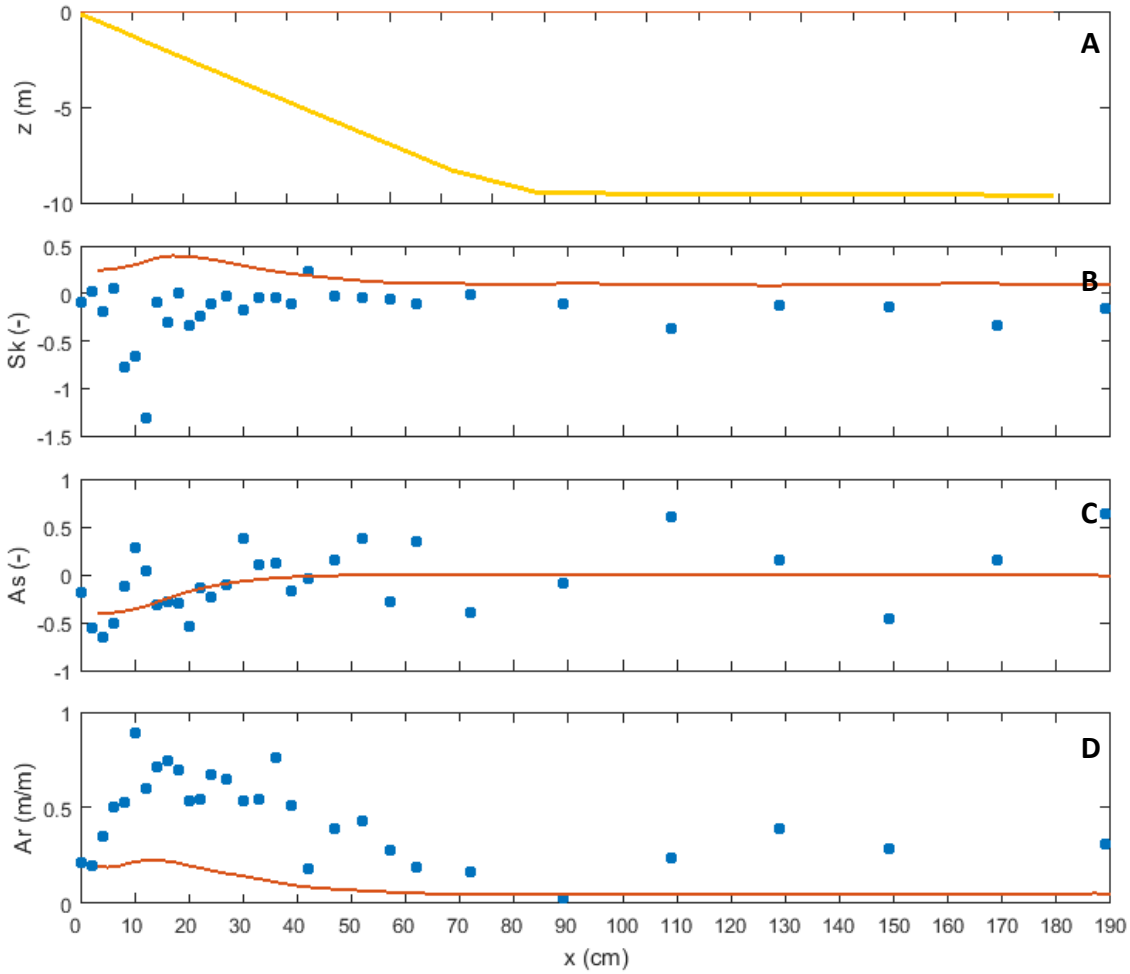

Figure 18. Experiment 2 (1:10 slope straight coast, 2.5 Hz waves) bottom profile (A); Skewness (B); Asymmetry (C); and total non-linearity (D)

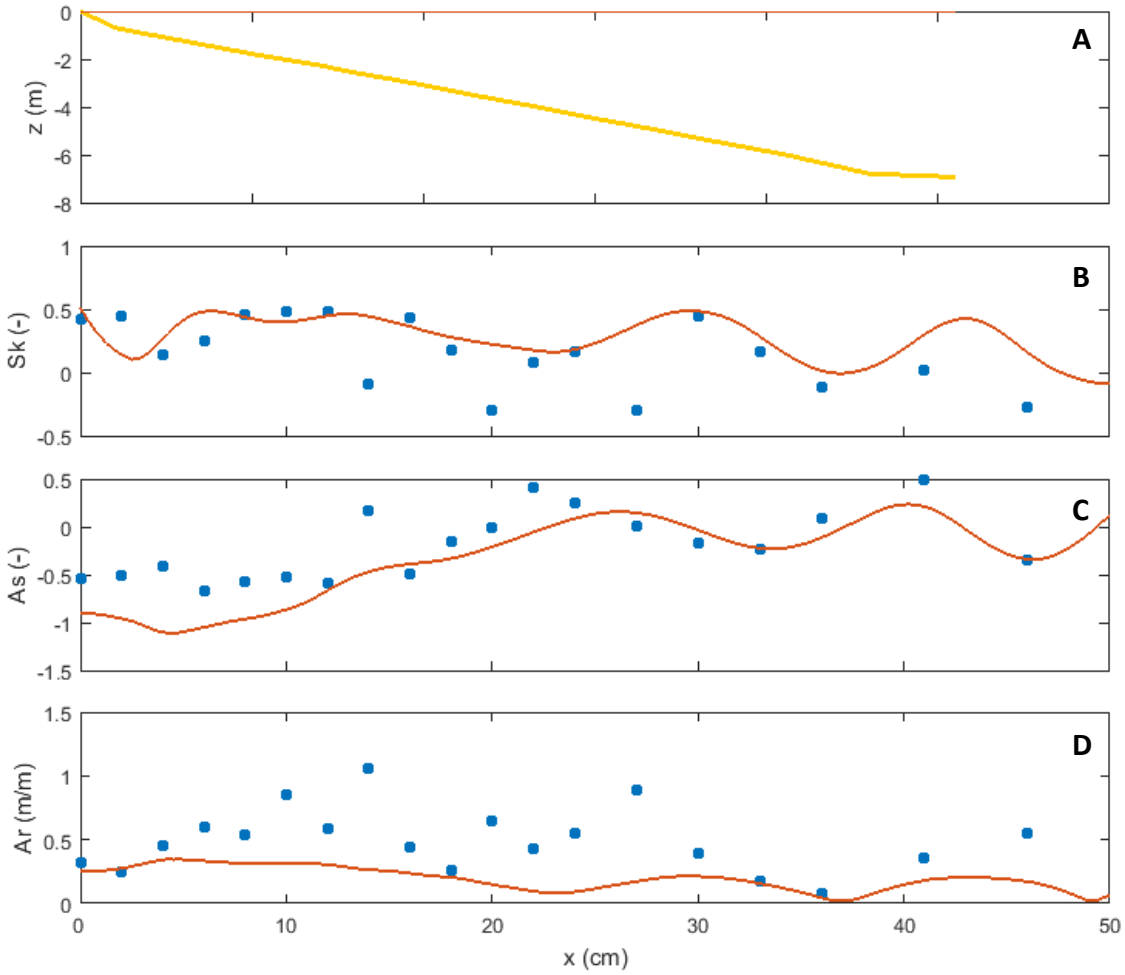

Figure 19. Experiment 3 (1:5 slope straight coast, 2.5 Hz waves) bottom profile (A); Skewness (B); Asymmetry (C); and total non-linearity (D)

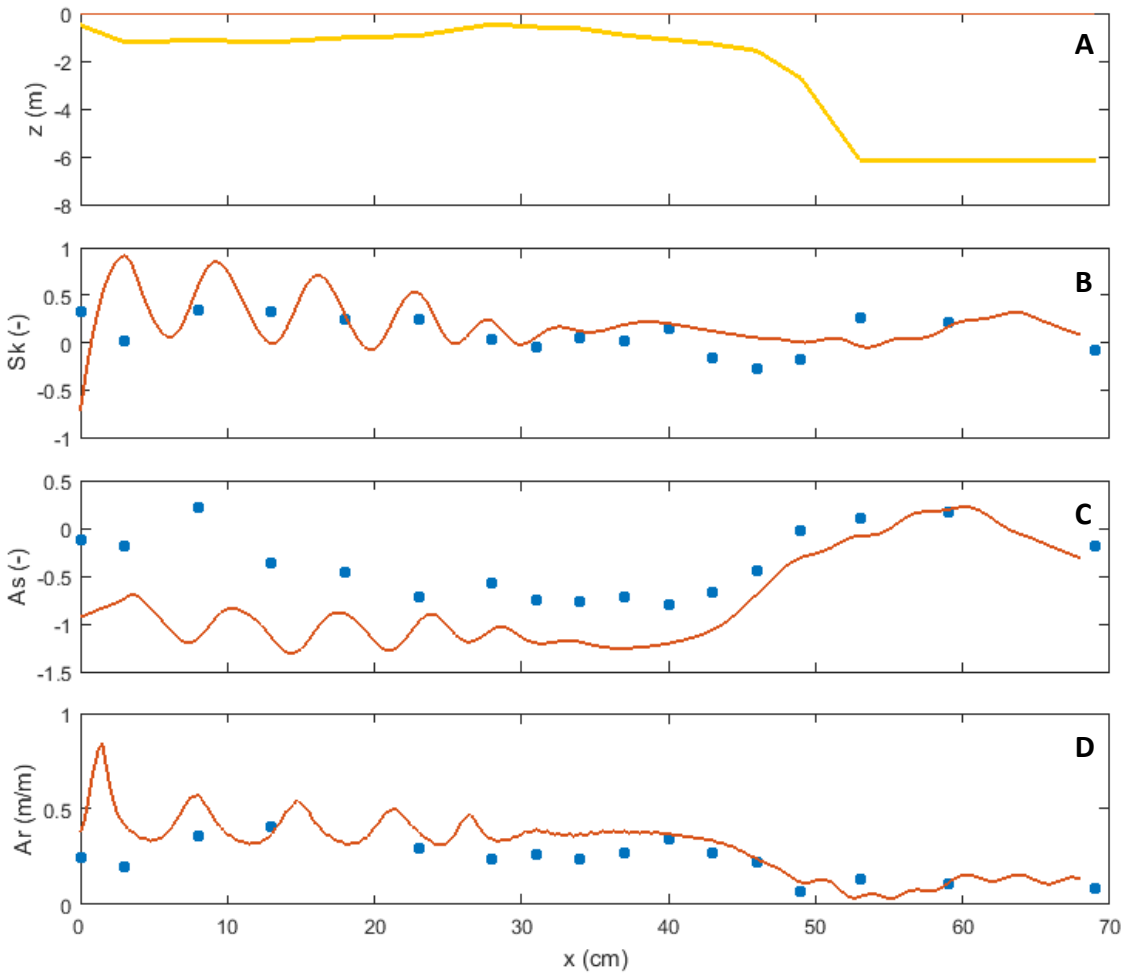

Figure 20. Experiment 4 (simplified delta, 2.25 Hz waves) bottom profile (A); Skewness (B); Asymmetry (C); and total non-linearity (D)

minimum of *As* = -0.6 at the same location. Moreover, asymmetry behind the terminal lobe does not disappear with *As* remaining about -1 between *x* = 30 and the landward boundary. Like skewness, model results show a feedback effect causing asymmetry to vary strongly around -1 behind the terminal lobe at a regular 7 cm interval. Total non-linearity indicates that wave non-linearity begins to develop at *x* = 50 where *z* = 0.044 m and reaches up to 0.3 at *x* = 40 after which *Ar* remains constant up to the landward boundary. Modelled total non-linearity matches measured results well, but shows the same feedback behaviour between *x* = 30 and the landward boundary. The feedback effect is most likely caused by enhanced triad wave-wave interactions and subsequent oversteepening and dissapation of the higher harmonics, which also causes the slow decay of wave height over the ebb delta seen in Figure 15B.

Wave shape parameters show the most consistent results in the lower wave frequency wave experiments (1 and 4, 2 and 2.25 Hz respectively). In experiment 2 and 3, trends in wave shape parameters are less pronounced than in experiments 1 and 4. It generally appears that maximum wave asymmetry is reached just before the onset of wave breaking, after which waves become less asymmetric. Skewness gives the most variation along the cross-shore profiles and cannot be used to reliably derive any trends. Total non-linearity develops along with increasing skewness and asymmetry and is highest just before the onset of breaking, similar to asymmetry.

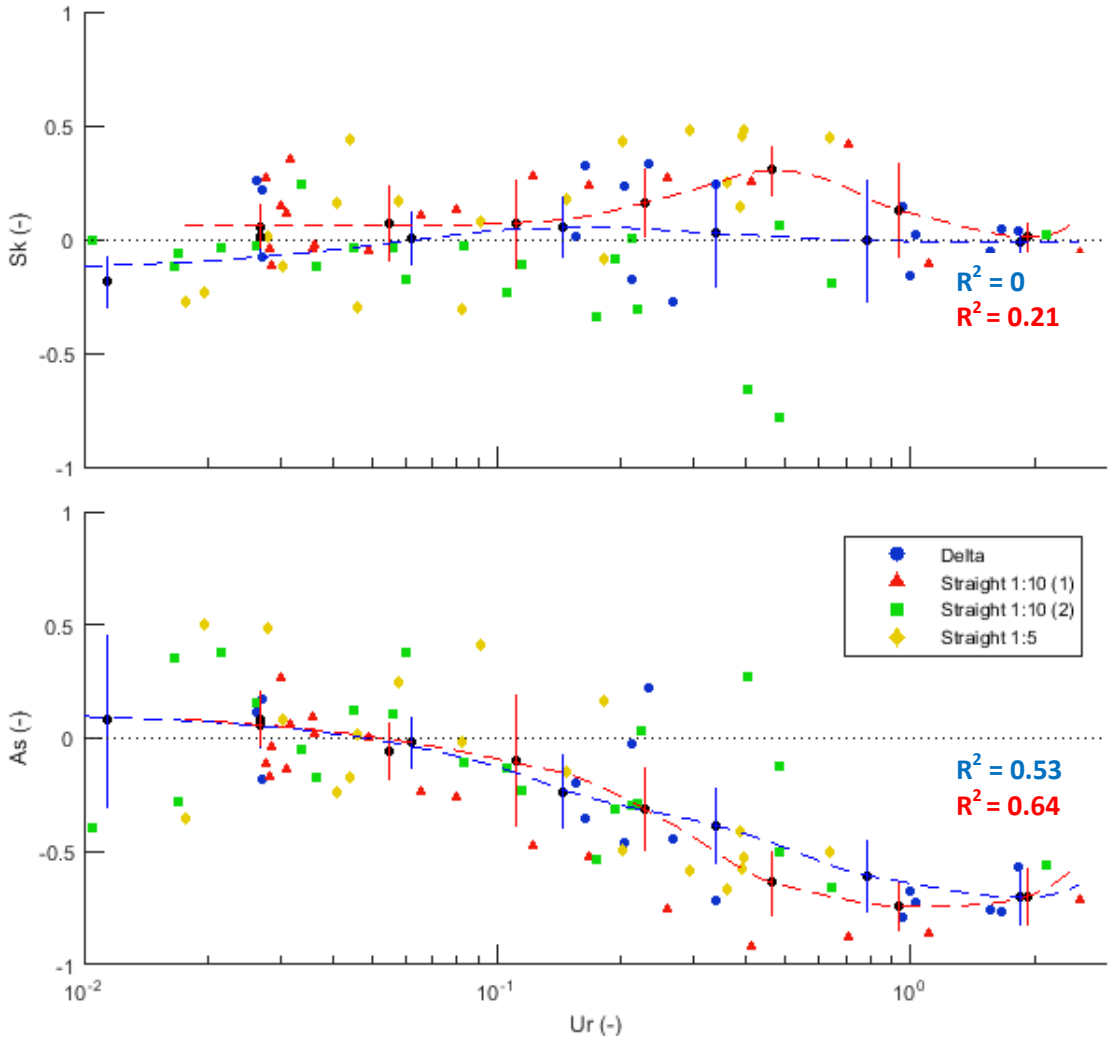

Figure 21. Wave skewness *Sk* and asymmetry *As* as a function of the Ursell number *Ur.*Trends were derived by applying a moving average filter with a total of eight windows. Vertical bars indicate the 95% confidence interval around the local mean value of each window. Blue trend is based on all data; red trend is based on all data except 1:10 straight coast 2 data (Exp. 2, green squares). Non-linearity mainly partitions into asymmetry, whereas skewness shows no real development towards greater non-linearities, but a very minor development if 1:10 straight coast 2 data is omitted.

The relation between skewness, asymmetry and the Ursell number is given in Figure 21. Skewness shows no trend and large standard deviations, especially for $0.1 < Ur < 1$ where development of skewed wave shapes is expected based on the parameterizations that are plotted in Figure 8 and Figure 22 (the latter alongside our trends). The result suggests that non-linearity is mainly partitioned into asymmetry, which clearly decreases for $Ur > 0.1$ and shows much less variation. It appears from the cross-shore development and from **Error! Reference source not found.** that development of skewness is much less pronounced, whereas asymmetry develops as wave non-linearity progressively increases. Omitting the results of the second 1:10 straight coast experiment results in slightly improved regressions as is evident from the higher R^2 values.

Significance of our data in comparison to the parameterizations from literature was tested by applying a paired sample t-test using observed and predicted values of *Sk* and *As*. It follows that at a significance level of $\alpha = 0.01$, none of the parameterizations shown in Figure 22 can be explained by our dataset as $p << \alpha$ in all cases. In other words: we can say at a confidence level of over 99% that the parameterizations from literature do not apply to our dataset. Thus, also given the limited number of samples ($n = 82$ and $n = 53$ if data from experiment 2 is omitted) and the large amount of variation in skewness and asymmetry, the observed data and their indicated trends merely show that there is a significant difference between observations and parameterizations of skewness and asymmetry, rather than giving an accurate representation of how non-linearity in the Metronome develops.

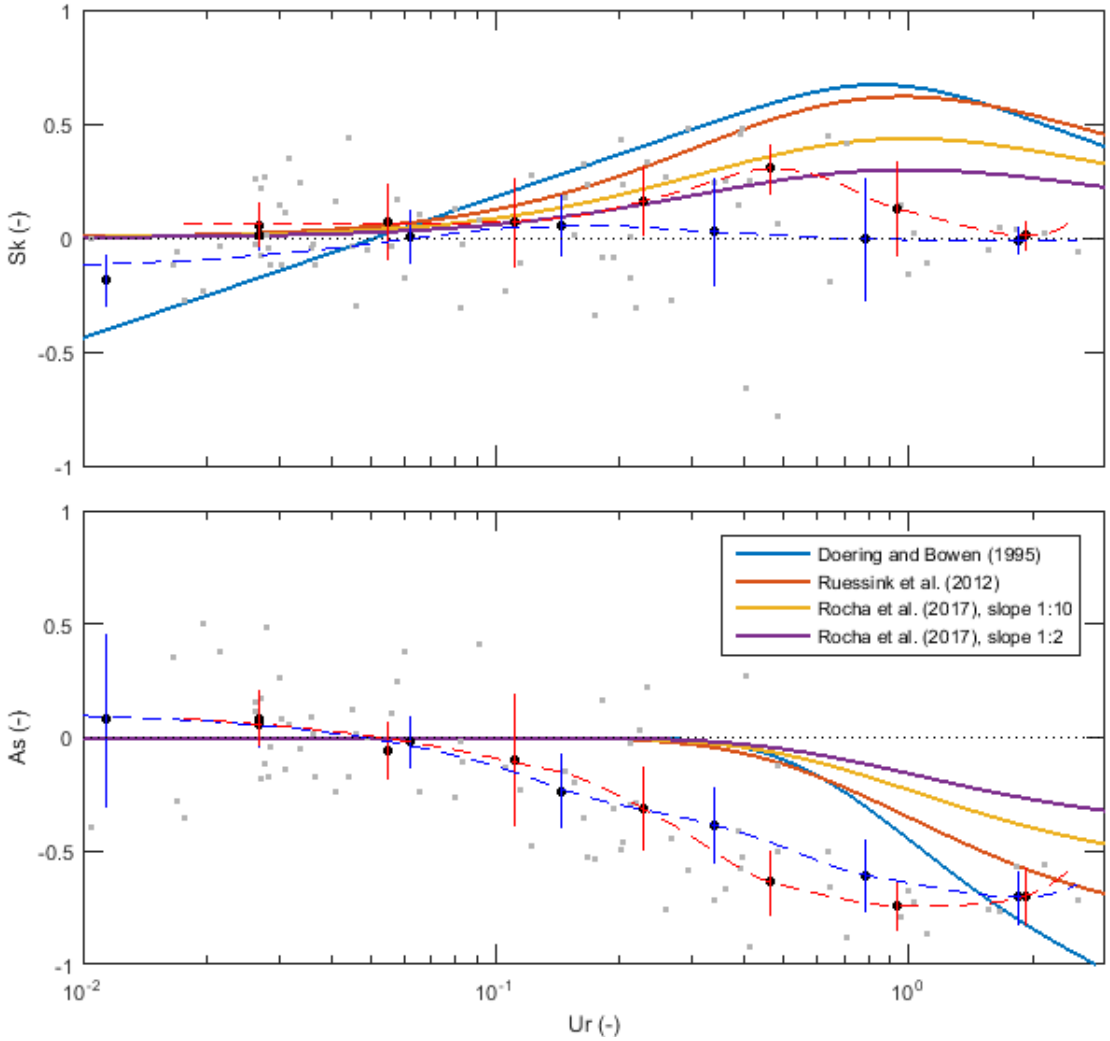

Figure 22. Parameterizations of skewness and asymmetry (see also Figure 8) in comparison to observed data and the trends based thereon. Grey points represent the same observed data as in Figure 21. The difference between observed data and all four parameterizations is statistically significant at *p*-values of less than 0.01 for both skewness and especially asymmetry.

4.3. Sediment mobility

In all wave experiments, offshore $U_w > 0$, suggesting that water is still shallow enough (intermediate depth) to feel some effect of the waves at the bottom. Offshore $U_w \approx 0.03$ m/s for all experiments, hence this effect is insignificantly small. Maximum near-bed orbital velocities of up to 0.1 – 0.15 m/s are generally reached at the point where waves start breaking and wave height starts declining (x = 10-15 for straight coast experiments 1-3 and at x = 45 in experiment 4). Measurements and model results are a close match in the offshore zone, but in the near-shore zone modelled results typically deviate from measurements for both maximum near-bed orbital velocity and Shields number, the latter being calculated directly from the maximum near-bed orbital velocity.

In experiment 1 (Figure 23), the peak Shields number at x = 10 never exceeds the critical Shields number ϑ_{cr} = 0.03. This agrees with the observed lack of movement at the bed throughout the experiment. Only the smallest fraction of grains was mobilized around x = 10, but was not enough to make any significant change to near-shore bed morphology. Model results give a similar cross-shore development of Shields number, but fail to capture decreasing mobility past x = 10.

In experiment 2 (Figure 24), $\vartheta > \vartheta_{cr}$ for the entire zone between x = 40 and the landward boundary. Peak mobility was computed under orbital velocities in excess of 0.15 m/s at the point where waves begin to break. During the experiment, sediment was visibly moving and a small swash-aligned submerged offshore bar was formed at x = 15. Model results show a similar development of mobility, but with underestimated Shields numbers, causing the mobile zone where $\vartheta > \vartheta_{cr}$ to start at x = 25. Furthermore, peak mobility is much lower than was computed from measured wave parameters.

In experiment 3 (Figure 25), $\vartheta > \vartheta_{cr}$ for $10 < x < 30$, with maximum mobility at around x = 15. Model results behave in a similar way as in experiment 1, with Shields number continuing to rise beyond the point where Shields number based on measurements reach their maximum. In the model $\vartheta > \vartheta_{cr}$ for $x < 15$, hence the zone where sediment is mobile only has a small overlap with the mobile zone based on measurements. During the experiment, a swash-aligned bar formed at x = 15, similar to the one formed in experiment 2.

In experiment 4 (Figure 26), sediment is mobile for $40 < x < 50$, with a distinct peak in mobility at x = 46. Peak mobility occurs just before waves begin to break and lose height at x = 42. The Shields number decreases exponentially and reaches a stable ϑ = 0.002 – 0.003 at x = 15, which is well behind the ebb delta terminal lobe. Modelled results suggest that the mobile zone is located between x = 45 and x = 35, which is 5 cm landward compared to the location of the mobile zone based on measured results. In addition there is no distinct peak in mobility within the aforementioned interval. Similar to measured results, modelled Shields number decreases exponentially, but settles at a significantly higher ϑ = 0.008 – 0.01 at x = 15.

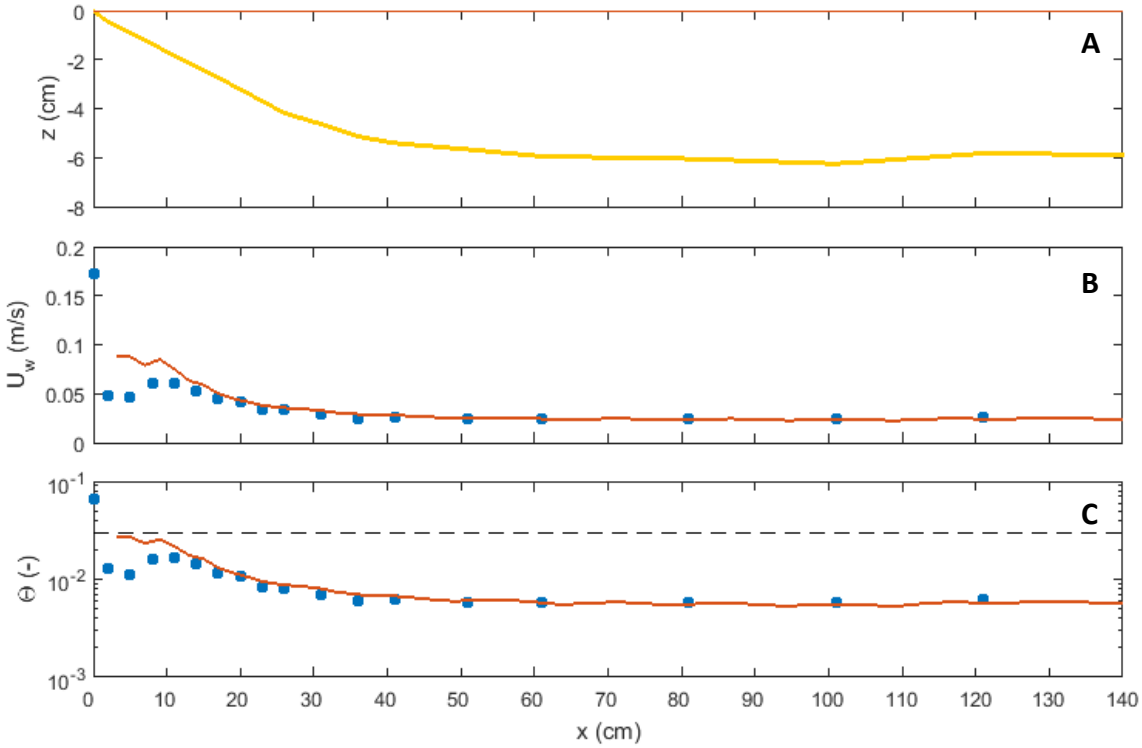

Figure 23. Experiment 1 (1:10 slope straight coast, 2 Hz waves) bottom profile (A); Maximum near-bed orbital velocity (B); and Shields number (C)

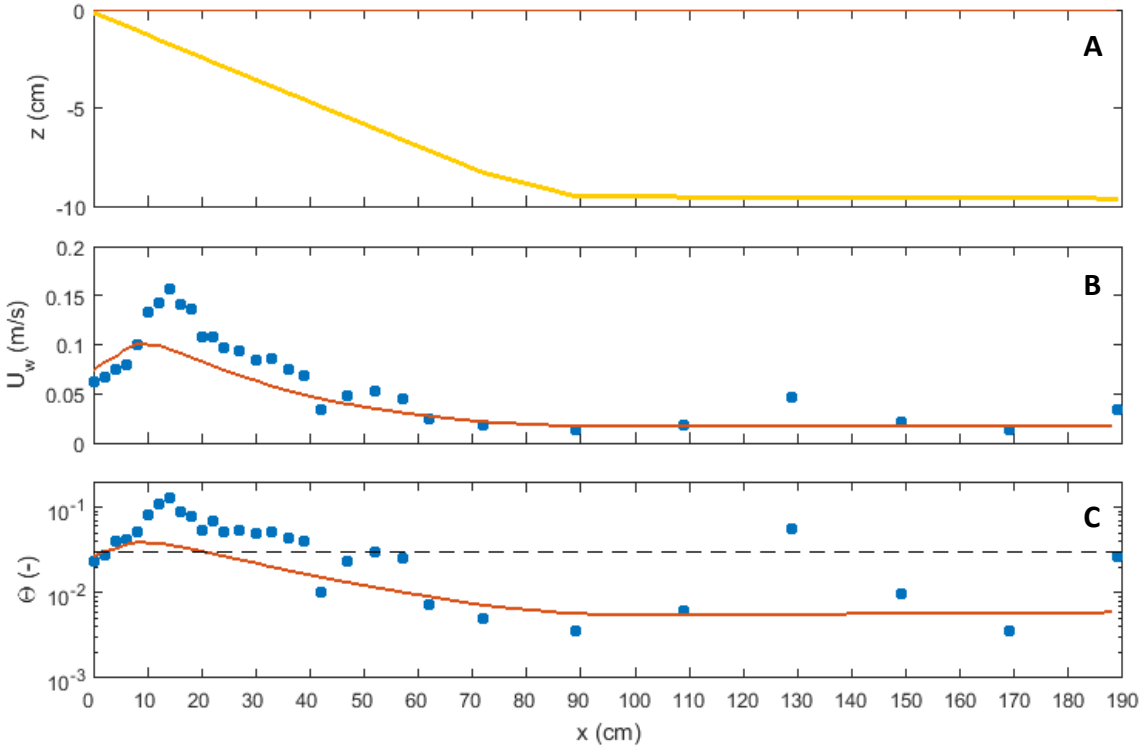

Figure 24. Experiment 2 (1:10 slope straight coast, 2.5 Hz waves) bottom profile (A); Maximum near-bed orbital velocity (B); and Shields number (C). Note different vertical scale in C.

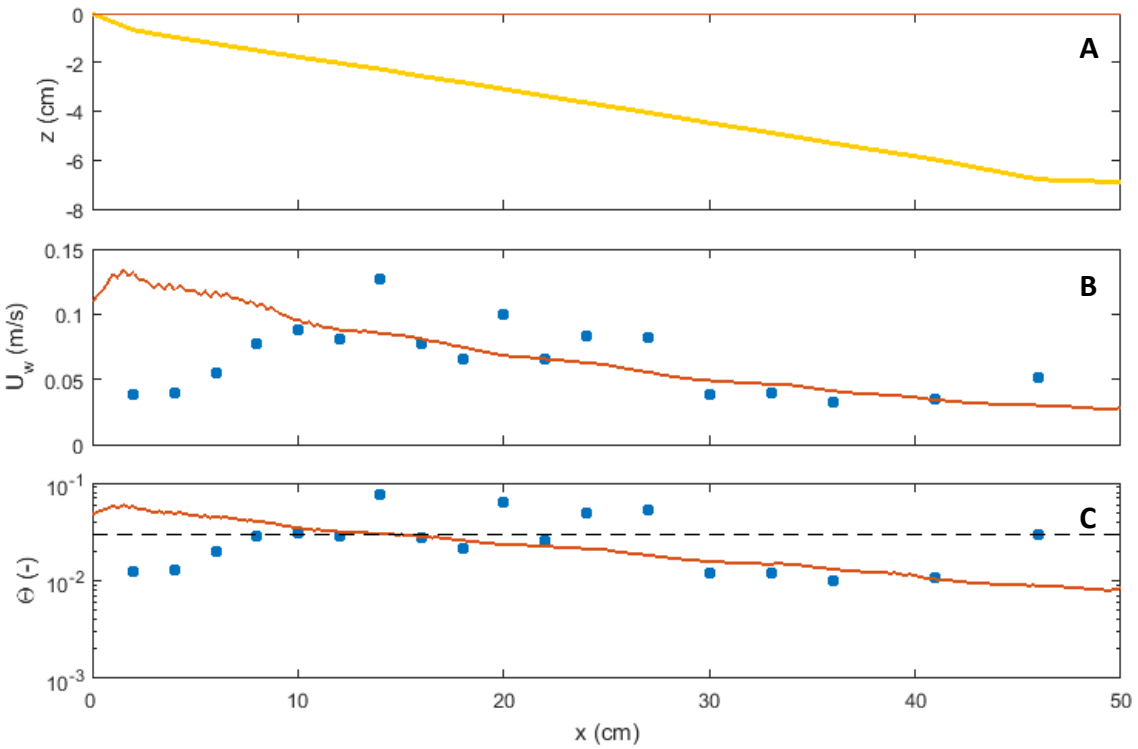

Figure 25. Experiment 3 (1:5 slope straight coast, 2.5 Hz waves) bottom profile (A); Maximum near-bed orbital velocity (B); and Shields number (C)

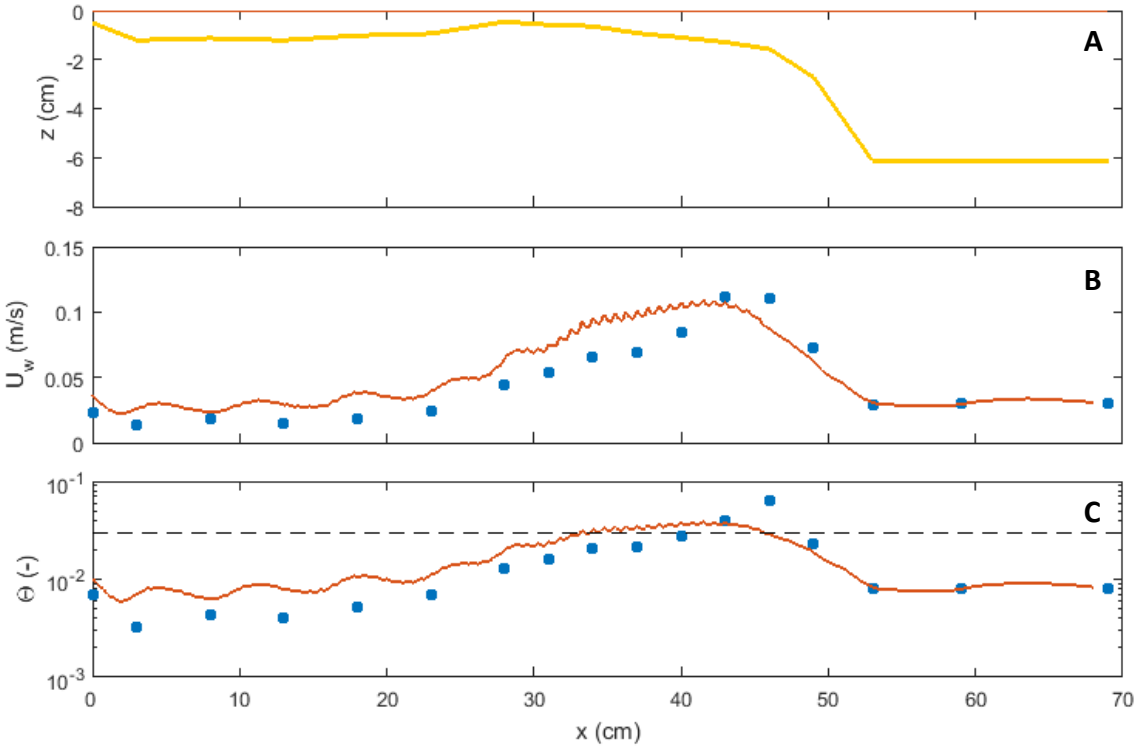

Figure 26. Experiment 4 (simplified delta, 2.25 Hz waves) bottom profile (A); Maximum near-bed orbital velocity (B); and Shields number (C).

5. Prototype results

Prototype modelling was done for the experimental ebb-delta, which was scaled up 500 times, resulting in a 250 m long ebb delta (i.e. the distance between terminal lobe and estuary mouth). Prototype model results are given for a range of distortions (n_l/n_h) between 1 (undistorted) and 5 (significant distortion) (Table 3). Distortions between 1 and 2 are termed 'low distortion'; distortions between 2 and 3 are referred to as 'medium distortion'; and distortions between 3 and 5 are henceforth called 'high distortion'.

Table 3. Overview of the effect of different distortion factors on geometry and wave parameters. Input wave is based on experiment 4 with a 0.009 m high wave and a period of 0.44 s. Horizontal length scale ratio n_l = 500.

Distortion:	n_h/n_l **=1**	n_h/n_l **= 2**	n_h/n_l **= 3**	n_h/n_l **= 4**	n_h/n_l **= 5**
Vertical length scales n_h, n_H	500	250	167	125	100
$H_{m.0}$**(m)**	4.5	2.25	1.5	1.13	0.9
T **(s)**	9.9	14.0	17.2	19.9	22.2
Maximum delta front steepness	1:1.17	1:2.34	1:3.51	1:4.68	1:5.85

5.1. Wave dimensions

Mean wave height depends on the distortion factor that is assumed (Figure 9), thereby making direct comparison of models with a different distortion factor difficult. Hence, the relative mean wave height was considered instead, which is wave height normalized by mean offshore wave height. From the results (Figure 27) it appears that the onset of breaking, i.e. where wave height declines, occurs at the same relative position as in the Metronome scale model. For higher distortion factors the point where waves begin to break is slightly more seaward. Also the gradient of wave height (H_m/dx) is larger at higher distortions, resulting in a slightly better similitude of highly distorted

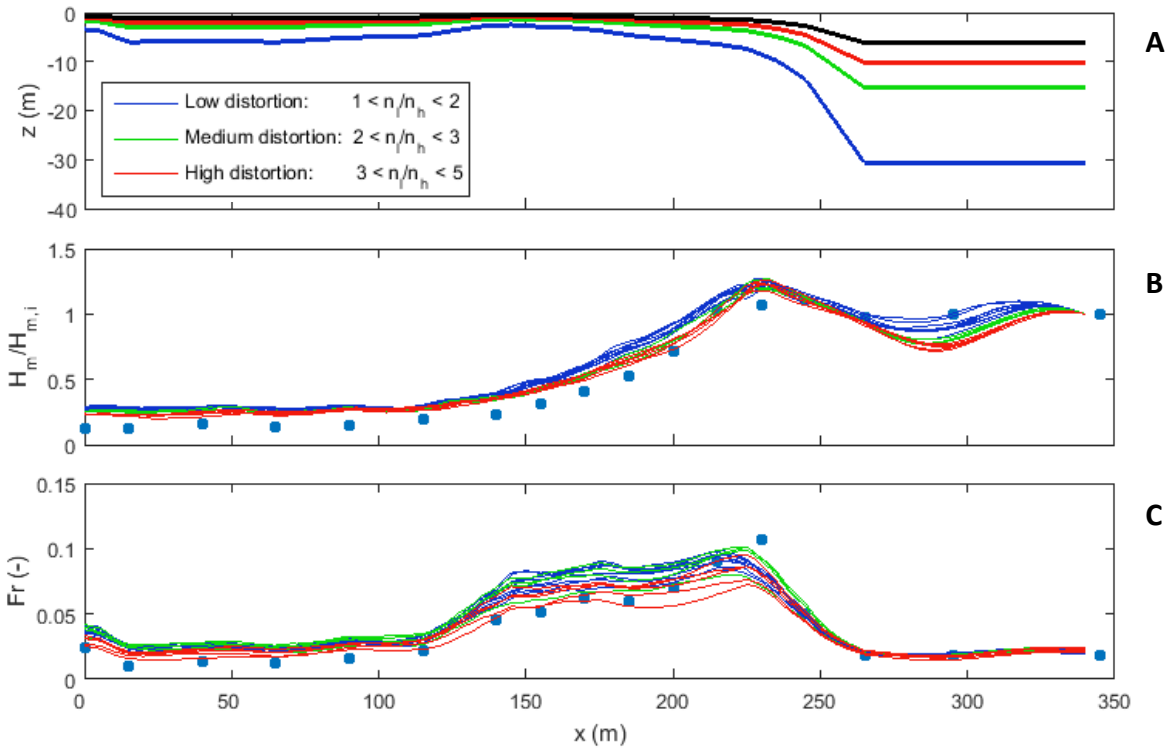

Figure 27. (A) Prototype bottom profiles for n_l/n_h = 1 (blue), n_l/n_h = 2 (green), n_l/n_h = 3 (red) and n_l/n_h = 5 (black). (B) Cross-shore development of relative mean wave height. Higher distortion yields a result that is closer to measured development (filled blue circles). (C) Development of Froude number, note perfect similitude at the seaward boundary. Higher distortion yields better Froude similitude along the coastal profile.

prototypes with measured results. In addition, relative wave height on the ebb delta behind the terminal lobe is lower and close to Metronome results at higher distortions. The surf zone similarity parameter is about 4.2, suggesting surging breakers and n_ξ remains 1. Froude number is in similitude for all prototype models close to the seaward boundary, since Froude-scaled waves are put in to the model at this boundary. As waves move onto the ebb delta, the Froude numbers of the prototype models diverge. Overall, Froude similitude in the zone where waves are affected by the bottom (from x = 250 to the coast at x = 0) is best maintained at high distortions.

5.2. Wave shape

Wave shape in general shows much clearer differences between prototype models (Figure 28). Wave skewness is slightly positive and shows no real development up till x = 150. After this point, where waves have already lost most of their initial height and propagate further over the shallow ebb delta, skewness becomes positive up to Sk = 1 for low distortion prototypes. At medium distortions, skewness varies around Sk = 0, which is closer to measured results. At high distortion factors, Sk < 1 for the area between x = 0 and x = 150. Asymmetry of waves over the ebb delta terminal lobe in the prototype models is much larger than that in the Metronome with As reaching

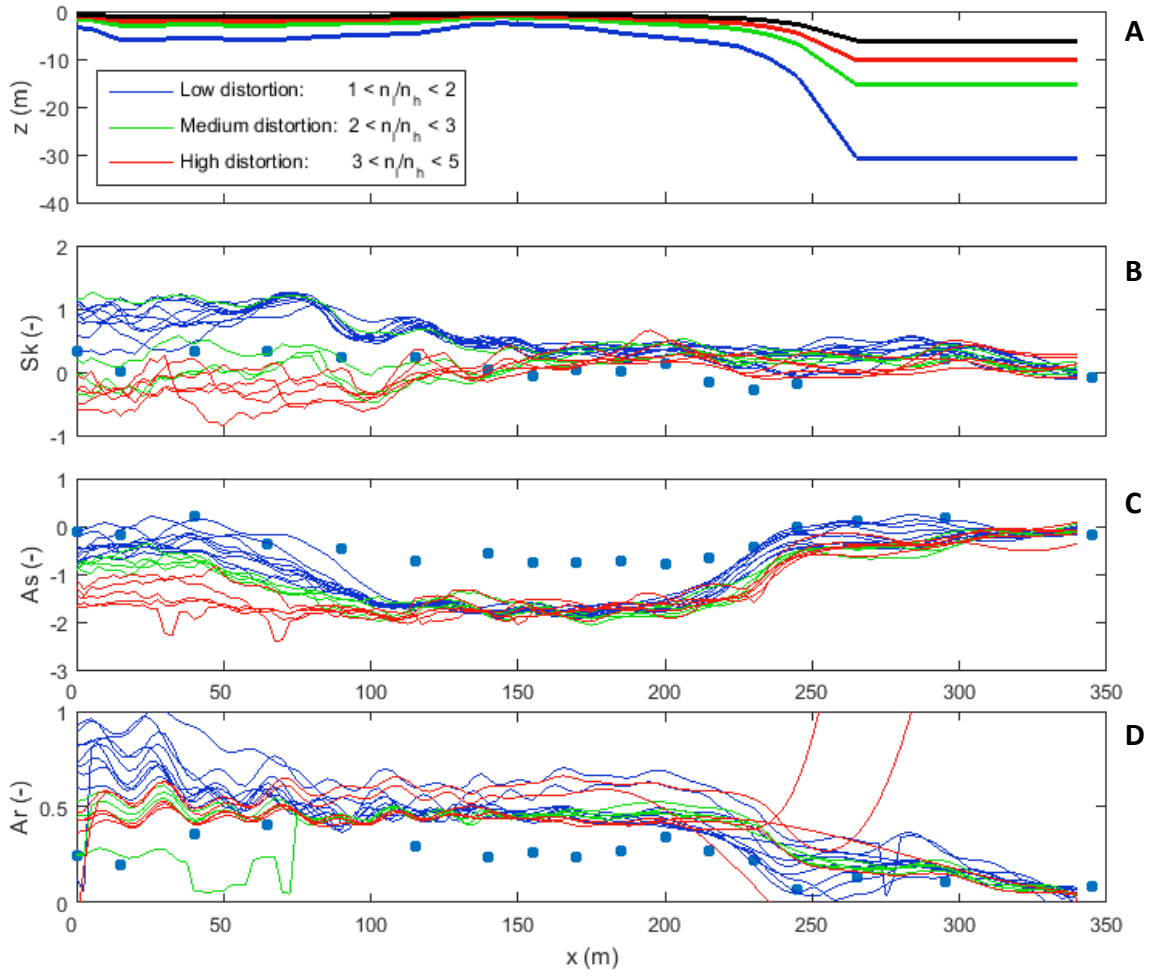

Figure 28. (A) Prototype bottom profiles for n_l/n_h = 1 (blue), n_l/n_h = 2 (green), n_l/n_h = 3 (red) and n_l/n_h = 5 (black). (B) Cross-shore development of wave Skewness. Less distorted models yield positive skewness (C) Development of wave asymmetry, Waves become asymmetric sooner at higher distortions. Maximum asymmetry is equal. Waves remain more asymmetric behind terminal lobe for distorted models. Overal waves become much more asymmetric at prototype scale (D) Total non-linearity. *Ar* is generally higher than measured results, especially in less distorted models.

up to -2. Development of asymmetry begins at around x = 250, at the same relative position where asymmetry of waves started to develop in the Metronome. Over the ebb delta between x = 250 and x = 100 there are no major differences between prototype models. After x = 100, modelled waves in low distortion models become less asymmetric towards the coast similar to measured results. High distortion models on the other hand have asymmetric waves up to the coast. Overall, waves of the prototype scale become highly non-linear when compared to results from the Metronome scale experiment (Figure 28D). In comparison to nature, the development of skewness up to Sk = 1 and asymmetry of up to As = -2 is significantly (more than one standard deviation) above average on the basis of the data collected by Ruessink et al. (2012).

5.3. Sediment mobility

Maximum near-bed orbital velocity for undistorted and low distortion models is 20-25 times higher than in the Metronome and about 15 times higher for heavily distorted models. In other words: maximum near-bed orbital velocity decreases with increasing model distortion (Figure 29). This trend also translates to the Shields number, which is 30 times higher in the undistorted prototype model and 10 times higher if distortion is assumed to be 5. The size of the waves (e.g. 4.5 m high with a period of 10 s) in combination with mobility all along the profile suggests that the waves are rough storm waves. However, based on the observed morphological development of on-shore migration of bars, it appears that relatively large waves effectively behave as calm weather waves in the Metronome. The larger shear stresses are expected as sediment size was not scaled in this example. Hence the much larger flow velocities at prototype scale cause a proportional increase of shear stresses in the model.

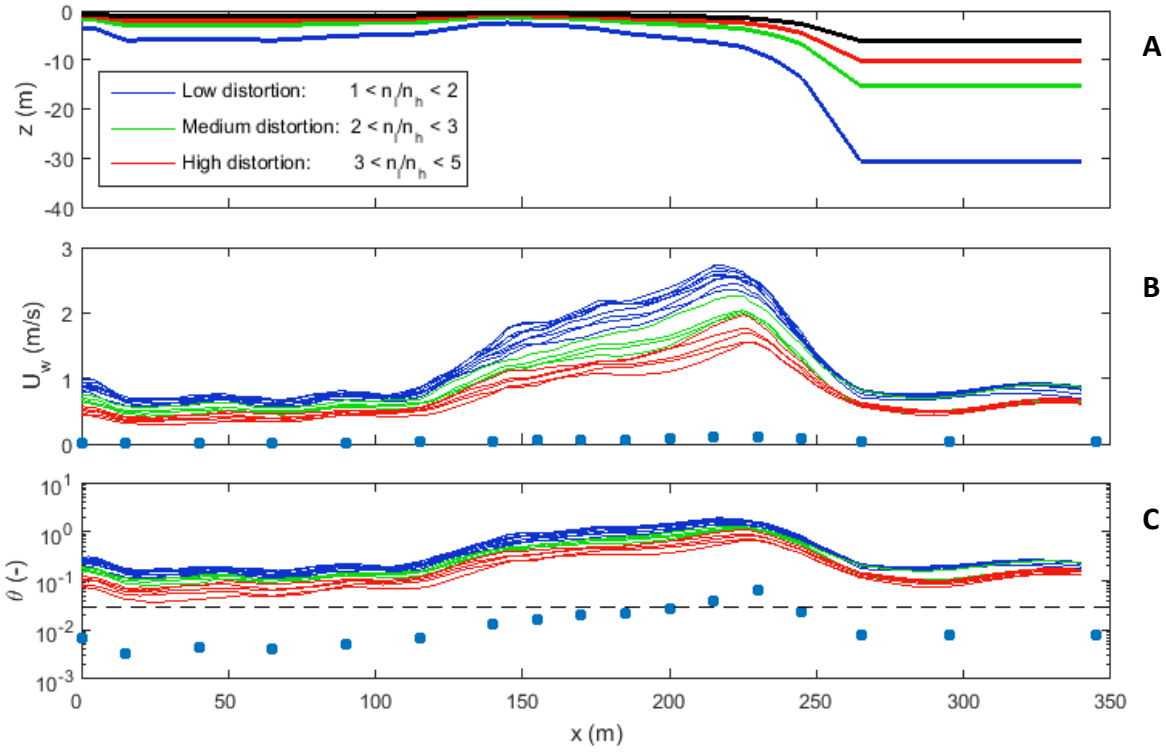

Figure 29. (A) Prototype bottom profiles for n_l/n_h = 1 (blue), n_l/n_h = 2 (green), n_l/n_h = 3 (red) and n_l/n_h = 5 (black). (B) Cross-shore development of maximum near-bed orbital velocity. Higher distortion yields a result that is closer to measured development. (C) Development of Shields number. In the absence of D_{50} scaling, Shields number becomes much higher in the prototypes, especially for undistorted and weakly distorted models.

In order to find the situation that we are actually modelling in the Metronome, a situation for which bed mobility of the prototype situation is in similitude with the Metronome model must be found. The latter can to some extent be done by varying model distortion (e.g. higher distortion lowers shear stresses, Figure 29) and sediment size (e.g. larger grain size reduces Shields number at given near-bed flow velocities. Results are shown in Figure 30. The mobility, represented by the recorded Shields number minus the critical Shields number, is 0 at the initiation of motion and higher than 0 for mobile beds. Best fits were derived by finding y in $n_{D50} = n_h^y$ that yields the smallest squared error between modelled and measured Shields number. Best fit functions (blue lines in Figure 30) show that less D_{50} scaling is required at higher distortions. This logically follows from the observation that increasing distortion alone causes Shields numbers in the prototype to become smaller. Without any assumed distortion between Metronome and prototype, the best fit for n_{D50} is given by $n_{d50} = n_h^{0.81}$, which gives a prototype median grain size of 9.2 cm. At the highest tested distortion of 5, $n_{D50} = n_h^{0.62}$ such that the median grain size is 1 cm. The aforementioned relation is close the empirical relation $n_{D50} = n_h^{0.55}$ proposed by Noda (1972). Furthermore, the position of peak mobility matches measured results better at higher distortions. The fitted situations proposed in (Figure 30) can be regarded as a 'literal translation' of the Metronome as a 1:500 scale model, thus we effectively reverse-engineered the natural, perfectly Froude-scaled situations on which the Metronome is based. For example: if no distortion is assumed, offshore waves are 4.5 m high, have a period of 10 s and propagate over a bed of cobbles with D_{50} = 9.2 cm. At a distortion of 5, offshore waves are 0.9 m high, have a period of 22 s and propagate over a medium gravel bed with D_{50} = 1 cm.

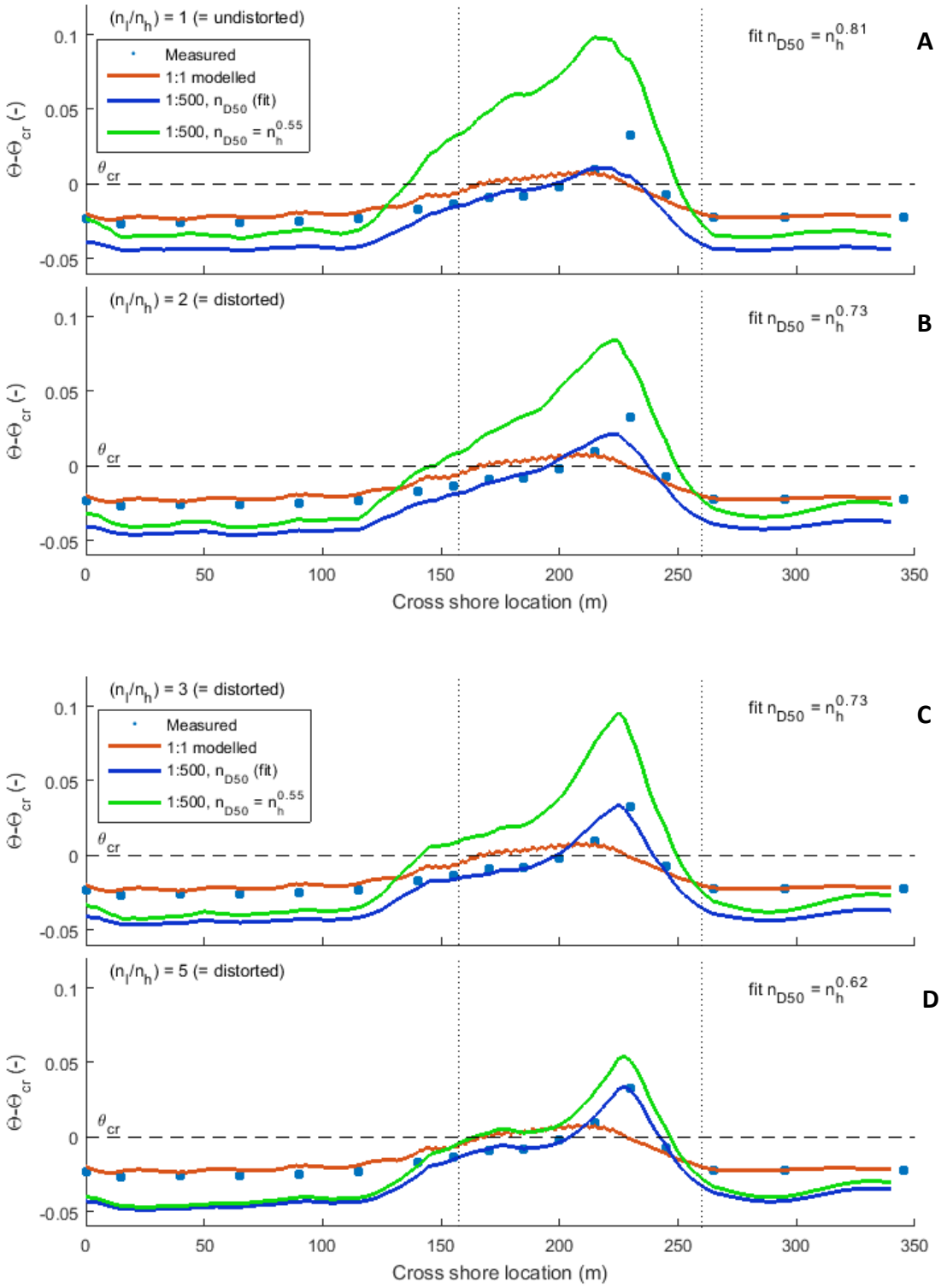

Figure 30. Development of ϑ-ϑ_{cr} over experimental ebb delta for n_l/n_h = 1 (A), n_l/n_h = 2 (B), n_l/n_h = 3 (C) and n_l/n_h = 5 (D). The power y in $n_{D50} = n_h^y$ that yields the best fit (blue line) of modelled ϑ-ϑ_{cr} to measured ϑ-ϑ_{cr} is given in the upper right corner. Green line represents $n_{D50} = n_h^{0.55}$ found by Noda (1972). Vertical bars indicate interval used for fitting $n_{D50} = n_h^y$. The empirical fits become progressively better with increasing distortion. For n_l/n_h = 5 and $n_{D50} = n_h^{0.62}$ model results almost perfectly match measured results.

The dependence of the best fit power y in $n_{D50} = n_h^y$ on the distortion ratio as well as the corresponding D_{50} scale ratio is given in Figure 31. Since increasing distortion causes prototype mobility to decrease, the required D_{50} scale ratio becomes smaller. Response of the required D_{50} scale ratio for mobility similitude is especially strong between distortions of 1 and 2. The linear decrease of maximum near-bed orbital velocity at increasing distortion ratios (Figure 31A) causes the relation between best fit n_{D50} and distortion ratio to become inversely exponential as $\vartheta \sim U_w^2$ (Figure 31B). The same holds for the relation between peak mobility and distortion (Figure 33). The mobile zone width was used as another indication of the effect of D_{50} scaling (Figure 32). If the gradient $d\vartheta/dx$ is low, the rate of decrease of mobile zone width dW_m/dn_{D50} is expected to be large. For our experimental delta specifically, where for $n_{D50} = 1$ all locations along the profile have a mobile bed, it means that at lower D_{50} scale ratios, the mobile zone width decreases rapidly as the areas over the delta and in the offshore zone with a low $d\vartheta/dx$ are to first areas to become immobile. At the point where Shields number changes rapidly (high $d\vartheta/dx$, between x = 125 and x = 275, a 150 m wide interval) mobile zone width decreases rapidly as n_{D50} is further increased. This point is visible just below $W_m = 150$ in as a sudden 'bend' going from high dW_m/dn_{D50} to a lower rate in Figure 32.

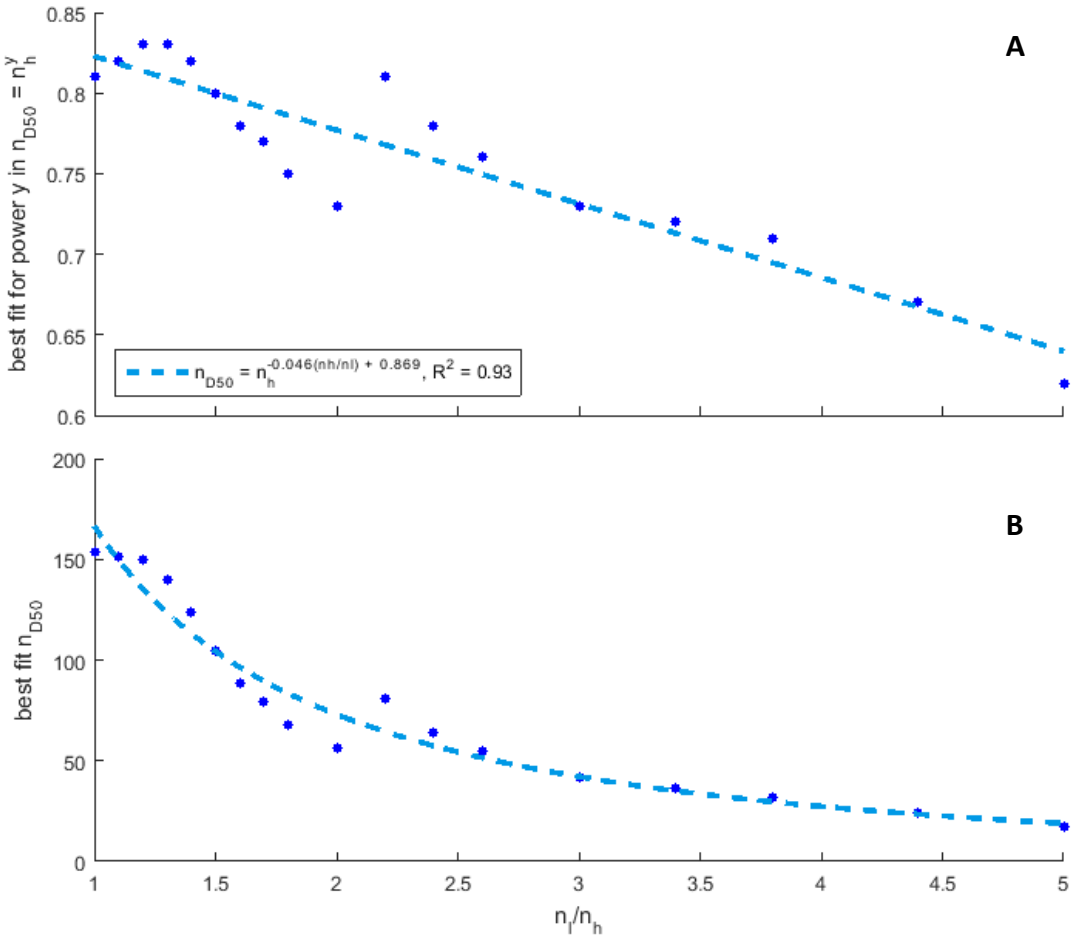

Figure 31. (A) Results of empirical fits of $n_{D50} = n_h^y$ for various distortion factors (i.e. the blue lines in Figure 30). (B) corresponding D_{50} scale ratios. Result shows that power y becomes smaller for increasing distortions i.e. the required sediment size to maintain mobility similitude is smaller if we regard the Metronome model as a distorted representation of reality. E.g. If we want to maintain mobility similitude we need to make grains 150 times larger if we scale up the Metronome model without distortion, but only 17 times larger if we assume a distortion of 5.

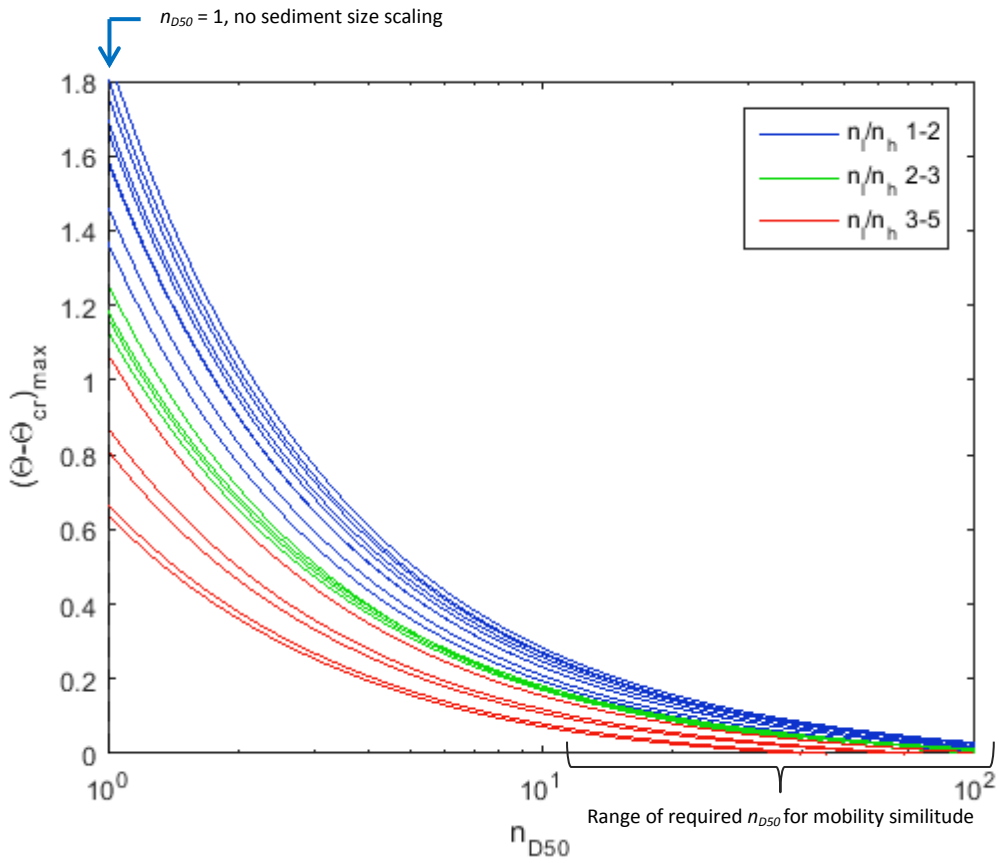

Figure 33. Peak mobility, represented as $(\vartheta-\vartheta_{cr})_{max}$. Results show that also for peak mobility, increasing distortion leads to decreasing mobility. Most notably, mobility is very sensitive to sediment size scaling close to n_{D50} = 1. E.g. peak mobility is reduced by about 80% between n_{D50} = 1 and n_{D50} = 10. Between n_{D50} = 10 and n_{D50} = 100 peak mobility declines far less.

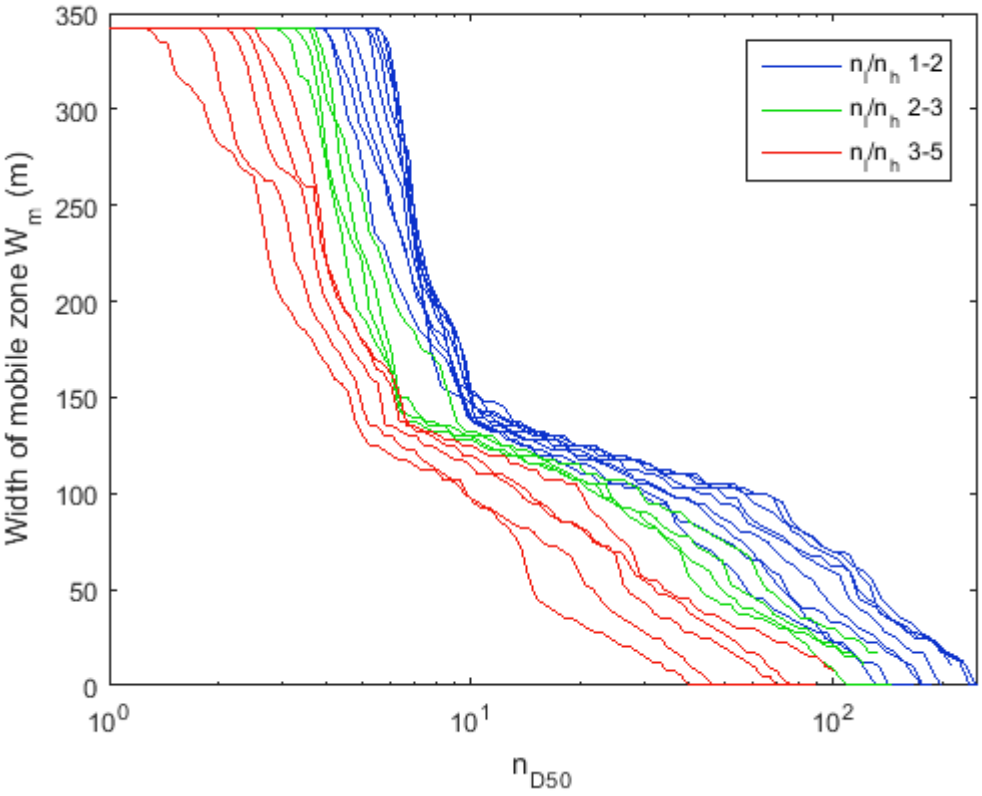

Figure 32. Mobile zone width, i.e. the length along the profile where $\vartheta-\vartheta_{cr} > 0$. Mobile zone width based on measurements indicated by the horizontal line at W_m = 40 Results show that for mobile zone width, higher distortion models require far less D_{50} scaling to accomplish similitude.

6. Discussion

In this research project, simplified coastal profiles were tested in the Metronome tidal facility. Our experimental ebb-delta was made 500 times larger in a model, which allowed us to investigate scale effects on wave-induced mobility. Waves were scaled up abiding strictly by the rules of (distorted) Froude scaling to maintain hydrodynamic similitude. Ultimately, the best models are those that remain undistorted and are as close as possible to the prototype scale (e.g. nature) (Hughes, 1993; Van Rijn *et al.*, 2011). While the latter makes the Metronome physical model far from ideal for wave experiments, we found numerous usable trends and relations with regards to wave dynamics, wave geometry and wave-induced sediment mobility that will be discussed in this chapter.

6.1. A simple scale comparison

Thus far, we only compared Metronome experiments to a SWASH modelled prototype. Since physical models are designed to simulate nature, it is useful to make a simple assessment of scales that shows how our experiment fits in reality in terms of wave climate and water depth over the ebb delta (Figure 34).

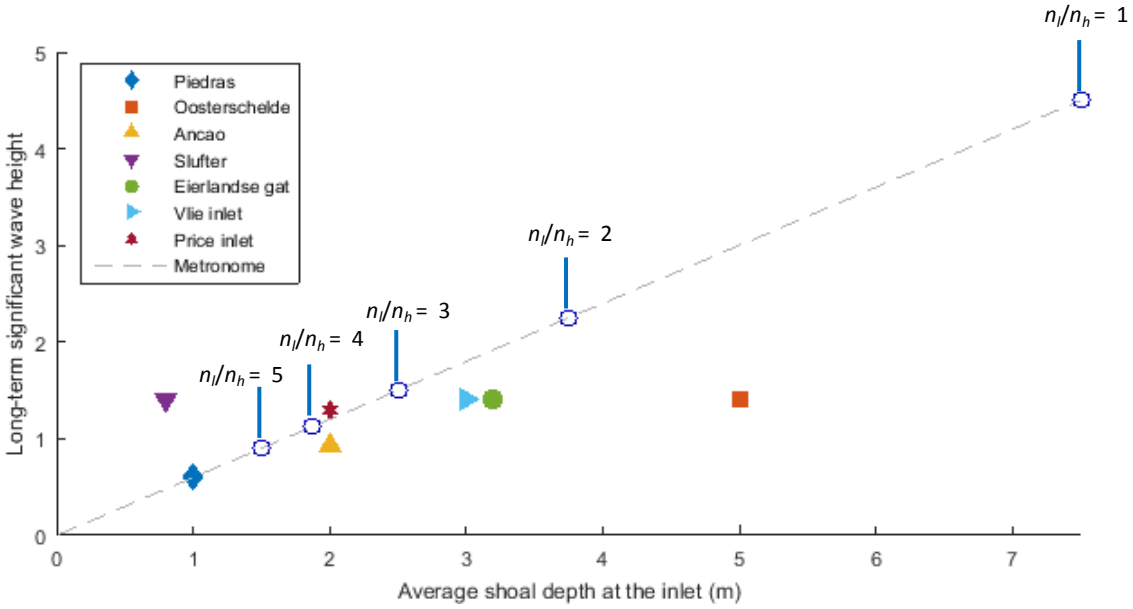

Figure 34. Comparison of wave climate and average inlet/ebb delta terminal lobe depth. Grey line represents the prototype model of the experimental ebb delta with various distortion factors indicated. Undistorted prototype has a wave height of 4.5 m at a depth of 7.5 m and falls well outside the range of natural situations displayed here. Distortions of 3-5 agree better with the examples from nature in terms of absolute wave height and terminal lobe depth. Field data: Piedras estuary mouth (Morales et al., 2001); Oosterschelde (Eelkema et al., 2013); Ancão estuary, Slufter, Eierlandse gat, Vlie inlet (Bertin et al., 2009; Kleinhans et al., 2015; Ridderinkhof et al., 2016); Price inlet (Fitzgerald, 1984).

Assuming the Metronome is an undistorted representation of reality at 1:500 scale, waves in the Metronome are comparatively large and water is relatively deep. Thus, on the basis of Froude similitude and an assumed 1:500 length scale, the ebb delta's that are formed in the Metronome are faced with extremely rough waves when considering mean wave height alone. At higher distortions between 3 and 5, offshore significant wave height and water depth above the ebb-delta terminal lobe correspond better to the observed values in the natural systems displayed in Figure 34. The latter supports the assumption that the Metronome scale model is a distorted representation of reality. The ratio between offshore significant wave height and average depth over the terminal lobe is constant across distortion ratios and is comparable to those of the Piedras estuary mouth, the Price inlet and the Ancão estuary.

6.2. Wave dynamics

We were able to keep waves in almost perfect Froude similitude throughout the entire range of tested distortion ratios. From comparison of measured and modelled wave height loss at various scales and geometric distortions we can confirm previous findings of Le Mehaute (1976). He argued that wave energy dissipation in the near-shore is independent of the fine details of the flow, but is intrinsically accounted for by the momentum balance, which is integrated in SWASH (Smit *et al*., 2013). Although total energy loss after breaking is correctly modelled at 1:1 scale, the position where waves begin to break had to be calibrated. In general, we found that the longest waves in the Metronome (experiment 1 and 4, 2 and 2.25 Hz wave input, respectively) required significantly lower breaking parameters α and β. In other words: the onset of breaking had to be initiated at gentler wave fronts in order to follow the decline of measured wave height correctly. At a higher wave frequency of 2.5 Hz, α and β were close to the calibrated (SWASH default) values used to model waves at natural scale. It appears that adjustment of the breaking parameters is required for waves with an offshore steepness of less than $H_0/L_0 = 0.05$. However, with only four experiments for which calibration parameters were defined, we cannot draw solid conclusions without doing multivariate analysis on a larger dataset. At scales larger than that of the Metronome, both the onset of breaking and total energy loss will be in similitude across scales, based on findings of Stive (1985). The errors that persisted in energy dissipation despite calibration efforts may seem small at first glance, but are magnified in mobility calculations as $\vartheta \sim U_w^2$. Furthermore, due to the rapid loss of wave energy, only a small offset in the position where breaking commences may lead to large differences between measured and modelled wave height in the surf zone. This led to several occasions where we predicted no sediment mobility based on model runs, whereas based on measurements and visual observations, the bed was mobile. Thus, care should be taken in measuring and modelling waves in the surf zone as errors in wave height prediction may lead to unreliable mobility calculations.

The shoreface in the Metronome is usually very steep at roughly 35° in wave only situations and slightly gentler if tides are included. The steep gradients make the coast highly reflective causing bore-like breaking of waves (Battjes, 1975). In order to simulate more realistic spilling or plunging type breakers, the bottom profile should be much gentler. E.g. for the waves in our simplified delta experiment the coastal gradient should be reduced to 0.1 or 0.05 to get plunging and spilling breakers, respectively. Alternatively, waves should be made steeper such that H/L in Eq. (2.9) becomes higher, thereby reducing the surfzone similarity parameter for a given beach gradient. In a physical model where only bed-load transport is present, care should be taken when suspended transport is considered in a prototype model, since suspended transport depends on breaker type (Kana, 1979; Nielsen, 1984; Beach & Sternberg, 1996).

Wave non-linearity in physical wave models is generated by (1) the wave generator and (2) by wave-wave interaction in the near-shore. In our case non-linearity was recorded close to the wave generator by the presence of a second-order wave signal in the frequency spectrum. Non-linearity made waves close to the generator slightly skewed, rather than asymmetric. Wave generator related non-linearities were not further considered as the second-order wave almost completely dampened out before reaching the near-shore zone. Application of suppression techniques to reduce second order waves as described in section 2.4 thus appear to be obsolete as long as there is enough distance over deep water for waves to become fully linear. This result also suggests that water in our offshore zone can be considered 'deep' despite the fact that water depth < 0.5L in some cases.

Non-linearity in the near-shore zone was characterized by the distinct development of wave asymmetry. Parameterization of skewness and asymmetry through the Ursell number suggests that Metronome waves do not fully develop skewness when compared to the field data presented in Ruessink et al. (2012) and other parameterizations in Figure 22. Asymmetry on the other hand fully develops up to the point of wave breaking as expected based on the aforementioned field data and parameterizations. However, asymmetry begins to develop its trend at Ursell numbers that are 10 times lower compared to trends found by Doering and Bowen (1995); Kuriyama (2009); Ruessink et al. (2012); and Rocha et al. (2017). Ruessink et al. (2012) discuss that their parameterization, which is

based on directionally spread waves from field studies, will likely underestimate skewness for laboratory waves since wave-wave interaction is stronger for uni-directional waves (Janssen, 2006). This contradicts our findings of largely undeveloped wave skewness in the Metronome and indicates that the lack of directional spreading of Metronome waves does not explain the observed discrepancy with waves in nature.

Waves in the Metronome are relatively long and approach the infragravity wave regime at higher distortion ratios (e.g. H = 0.9, T = 22 at n_l/n_h = 5). The relatively long waves may explain the reduced development of wave skewness as interactions between low frequency waves tend to reduce skewness and asymmetry at the surface (Elgar and Guza, 1985). Furthermore, De Bakker et al. (2015) found, based on infragravity wave experiments part of the GLOBEX project, that infragravity-infragravity interactions induce higher harmonics that cause waves to become asymmetric rather than skewed. Although development of non-linear interactions of low frequency waves may explain observed trends if we assume high distortions, it does not explain the behavior of waves if we assume no distortion. If no distortion is assumed, waves in e.g. our ebb-delta experiment fall within the sea/swell wave regime if scaled up to prototype conditions. Hence, in our case the absence of skewness cannot be explained by wave regime alone.

The development of sea/swell wave skewness and asymmetry is also related to offshore wave steepness and beach slope, with skewness being affected the most (Rocha et al., 2017). In small-scale wave experiments such as in the Metronome, the beach slope and offshore wave steepness is often much larger than in nature. For example: on the self-formed ebb-deltas in the Metronome, the seaward facing slope of the delta's terminal lobe can become as steep as the angle of repose of wet sand, while offshore waves were up to three times steeper than typical sea waves with a period of 8 s and a significant wave height of 1.5 m. Steeper offshore waves result in a reduced development of total non-linearity because they begin to break in deeper waters (Dibajnia et al., 2001; Rocha et al., 2017). Steep beach slopes also limit the development of non-linearity, especially due to the decreased contribution of skewness. Over a gentle slope, skewness has more time to develop than asymmetry (Rocha et al., 2017). Conversely, for steeper slopes asymmetry has more time to develop relative to skewness, resulting to a greater contribution of asymmetry to the total non-linearity. Although beach gradient and offshore wave steepness also varied between our experiments, there was no significant difference in skewness/asymmetry development. However, this could be explained by the large variation in our dataset. We conclude that the effects of offshore wave steepness and beach gradient best explain our findings of an overall reduced development of total non-linearity and a larger contribution of asymmetry to the total non-linearity. There is no known explanation of the development of skewness and asymmetry at lower Ursell numbers. The latter is most likely caused by a scale effect of unknown origin and remains the subject of future research.

6.3. Sediment mobility and transport

In order to find conditions for mobility similitude we attempted to find the best D_{50} scale ratios across a range of distortions to fulfill this condition. As Metronome sediment size is similar to that in nature, we cannot satisfy similitude of flow characteristics through the Froude number while at the same time having mobility similitude, i.e. sediment size scaling is unavoidable in a Froude-scaled model. With modern modeling techniques available, allowing us to test a larger number of scenarios in a considerably smaller amount of time (compared to collecting field or experimental data), we have been able to expand Noda's (1972) empirical relation (Eq. 2.21 & 2.22) across a range of distortion ratios. The empirical relation between n_{D50} and distortion n_l/n_h based on our results is close to that of Noda (1972) (Figure 30D) at n_l/n_h = 5, but at lower distortions the required D_{50} scale ratio is considerably higher. The trends presented in Figure 31 are expected to continue for n_l/n_h > 5. The scaling laws derived by Ito and Tsuchiya (1984, 1986, 1988) and Ito et al. (1995) (Eq. 2.23 & 2.24) lie far from the relations derived by Noda (1972) and those found in this paper.

The direction of sediment transport in the near-shore zone is mainly determined by wave skewness and asymmetry resulting from non-linear wave-wave interactions (Ribberink et al., 1995; Nielsen, 2006; Ruessink et al., 2011) in combination with phase-lag effects (Ruessink et al., 2009;

Silva et al., 2011) for suspended load transport. Since sediment transport in most small-scale experiments is bedload-dominated the latter effect is not immediately relevant. The limited development of wave skewness implies that the Metronome is missing an important contributor to on-shore directed sediment transport. Thus, at a given sediment mobility, more sediment would be expected to transport towards the shore in reality. In addition, the absence of bound infragravity waves takes away another component that can suspend sediment and cause onshore or offshore directed sediment transport, depending on location (Beach & Sternberg, 1988; Aagaard & Greenwood, 2008). Lastly, in nature the presence of bedforms may also contribute to the direction of sediment transport (Ribberink and Al-salem, 1994), which was not the case in the Metronome as no bedforms were formed by waves. In conclusion, small scale wave models model is missing a number of important transport mechanisms (i.e. the absence of wave skewness, bound infragravity waves, phase lag effects, suspended transport and bedforms) that are important for modelling bed level change. As such, these mechanisms must be accounted for if a wave model is scaled up and coupled to a sediment transport model. Furthermore, due to the lack of wave skewness, on-shore transport rates at the ebb delta's terminal lobe are likely to be larger in nature.

In this research the D_{50} scaling relation is based on the requirement of mobility similitude ($n(\vartheta\text{-}\vartheta_{cr})$ = 1), which is a modified version of the sediment transport similitude requirements of Kamphuis (1985). The D_{50} scaling laws from Noda (1972); Ito and Tsuchiya (1984, 1986, 1988) and Ito et al. (1995) were derived from equilibrium bed profiles, where a fully developed (equilibrium) bed profile in a model is compared to its prototype counterpart. Care should be taken when applying this method to small-scale models such as the Metronome, since using equilibrium bed profile similitude inadvertently takes into account other factors that are responsible for sediment transport, such as wave skewness, asymmetry and relative amount of bedload and suspended load. We argued that in small-scale models the development of skewness and asymmetry is mostly influenced by offshore wave steepness and beach gradient. Thus, in a small-scale experimental setup with reduced total non-linearity, almost no contribution of skewness and no suspended transport, the balance between on-shore and off-shore directed sediment transport rates will be more in favor of off-shore transport despite similitude of the Shields' number. Hence, deriving D_{50} scaling laws from equilibrium bed profiles in this case is very difficult as model and prototype equilibrium bed profiles will either be different or suggest inaccurate scaling requirements. For the equilibrium bed profile method to be accurate, a model should most importantly be undistorted and should ideally also have a similar contribution of bed load and suspended load to the total amount of sediment transport.

6.4. Recommendations and future work.

The comparison between physical and numerical model data in this research is purely based on scaling up to natural scale under the strict requirement of Froude similitude. Although this provides an insight into the behavior of very small scale waves compared to their Froude-scaled natural-scale counterparts, it does not provide an answer on whether the mobility over the experimental ebb-tidal corresponds to nature in the first place. A simple mobility computation based on wave conditions for the natural ebb deltas given in Figure 34 yields shields stresses at $z = 0.05L_0$ over the terminal lobe of ϑ = 0.1-0.4 for D_{50} = 0.0006 m. Mobility at $z = 0.05L_0$ over the Metronome ebb-tidal delta is far lower at ϑ = 0.03-0.06, thus the degree of sediment mobility should be made higher in the Metronome. This can be accomplished by either choosing a different type of sediment with a lower density or by generating higher waves (Figure 35).

Since the slopes on the ebb-delta are very steep in the scale experiment compared to nature, the Metronome scale model could be regarded as a distorted representation of reality. If distortion is applied such that the beach slope in the prototype attains a more realistic gradient, waves become long, low and thereby fit into the infragravity wave regime. From this point of view, waves in the Metronome should be made higher and steeper which will have two effects (1) sediment mobility is increased (Figure 35A) and (2) the surfzone similarity parameter is brought back to more realistic values. On the downside this may further reduce the development of non-linearity, leading to decreased on-shore transport rates.

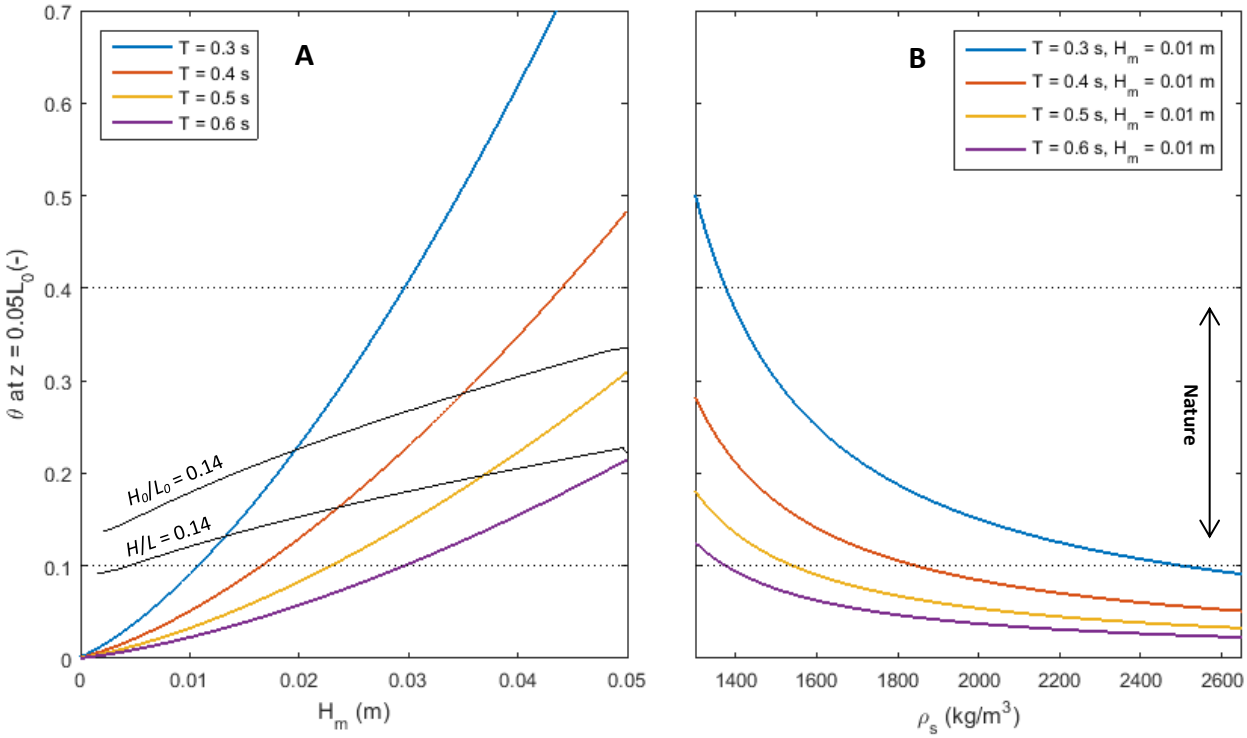

Figure 35. Effect of mean wave height (A) and sediment density (B) on the Shields mobility number at depth z = $0.05L_0$. Adjusting wave height is limited by the maximum steepness of waves. Above the line indicated as H/L = 0.14, waves will begin to break due to oversteepening, rather than depth-induced breaking. i.e. this line indicates the maximum mobility that can be reached before energy dissipates. Above the line indicated as H_0/L_0 = 0.14, waves already break in the offshore zone due to oversteepening, which is further detailed in Figure 36B.

Steeper waves can be generated by either reducing wavelength or by increasing wave height, but this may result in unwanted scale effects if overdone. For the sampling conditions used in this research (Fs = 20 Hz; transducer distance = 15 cm; beam aperture = 8°) offshore waves should be longer than 0.1 cm (Figure 6). Additional problems arise if waves are shortened: surface tension and internal friction effects may become significant and oversteepening of waves may lead to wave breaking in deep water (white-capping). The contribution of surface tension to the wave dispersion relation, expressed by the fraction F_{st} (Eq. 2.21) increases rapidly for waves with L_0 < 0.1 m (Figure 36A). Although there is no agreed upon value for the critical Weber number, a critical range of between 10 and 120 is reported by Peakall et al., 1996 on the basis of small river experiments. The critical range implies that surface tension may affect flow and wave characteristics in a model, but to which extent, especially for small model waves, is yet to be identified. Weber numbers below 10 should at all cost be avoided, which for a 0.01 m wave height occurs for wavelengths of less than 0.07 meters (Figure 36A). The loss of wave height per meter (as a fraction of initial wave height) is also given in Figure 36A. Waves shorter than 0.1 meter may lose a significant amount of energy due to internal friction and are therefore unsuitable for use in experiments. Deep water waves begin to break at a steepness of H_0/L_0 = 0.14 (dashed line in Figure 36B) and by H_0/L_0 = 0.175, all waves have broken (Toffoli et al., 2010) (solid line in Figure 36B). For typical wavelengths in the Metronome of between 0.2 and 0.3 m, a wave height of 0.03 m or higher will lead to preliminary wave breaking in deep water. The wave steepness limit is also indicated in Figure 35 for both near-shore and off-shore waves. Using waves close to their limit steepness is not recommended because they break in deeper water, thus preventing skewed and asymmetric wave shapes from developing and thereby also limiting sediment transport as previously discussed. Furthermore, if a wave generator is set to generate waves at their limit steepness, they will likely break just after leaving the wave paddle because their slightly asymmetric shape causes the wave front to be too steep. In summary: to avoid scale effects (surface tension and internal friction) and preliminary wave breaking in small-scale wave

experiments, a minimum wavelength of L_0 = 0.1 m and keeping offshore wave steepness as low as possible (and never exceeding H_0/L_0 = 0.14) to avoid scale effects on wave non-linearity is recommended.

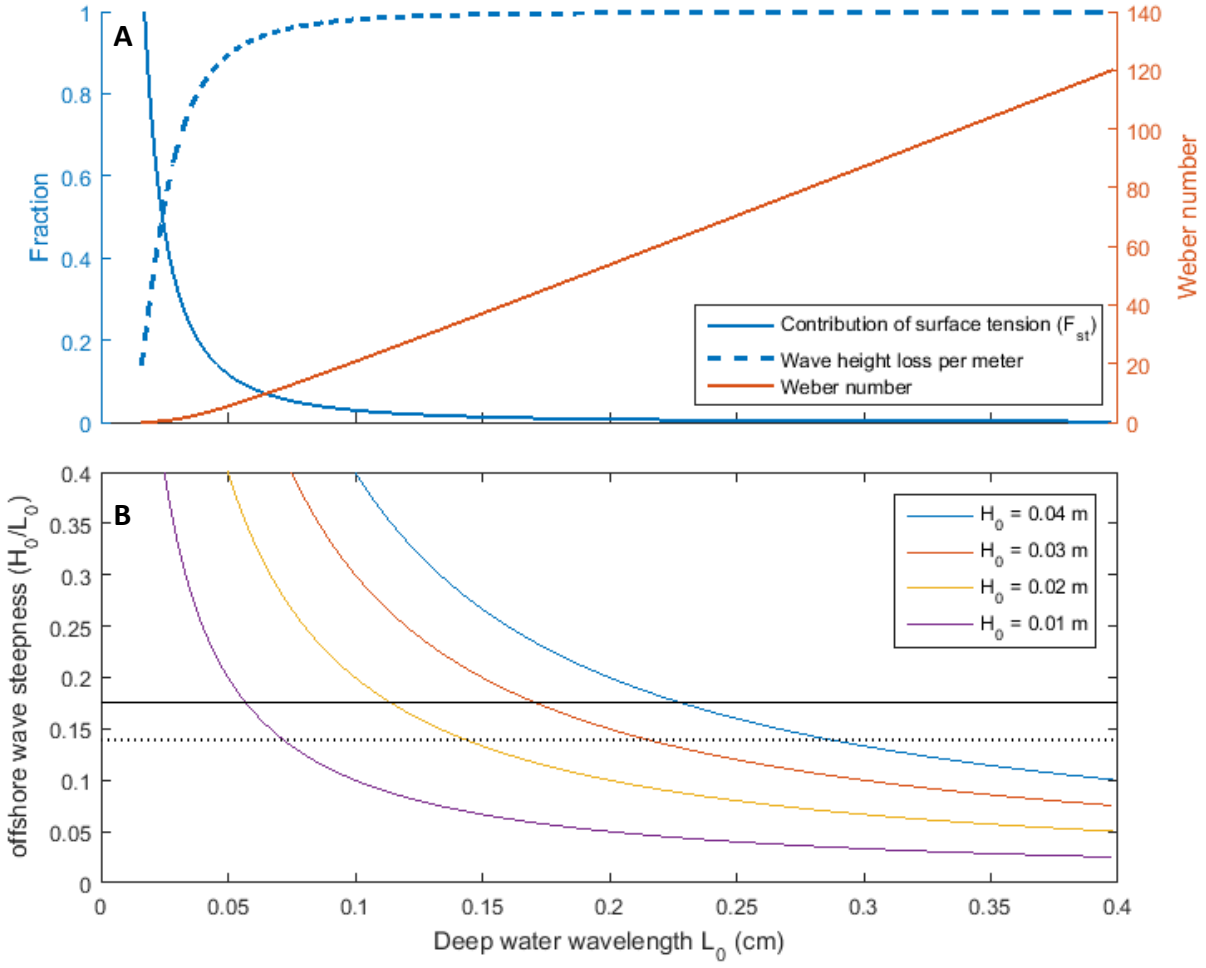

Figure 36. Effects of deep water wave length on scale effects and wave steepness. (A) scale effects: surface tension and internal friction become a significant factor for L_0 < 0.1 m. Internal friction here is shown as wave height loss per meter as a fraction of initial wave height. E.g. for L_0 = 0.05 m H = 0.9H_0 after 1 meter. (B) wave steepness H_0/L_0 is shown for four different offshore wave heights. Deep water wave breaking (white-capping) begins at a steepness of H_0/L_0 = 0.14, hence it is recommended to keep waves long enough to prevent this from happening.

Although we have attempted to quantify scale effects in great detail, it is often not required to strictly abide by scaling rules to recreate morphological patterns (Kleinhans et al., 2014). Thus, when it comes to scaling sediment size up to simulate prototype conditions in a model, it is most important to at least make sure that undistorted prototype sediment is not mobilized by waves in the offshore zone and behind the terminal lobe of the ebb-delta. Based on the current sediment and wave conditions in the Metronome, it requires median grain size scale ratios of 5 (distortion 5) to 10 (undistorted) to ensure prototype mobility is limited to the delta front.

7. Conclusions

We conducted four monochromatic, unidirectional wave experiments over simplified straight coast and delta bathymetries. We found that the on average 1 cm high waves are not significantly affected by surface tension effects or by bottom and/or sidewall friction in our 3 m wide basin, allowing us to use equations for gravity waves. Based on the Metronome wave experiments and 1:1 scale models in SWASH we found that:

- The SWASH wave model is able to accurately simulate waves at Metronome scale. However, small errors in wave energy dissipation may lead to large discrepancies in mobility and hence sediment transport models that could potentially be coupled to it.
- For small-scale models with relatively steep offshore waves and large beach gradients, the maximum total wave non-linearity is smaller and mainly translates to the development of wave asymmetry while skewness barely develops.
- In comparing small-scale wave models to nature, on-shore transport is likely to be underdeveloped due to the absence of on-shore transport under skewed waves.

The experimental ebb delta was scaled up 500 times using Froude scaling for a range of geometric distortions between 1 and 5. Froude number and wave energy dissipation were in similitude along the entire cross-shore profile, regardless of model distortion.

- Wave non-linearity appears to be stronger in the prototype: especially wave asymmetry is about twice as strong over the ebb-delta terminal lobe compared to the Metronome model.
- The required degree of D_{50} scaling for mobility similitude between prototype and model is a function of the amount of geometric distortion. In $D_{50} = n_h^y$ the power y is inversely proportional to geometric distortion. This is because maximum near-bed orbital velocity decreases proportionally to increasing distortion, which leads to an exponential decrease of mobility.
- Metronome waves should be made higher and steeper in order to achieve similar mobility as over natural ebb deltas. The recommended minimum deep water wavelength for small-scale waves in general is 0.1 m to avoid surface tension and internal friction effects. Furthermore, too steep waves have the disadvantage of (1) potential steepness-induced breaking rather than depth-induced breaking; and (2) reduced development of wave non-linearity.

References

Aagaard, T., & Greenwood, B. (2008). Infragravity wave contribution to surf zone sediment transport—The role of advection. *Marine Geology*, *251*(1), 1-14.

Abreu, T., Silva, P. A., Sancho, F., & Temperville, A. (2010). Analytical approximate wave form for asymmetric waves. *Coastal Engineering*, *57*(7), 656-667.

Baldock, T. E., Alsina, J. A., Caceres, I., Vicinanza, D., Contestabile, P., Power, H., & Sanchez-Arcilla, A. (2011). Large-scale experiments on beach profile evolution and surf and swash zone sediment transport induced by long waves, wave groups and random waves. *Coastal Engineering*, *58*(2), 214-227.

Battjes, J. A. (1975). Surf similarity. In *Coastal Engineering 1974* (pp. 466-480).

Beach, R. A., & Sternberg, R. W. (1988). Suspended sediment transport in the surf zone: response to cross-shore infragravity motion. *Marine Geology*, *80*(1), 61-79.

Beach, R. A., & Sternberg, R. W. (1996). Suspended-sediment transport in the surf zone: response to breaking waves. *Continental Shelf Research*, *16*(15), 1989-2003.

Bertin, X., Fortunato, A. B., & Oliveira, A. (2009). Morphodynamic modeling of the Ancão Inlet, south Portugal. *Journal of Coastal Research*, 10-14.

Brocchini, M., & Baldock, T. E. (2008). Recent advances in modeling swash zone dynamics: Influence of surf-swash interaction on nearshore hydrodynamics and morphodynamics. *Reviews of Geophysics*, *46*(3).

Daugaard, E. (1972). Generation of regular waves in the laboratory. *Institute of Hydrodynamics Engineering, Technical University of Denmark*.

De Bakker, A. T. M., Herbers, T. H. C., Smit, P. B., Tissier, M. F. S., & Ruessink, B. G. (2015). Nonlinear infragravity–wave interactions on a gently sloping laboratory beach. *Journal of Physical Oceanography*, *45*(2), 589-605.

De Swart, H. E., & Zimmerman, J. T. F. (2009). Morphodynamics of tidal inlet systems. *Annual review of fluid mechanics*, *41*, 203-229.

Dibajnia, M., Moriya, T., & Watanabe, A. (2001). A representative wave model for estimation of nearshore local transport rate. *Coastal Engineering Journal*, *43*(01), 1-38.

Doering, J. C., & Bowen, A. J. (1995). Parametrization of orbital velocity asymmetries of shoaling and breaking waves using bispectral analysis. *Coastal Engineering*, *26*(1), 15-33.

Eelkema, M. (2013). *Eastern Scheldt inlet morphodynamics* (Doctoral dissertation, TU Delft, Delft University of Technology).

Fedorov, A. V., & Melville, W. K. (1998). Nonlinear gravity-capillary waves with forcing and dissipation. *Journal of Fluid Mechanics*, *354*, 1-42.

Fenton, J. D., & McKee, W. D. (1990). On calculating the lengths of water waves. *Coastal Engineering*, *14*(6), 499-513.

Hansen, J. B., & Svendson, I. A. (1974). Laboratory generation of waves of constant form. *Coastal Engineering Proceedings*, *1*(14).

Hayes, M. O. (1975). Morphology of sand accumulation in estuaries: an introduction to the symposium. *Estuarine research*, *2*, 3-22.

Hayes, M. O. (1980). General morphology and sediment patterns in tidal inlets. *Sedimentary geology*, *26*(1), 139-156.

Hudson, R. Y., Herrmann, F. A., & Sager, R. A. (1979). *Coastal hydraulic models* (No. SR-5).

Hunter, J. K., & Vanden-Broeck, J. M. (1983). Solitary and periodic gravity—capillary waves of finite amplitude. *Journal of fluid mechanics*, *134*, 205-219.

International Hydrographic Organization (2005). *Manual on Hydrography.* International Hydrographic Bureau, Monaco.

Ito, M., & Tsuchiya, Y. (1984). *Scale–model relationship of beach profile*. Proc. 19th ICCE, Houston, USA, Vol. 2, pp. 1386–1402.

Ito, M., & Tsuchiya, Y. (1986). *Time scale for modeling beach change*. Proc. 20th ICCE, Taipei, Taiwan, Vol. 2, pp. 1196–1200.

Ito, M., & Tsuchiya, Y. (1988). *Reproduction model of beach change by storm waves*. Proc. 21st ICCE, Malaga, Spain, Vol. 2, pp. 1544–1557.

Ito, M., Murakami, H., Ito, T. (1995). *Reproducibility of beach profiles and sand ripples by huge waves*. Coastal Dynamics 698–708.

Janssen, T. T. (2006). *Nonlinear surface waves over topography* (Doctoral dissertation, TU Delft, Delft University of Technology).

Jonsson, I. G. (1966). Wave boundary layers and friction factors. *Coastal Engineering Proceedings*, *1*(10).

Kamphuis, J. W. (1972). Scale selection for mobile bed wave models. *Proc. 13th ICCE, Vancouver, Canada*, *2*, 1173-1195.

Kamphuis, J. W. (1985). On understanding scale effect in coastal mobile bed models. *Physical Modelling in Coastal Engineering*, 141-162.

Kamphuis, J. W. (1991). Alongshore sediment transport rate. *Journal of Waterway, Port, Coastal, and Ocean Engineering*, *117*(6), 624-640.

Kana, T. W. (1979). *Suspended Sediment in Breaking Waves* (No. TR-18-CRD). SOUTH CAROLINA UNIV COLUMBIA COASTAL RESEARCH DIV.

Keulegan, G. H. (1950). Wave motion. *Engineering hydraulics*, 711-768.

Kleinhans, M. G., van Dijk, W. M., van de Lageweg, W. I., Hoyal, D. C., Markies, H., van Maarseveen, M., ... & Cheshier, N. (2014). Quantifiable effectiveness of experimental scaling of river-and delta morphodynamics and stratigraphy. *Earth-Science Reviews*, *133*, 43-61.

Kleinhans, M. G., Scheltinga, R. T., Vegt, M., & Markies, H. (2015). Turning the tide: Growth and dynamics of a tidal basin and inlet in experiments. *Journal of Geophysical Research: Earth Surface*, *120*(1), 95-119.

Le Mehaute, B. (1976). Similitude in coastal engineering. *Journal of the waterways, harbors and coastal engineering division*, *102*(3), 317-335.

Le Méhauté, B. (1990). Similitude. *The sea ocean engineering science*, *9*, 955-980.

Madsen, O. S., Poon, Y. K., & Graber, H. C. (1988). Spectral wave attenuation by bottom friction: theory. *Coastal Engineering Proceedings*,*1*(21).

Massa Products Cooperation, *Massa M320-150 low cost sensor data sheet.* Online PDF: https://www.massa.com/wp-content/uploads/2016/02/M-320-150-Datasheet-160229.pdf

Morales, J. A., Borrego, J., Jiménez, I., Monterde, J., & Gil, N. (2001). Morphostratigraphy of an ebb-tidal delta system associated with a large spit in the Piedras Estuary mouth (Huelva Coast, Southwestern Spain). *Marine Geology*, *172*(3), 225-241.

Miller, R. L. (1972). *The role of surface tension in breaking waves* (No. TR-13 Tech Rpt). Fluid Dynamics and Sediment Transport Laboratory, Department of the Geophysical Sciences, the University of Chicago.

Nielsen, P. (1984). Field measurements of time-averaged suspended sediment concentrations under waves. *Coastal Engineering*, *8*(1), 51-72.

Nielsen, P. (2006). Sheet flow sediment transport under waves with acceleration skewness and boundary layer streaming. *Coastal Engineering*, *53*(9), 749-758.

Noda, E.K., 1972. Equilibrium beach profile scale–model relationship. Journal of Waterways, Harbors and Coastal Division, ASCE WW4, 511–528.

Oertel, G. F. (1972). Sediment transport of estuary entrance shoals and the formation of swash platforms. *Journal of Sedimentary Research*, *42*(4).

Peakall, J., Ashworth, P., & Best, J. (1996). Physical modelling in fluvial geomorphology: principles, applications and unresolved issues. *The scientific nature of geomorphology*, 221-253.

Petersen, D., Deigaard, R., & Fredsøe, J. (2008). Modelling the morphology of sandy spits. *Coastal Engineering*, *55*(7), 671-684.

Pickrill, R. A. (1985). Sedimentation in an ebb-tidal delta, Rangaunu Harbour, Northland, New Zealand. *New Zealand Journal of Geology and Geophysics*, *28*(3), 531-542.

Sato, S. (1992). Sand transport under grouping waves. *Coastal Engineering Proceedings*, *1*(23).

Schäffer, H. A. (1996). Second-order wavemaker theory for irregular waves.*Ocean Engineering*, *23*(1), 47-88.

Silva, P. A., Abreu, T., Van Der A, D. A., Sancho, F., Ruessink, B. G., Van der Werf, J., & Ribberink, J. S. (2011). Sediment transport in nonlinear skewed oscillatory flows: Transkew experiments. *Journal of hydraulic research*, *49*(sup1), 72-80.

Simons, D.G., Snellen, M. (2016), *Lecture notes "Seafloor Mapping", part 2.* [PDF]. Retrieved from https://ocw.tudelft.nl/wp-content/uploads/seafloor_mapping.pdf

Smit, P., Zijlema, M., & Stelling, G. (2013). Depth-induced wave breaking in a non-hydrostatic, near-shore wave model. *Coastal Engineering*, *76*, 1-16.

Soulsby, R. L., & Smallman, J. V. (1986). A direct method of calculating bottom orbital velocity under waves.

Soulsby, R. L. (1997), Dynamics of Marine Sands, Thomas Telford, London.

Soulsby, R. L. (2006). Simplified calculation of wave orbital velocities.

Stive, M. J. F. (1985). A scale comparison of waves breaking on a beach. *Coastal engineering*, *9*(2), 151-158.

Toffoli, A., Babanin, A., Onorato, M., & Waseda, T. (2010). Maximum steepness of oceanic waves: Field and laboratory experiments. *Geophysical Research Letters*, *37*(5).

Van Rijn, L. C. (1984). Sediment transport, part I: bed load transport. *Journal of hydraulic engineering*, *110*(10), 1431-1456.

Van Rijn, L. C., Tonnon, P. K., Sánchez-Arcilla, A., Cáceres, I., & Grüne, J. (2011). Scaling laws for beach and dune erosion processes. *Coastal Engineering*, *58*(7), 623-636.

Ribberink, J. S., & Al-Salem, A. A. (1994). Sediment transport in oscillatory boundary layers in cases of rippled beds and sheet flow. *Journal of Geophysical Research: Oceans*, *99*(C6), 12707-12727.

Ribberink, J. S., Katopodi, I., Ramadan, K. A., Koelewijn, R., & Longo, S. (1995). Sediment transport under (non)-linear waves and currents. In *Coastal Engineering 1994* (pp. 2527-2541).

Ridderinkhof, W., Hoekstra, P., van der Vegt, M., & de Swart, H. E. (2016). Cyclic behavior of sandy shoals on the ebb-tidal deltas of the Wadden Sea.*Continental Shelf Research*, *115*, 14-26.

Roelofs, L. (2016), Effect of waves in the metronome tidal facility. *Unpubl. Undergraduate Honours Research Project, Dept. of Physical Geography, Utrecht University*, 32 pp.

Rocha, M. V. L., Michallet, H., & Silva, P. A. (2017). Improving the parameterization of wave nonlinearities–The importance of wave steepness, spectral bandwidth and beach slope. *Coastal Engineering*, *121*, 77-89.

Ruessink, B. G., Houwman, K. T., & Hoekstra, P. (1998). The systematic contribution of transporting mechanisms to the cross-shore sediment transport in water depths of 3 to 9 m. *Marine Geology*, *152*(4), 295-324.

Ruessink, B. G., Van den Berg, T. J. J., & Van Rijn, L. C. (2009). Modeling sediment transport beneath skewed asymmetric waves above a plane bed. *Journal of Geophysical Research: Oceans*, *114*(C11).

Ruessink, B. G., Michallet, H., Abreu, T., Sancho, F., Van der Werf, J. J., & Silva, P. A. (2011). Observations of velocities, sand concentrations, and fluxes under velocity-asymmetric oscillatory flows. *Journal of Geophysical Research: Oceans*, *116*(C3).

Ruessink, B. G., Ramaekers, G., & Van Rijn, L. C. (2012). On the parameterization of the free-stream non-linear wave orbital motion in nearshore morphodynamic models. *Coastal Engineering*, *65*, 56-63.

Zijlema, M., Stelling, G., & Smit, P. (2011). SWASH: An operational public domain code for simulating wave fields and rapidly varied flows in coastal waters. *Coastal Engineering*, *58*(10), 992-1012.